

# Interplanetary Trajectory Development

by

Thomas Reed Reppert

Honors Thesis submitted to the Aerospace Engineering Department Faculty of the  
Virginia Polytechnic Institute and State University  
in partial fulfillment of the requirements for the degree of

BACHELOR OF SCIENCE  
*Honors Baccalaureate*

APPROVED

.....  
Hanspeter Schaub, Research Advisor, Aerospace and Ocean Engineering

.....  
Christopher D. Hall, Co-Advisor, Aerospace and Ocean Engineering

.....  
Kevin A. Shinpaugh, Committee Member, Aerospace and Ocean Engineering

This student has fulfilled the requirements of the  
Aerospace Engineering Department to graduate *Honors Baccalaureate*

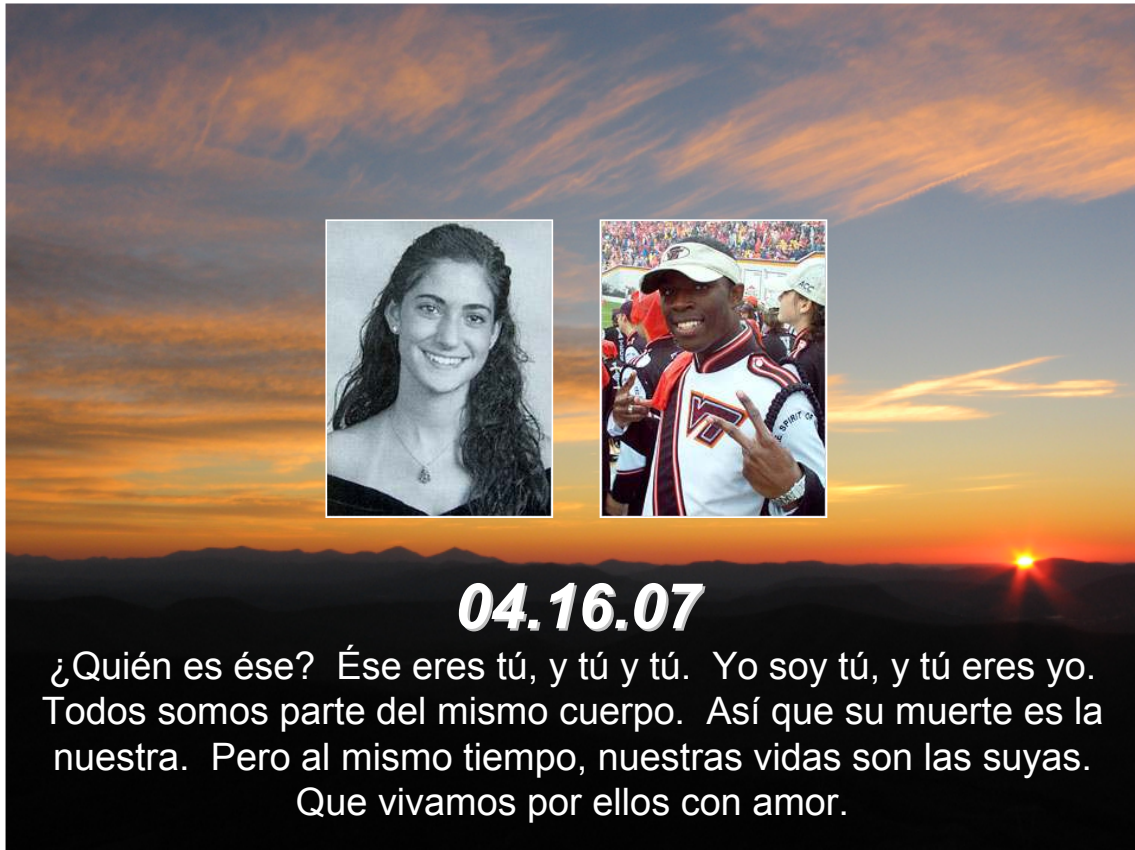
.....  
Madhu B. Kapania, Honors Advisor, Aerospace and Ocean Engineering

May 2007  
Blacksburg, Virginia

## Abstract

Given the costly nature of interplanetary travel, it is important to be able to model accurately a spacecraft's trajectory. Accurate transfer models help to keep the mission fuel budget as low as possible and provide a good starting point for mission operations ground teams. The particular transfer orbit analyzed in this paper is that of a spacecraft traveling from Earth to Mars. The gravitational influences of the sun, Earth, and Mars upon the spacecraft are taken into account for the entire time of flight; thus, this application is termed the restricted four-body problem. A Runge-Kutta integrator is built and used to propagate the non-Keplerian trajectory of the spacecraft. The planets' orbits are initially modeled as circular, but this restriction is eventually relaxed. All interplanetary motion discussed in this paper is planar, although the modeling concepts developed may be extended to three-dimensional motion. Once the spacecraft's equations of motion are derived, they are then integrated to model a Hohmann transfer from Earth to Mars. Sensitivity correction schemes are used to achieve desired arrival orbit geometries for the Hohmann transfer. Finally, the continuation method is used to alter both the spacecraft's time of flight and Mars' heliocentric eccentricity. As such, this paper provides a detailed discussion of several optimization techniques that may be used to accurately model interplanetary trajectories.

## Dedication



In loving memory of Ryan 'Stack' Clark, my fellow servant, and Reema Samaha, my fellow salsaera. You will both be missed greatly, but your wonderful smiles and your loving ways will *never* be forgotten.

## Acknowledgements

I would like to thank my undergraduate research advisor, Dr. Hanspeter Schaub, for his guidance and support during the past two years. He has taught me a great deal not just about celestial mechanics, but also about how to analyze and to conduct research effectively. His concern for my success as both a student and a person has been incredible, and I am forever grateful to have worked with him. I would also like to thank my co-advisor, Dr. Christopher Hall, for his guidance during my undergraduate career. If it were not for Dr. Hall, I would not have had the opportunity to visit Zaragoza, Spain to share my research with the European community. Dr. Hall's sincere care for his students' opportunities is a quality that demands the utmost admiration and respect. Finally, I would like to express my appreciation for the support of my senior design professor, Dr. Kevin Shinpaugh. He has helped me to apply my undergraduate research to our design project, graciously offering guidance and suggestions wherever needed. Virginia Tech is a very special campus filled with brilliant and amazing people, and I am honored to have learned from some of the best.

# Nomenclature

$a$	Semi-major axis
$\mathbf{A}$	Nonlinear operator
$[A]$	Coefficient matrix
$c$	Chord length
$d_a$	Perpendicular miss distance of the arrival orbit
$d_e$	Error in miss distance calculation
$d^*$	Desired miss distance
$e$	Eccentricity
$g$	Integration time step
$G$	Universal gravitation constant
$\mathbf{h}$	Angular momentum
$i$	Iteration counter
$[I]$	Identity matrix
$k$	Spring constant
$\mathbf{L}$	Auxiliary linear operator
$m$	Point mass
$n$	Mean orbit rate
$N$	Continuation method maximum iterations
$p$	Semilatus rectum
$P$	Transfer orbit period
$r_3$	Arrival orbit periapsis radius
$r_{3e}$	Error in periapsis calculation
$\mathbf{r}$	Orbit position
$r_\oplus$	Earth's mean heliocentric orbit radius
$r_\sigma$	Mars' mean heliocentric orbit radius
$t$	Orbit time
$\mathbf{v}$	Heliocentric velocity
$\mathbf{x}(t)$	Generic state vector
$\mathbf{y}(t)$	Spacecraft state vector
$\alpha$	Continuation method step parameter
$\beta$	Sensitivity optimization weight parameter
$\delta\mathbf{x}(t)$	Error vector
$\Delta\hat{t}$	Current integration time
$\Delta\tilde{t}$	Desired integration time
$\epsilon$	Sensitivity perturbation value
$\phi$	Increment function
$\Phi$	Departure burn angle
$[\Phi(t, t_0)]$	State transition matrix
$\gamma$	Phase difference between Earth and Mars
$\lambda$	Eigenvalue of the coefficient matrix
$\mu$	Gravitational coefficient

$\nu$	Planet-relative velocity
$\vartheta$	Planet-relative heading angle
$\sigma$	Heliocentric heading angle
$\tau$	Continuation parameter
$\omega_n$	Natural frequency
$\xi$	Stopping criterion

# Contents

<b>1</b>	<b>Development of the Restricted Four-Body Problem</b>	<b>1</b>
1.1	Introduction . . . . .	1
1.2	Patched-Conic Approximation . . . . .	2
1.2.1	Establishing the Initial Offset Angle . . . . .	2
1.2.2	Determining the Heliocentric Departure Velocity . . . . .	3
1.2.3	Leaving Earth's Sphere of Influence . . . . .	4
1.2.4	Entering Mars' Sphere of Influence . . . . .	6
1.3	Restricted Four-Body Problem . . . . .	9
1.3.1	Derivation of the Equations of Motion . . . . .	9
1.3.2	Numerical Integrator . . . . .	12
1.3.3	Four-Body Algorithm . . . . .	14
1.3.4	Validity Check . . . . .	16
1.4	Integration Results . . . . .	17
1.4.1	Comparison of the Patched-Conic and Restricted Four-Body Solutions . . . . .	17
1.4.2	Altering the Initial Conditions . . . . .	21
1.4.3	Comparison of Predicted $\Delta v$ Values . . . . .	25
1.5	Conclusions . . . . .	26
<b>2</b>	<b>Application of Sensitivities to the Restricted Four-Body Problem</b>	<b>28</b>
2.1	Introduction . . . . .	28
2.2	Converting Code from Matlab to C . . . . .	29
2.3	State Transition Matrices . . . . .	30
2.3.1	Linear, Homogeneous Dynamic Systems . . . . .	31
2.3.2	Spring-Mass System; Direct Analytical Solution . . . . .	32
2.3.3	Spring-Mass System; State Transformation Solution . . . . .	32
2.3.4	Spring-Mass System; Matrix Exponential Solution . . . . .	34
2.3.5	Using State Transition Matrices to Apply Corrections to Initial Conditions . . . . .	34
2.4	Sensitivity Analysis of the Restricted Four-Body Problem . . . . .	35
2.4.1	Analytical Solution for $\frac{\partial d_a}{\partial v_0}$ . . . . .	36
2.4.2	Numerical Solution for $\frac{\partial d_a}{\partial v_0}$ . . . . .	41
2.4.3	Numerical Solution for $\frac{\partial r_3}{\partial v_0}$ . . . . .	43
2.4.4	Integration Time Comparison . . . . .	46
2.5	Conclusions . . . . .	47

<b>3</b>	<b>Application of Continuation Methods to the Restricted Four-Body Problem</b>	<b>49</b>
3.1	Introduction . . . . .	49
3.2	Continuation Methods . . . . .	50
3.2.1	Introduction . . . . .	50
3.2.2	Application: Sensitive Two-Point Boundary Value Problem . . . . .	52
3.3	Restricted Four-Body Problem . . . . .	58
3.3.1	Altering the Time of Flight: First Method . . . . .	59
3.3.2	Altering the Time of Flight: Revised Method . . . . .	60
3.3.3	Altering Mars' Eccentricity . . . . .	63
3.4	Conclusions . . . . .	64

# List of Tables

1.1	Semi-Major Axis Correction Scheme Miss Distance Values . . . . .	24
1.2	Comparison of $\Delta v$ Estimates for the Hohmann Transfer . . . . .	26
2.1	Error Values Using Analytical $\partial d_a / \partial v_0$ . . . . .	39
2.2	Effects of Perturbation Value $\epsilon$ Using Numerical $\frac{\partial d_a}{\partial v_0}$ . . . . .	43
3.1	Example Continuation Application Initial Conditions . . . . .	57
3.2	Initial Velocity Corrections: Revised Method . . . . .	61

# List of Figures

1.1	Illustration of the Hohmann Transfer . . . . .	3
1.2	Illustration of the Hyperbolic Departure . . . . .	4
1.3	Illustration of the Hyperbolic Arrival . . . . .	7
1.4	Illustration of the Arrival Heading Angles . . . . .	8
1.5	Coordinate Frames and Position Vectors . . . . .	10
1.6	Earth's Motion With Respect to the Sun . . . . .	12
1.7	Fourth-Order Runge-Kutta Method . . . . .	13
1.8	Critical Orbit Integrator Check . . . . .	16
1.9	Integration Time Step Validation . . . . .	17
1.10	Patched-Conic and Four-Body Motions . . . . .	18
1.11	Restricted Four-Body Heliocentric Motion . . . . .	19
1.12	Restricted Four-Body Arrival Orbit . . . . .	20
1.13	Arrival Orbits Corresponding to Initial Offset Angle Variations . . . . .	22
1.14	Semi-Major Axis Correction Algorithm . . . . .	23
1.15	Semi-Major Axis Correction Results . . . . .	24
1.16	Semi-Major Axis Correction Miss Distance Errors . . . . .	25
2.1	Setup for the C Miss Distance Calculation . . . . .	30
2.2	Geometry Used to Approximate the Hohmann Chord Length . . . . .	37
2.3	Parameters of the Hyperbolic Departure Orbit . . . . .	38
2.4	Correction Scheme Using Analytical $\partial d_a / \partial \nu_0$ . . . . .	40
2.5	Error Values Using Analytical $\partial d_a / \partial \nu_0$ . . . . .	41
2.6	Final Mars-Relative Arrival Orbit Geometry Using Analytical $\partial d_a / \partial \nu_0$ . . . . .	42
2.7	Effect of $\epsilon$ on Number of Iterations Using Numerical $\frac{\partial d_a}{\partial \nu_0}$ . . . . .	44
2.8	Effect of $\epsilon$ on Number of Iterations Using Numerical $\frac{\partial r_3}{\partial \nu_0}$ . . . . .	45
2.9	Plot of Integration Times . . . . .	47
3.1	Flowchart for Example Continuation Application . . . . .	53
3.2	Example Continuation Application Final States . . . . .	56
3.3	Progressively Smaller Values of $\Delta t$ . . . . .	59
3.4	Final Heliocentric Transfer Geometry: Revised Method . . . . .	60
3.5	Final Mars-Relative Transfer Geometry: Revised Method . . . . .	62
3.6	Heliocentric Motion: Elliptic Martian Orbit . . . . .	63

# Chapter 1

## Development of the Restricted Four-Body Problem

### 1.1 Introduction

A Hohmann transfer is an interplanetary mission that requires a change in true anomaly of 180 degrees. It is a particular type of minimum energy transfer orbit. In fact, the Hohmann transfer is an interplanetary mission that requires a minimum initial burn in order to reach the foreign planet.[2] The Hohmann is commonly used to transfer from one circular orbit to another. Thus, it is an attractive option for designing future missions from Earth to Mars.

Analytic solutions relating the planets' mean heliocentric orbit radii to the required departure burn have already been established.[13] These equations were developed chiefly through the application of conservation laws, including the conservations of both angular momentum and energy. But these solutions only provide a rough estimate of how to reach Mars' sphere of influence. We desire a higher fidelity method for estimating the required initial burn. In addition, we seek a method which allows us to alter the departure orbit geometry and to analyze the effects upon the arrival at Mars. The analytic Hohmann solution fully disregards the gravitational influences of both Earth and Mars. By failing to consider the spacecraft's departure and arrival orbits, this solution only provides a preliminary estimate of the required departure burn.

The patched-conic approximation has thus been developed as a more accurate solution to interplanetary transfer description. It involves partitioning the overall transfer into distinct conic solutions. For instance, as a spacecraft travels from Earth to Mars, its orbit is approximated as a hyperbolic departure, an elliptic transfer, and a hyperbolic arrival. The patched-conic approximation breaks the entire orbit down into several two-body problems. In other words, only one celestial body's influence is considered to be acting upon the spacecraft at all times. This approximation provides a much better understanding of the relation between the departure orbit and the overall transfer than the analytic Hohmann solution. However, the patched-conic approximation is still limited in that it only considers the gravity of one celestial body at a time. During a true Hohmann transfer from Earth to Mars, the sun will have some minute gravitational effect upon the spacecraft during both the departure and arrival orbits. A numerical integrator is necessary in order to take such

smaller perturbations into account.

When looking to design a real-time interplanetary mission from Earth to Mars, we seek a higher fidelity orbit description than the patched-conic approximation. Thus, we introduce the restricted four-body problem, which offers a more precise representation of the transfer orbit. The restricted four-body problem, applied to a Hohmann transfer from Earth to Mars, considers the gravitational influences of Earth, the sun, and Mars at all times. Thus, unlike the patched-conic approximation, this orbit integration scheme allows us view the direct effect of altered initial conditions upon the hyperbolic arrival orbit. Perhaps most importantly, the restricted four-body problem presents a method of analyzing a highly non-linear transfer orbit without breaking the actual orbit into separate parts.

## 1.2 Patched-Conic Approximation

The patched-conic approximation offers an efficient method for developing interplanetary orbits. By partitioning the overall orbit into a series of two-body orbits, it greatly simplifies mission analysis. For instance, the initial part of an interplanetary voyage may be approximated as a hyperbola with the departure planet at the focus. Once the spacecraft leaves the departure planet's sphere of influence, the orbit may be approximated as an ellipse whose focus is centered at the sun. Once the vehicle enters the arrival planet's sphere of influence, the orbit may again be approximated as hyperbolic, with its focus now centered at the arrival planet. For each of the three portions of the orbit, one gravitational force is assumed to be acting upon the spacecraft at a time.[2]

To illustrate the efficiency of the patched-conic approximation, we partition the standard Hohmann transfer of a spacecraft traveling from Earth to Mars into three separate conic stages. During the initial portion of the voyage, we approximate the transfer as a hyperbolic departure orbit with its primary focus positioned at the center of the Earth. After escaping the Earth's sphere of influence, the spacecraft then enters its elliptic orbit about the sun. Following this second stage, the spacecraft enters Mars' sphere of influence. Once again, we approximate the motion as a hyperbolic orbit, this time with its focus located at the center of Mars. All portions of the transfer orbit are assumed to be planar. Because each portion of the voyage is considered a two-body problem, there is never more than one gravitational force acting upon the spacecraft at a given time.

### 1.2.1 Establishing the Initial Offset Angle

If the spacecraft is to intercept Mars after its transfer, there needs to exist some specific offset angle  $\gamma(t_1)$  between Earth and Mars at the initial time  $t_1$ . Figure 1.1 illustrates the Hohmann transfer orbit from Earth to Mars. Note that time  $t_1$  corresponds to the instant at which the spacecraft leaves Earth's sphere of influence, while time  $t_2$  denotes the instant when the craft enters Mars' sphere of influence. If  $n_{\oplus}$  denotes the mean Hohmann orbit rate, then the Hohmann transfer period is given by

$$P = \frac{1}{2} \frac{2\pi}{n_{\oplus}} = \pi \sqrt{\frac{a_{\oplus}^3}{\mu_{\odot}}} \quad (1.1)$$

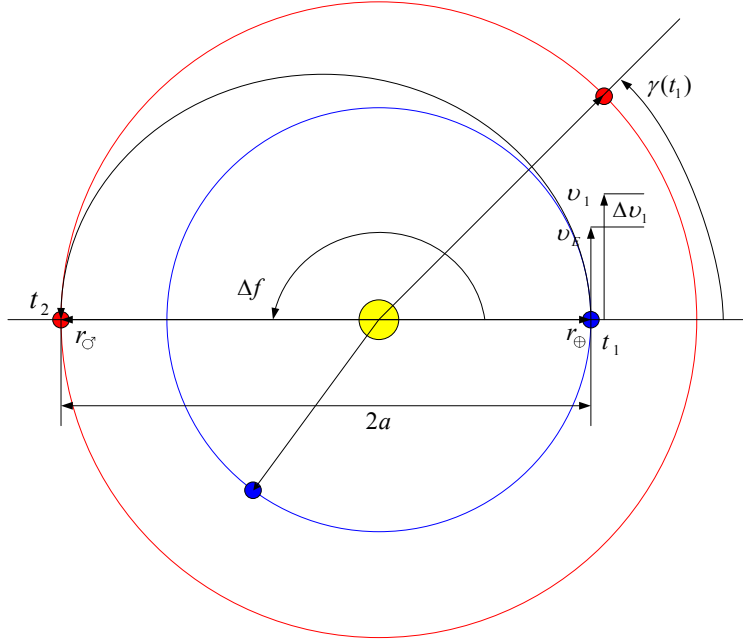


Figure 1.1: **Illustration of the Hohmann Transfer.** The Hohmann is a minimum-energy transfer orbit.

where  $a_{\oplus}$  is the semi-major axis of the transfer orbit, as shown in Figure 1.1. Taking the value of  $a_{\oplus}$  from the constants listing, the transfer period  $P$  is determined to be 258.979 days. Because Mars travels a distance  $n_{\sigma}P$  during the spacecraft's travel, the initial phase difference between Earth and Mars must be

$$\gamma(t_1) = \pi - n_{\sigma}P \quad (1.2)$$

where  $n_{\sigma}$  corresponds to Mars' mean orbit rate. Using the value of  $n_{\sigma}$  given in the constants listing, the initial offset angle for the Hohmann transfer is found to be 44.343 deg.

## 1.2.2 Determining the Heliocentric Departure Velocity

The typical application of the patched-conic solution is to determine approximately what  $\Delta v$  is needed to complete a certain transfer mission. This method is most accurate in establishing the magnitude of the  $\Delta v$ , as opposed to its direction or timing. We first seek the necessary heliocentric velocity  $v_1$  as the spacecraft leaves the Earth's sphere of influence. This particular velocity is illustrated in Figure 1.1. The  $v_1$  necessary to complete the Hohmann transfer may be computed as

$$v_1 = \sqrt{\frac{2\mu_{\odot}}{r_{\oplus} + r_{\sigma}} \left( \frac{r_{\sigma}}{r_{\oplus}} \right)} \quad (1.3)$$

where  $\mu_{\odot}$  denotes the sun's gravitational coefficient,  $r_{\oplus}$  denotes the Earth's mean orbit radius, and  $r_{\sigma}$  denotes Mars' mean orbit radius. For a complete derivation of Equation (1.3), consult Schaub and Junkins.[13] Using the quantities for  $\mu_{\odot}$ ,  $r_{\oplus}$ , and  $r_{\sigma}$  given in the constants listing, the heliocentric velocity  $v_1$  is computed to be 32.715 km/s. Once the

heliocentric departure velocity is calculated,  $\Delta v_1$  may be computed as

$$\Delta v_1 = v_1 - v_\oplus = v_\oplus \left( \sqrt{\frac{2r_\sigma}{r_\oplus + r_\sigma}} - 1 \right) \quad (1.4)$$

where  $v_\oplus$  is the Earth's mean heliocentric velocity, as shown in Figure 1.1. Because  $r_\sigma > r_\oplus$ , the resulting  $\Delta v_1$  will be positive. Using the value of  $v_\oplus$  in the constants listing, the  $\Delta v_1$  for the Hohmann transfer is calculated as 2.943 km/s. After performing the  $\Delta v_1$ , the spacecraft leaves Earth's sphere of influence and enters into its elliptic orbit about the sun. During this portion of the mission, the sun is the only celestial body considered to be influencing the motion of the spacecraft. At the end of the Hohmann transfer, the spacecraft enters Mars' sphere of influence and begins its hyperbolic arrival orbit. The departure and arrival orbits will now be considered.

### 1.2.3 Leaving Earth's Sphere of Influence

The following discussion offers a closer examination of how the spacecraft escapes Earth's sphere of influence. Figure 1.2 offers an illustration of the departure. Note that time  $t_0$  corre-

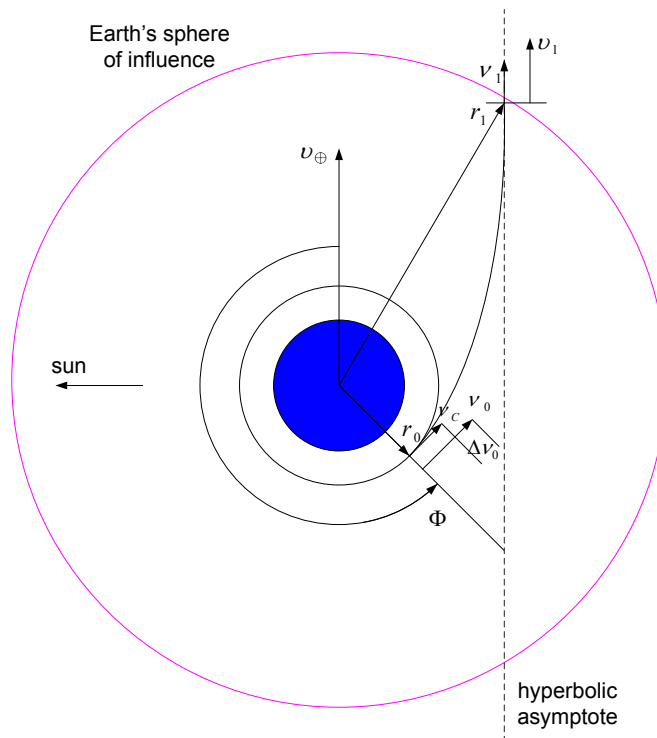


Figure 1.2: **Illustration of the Hyperbolic Departure.** The spacecraft escapes Earth's sphere of influence and attains the heliocentric velocity  $v_1$ .

sponds to the spacecraft's departure from the initial parking orbit, while time  $t_1$  again corresponds to the instant at which the spacecraft escapes Earth's sphere of influence. Throughout

the following analysis, heliocentric velocities are expressed as  $v_i$ , while planet-centric velocities are denoted as  $\nu_i$ . In an attempt to leave Earth's sphere of influence, either a parabolic or hyperbolic orbit is necessary. But because the spacecraft is required to converge to some velocity  $v_1$  as it leaves Earth's sphere of influence, the departure orbit must be hyperbolic. The necessary Earth-relative velocity  $\nu_1$  at the limit of the sphere of influence is computed as

$$\nu_1 = v_1 - v_\oplus \quad (1.5)$$

Thus, the corresponding Earth-relative velocity  $\nu_1$  for the Hohmann transfer is 2.943 km/s. We can also use the vis-viva equation[13] to determine the Earth-relative velocity  $\nu_1$  as

$$\nu_1 = \sqrt{\frac{2\mu_\oplus}{r_1} - \frac{\mu_\oplus}{a_h}} \approx \sqrt{-\frac{\mu_\oplus}{a_h}} \quad (1.6)$$

where  $\mu_\oplus$  denotes the Earth's gravitational coefficient and  $a_h$  corresponds to the semi-major axis of the departure hyperbola. We approximate  $r_1 \approx \infty$  due to the assumption that the spacecraft trajectory asymptotically approaches its limiting value at time  $t_1$ . Therefore, we can relate the departure hyperbola's semi-major axis to either  $\nu_1$  or  $v_1$  via

$$a_h = \frac{-\mu_\oplus}{\nu_1^2} = -\frac{\mu_\oplus}{(v_1 - v_\oplus)^2} \quad (1.7)$$

Because  $\nu_1$  equals 2.943 km/s, we find the hyperbolic semi-major axis  $a_h$  to be -46010 km. Using the vis-viva equation once again, the Earth-relative speed  $\nu_0$  that the vehicle must have in order to initiate the hyperbolic transfer orbit at  $t_0$  becomes

$$\nu_0 = \sqrt{\frac{2\mu_\oplus}{r_0} - \frac{\mu_\oplus}{a_h}} \quad (1.8)$$

where  $r_0$  denotes the spacecraft's initial parking orbit radius about the Earth. After substituting the relation for  $a_h$  given in Equation (1.7), the speed  $\nu_0$  is expressed as

$$\nu_0^2 = \nu_1^2 + \frac{2\mu_\oplus}{r_0} \quad (1.9)$$

At this point, it is important to note that once  $\nu_1$  and  $r_0$  are chosen for a particular mission, the corresponding patched-conic approximation for  $\nu_0$  is set. However, because  $\nu_1$  is determined via the semi-major axis of the elliptic transfer orbit, we truly set  $\nu_0$  with our choices of  $a_\oplus$  and  $r_0$ . Throughout the remainder of Chapter 2, we consider the value of  $a_\oplus$  given in the constants listing (1.8877e+008 km), as well as an initial parking orbit radius  $r_0$  of 7500 km. Using these values, we find a corresponding  $\nu_0$  of 10.722 km/s.

In order to maintain its initial parking orbit about Earth, the spacecraft has a critical speed of

$$\nu_c = \sqrt{\frac{\mu_\oplus}{r_0}} \quad (1.10)$$

which is calculated to be 7.290 km/s given the previous values of  $\mu_\oplus$  and  $r_0$ . Thus, in order to begin the hyperbolic transfer, the initial burn required is given as

$$\Delta\nu_0 = \nu_0 - \nu_c = \sqrt{2\nu_c^2 + \nu_1^2} - \nu_c \quad (1.11)$$

As shown in Figure 1.2, the point where the initial  $\Delta\nu_0$  burn must be applied is defined via the angle  $\Phi$ . For any transfer to an outer planet, the spacecraft's velocity should asymptotically align itself with the Earth's heliocentric velocity. Thus, the burn angle  $\Phi$  may be determined from the geometry of the departure hyperbola as

$$\Phi = \cos^{-1}\left(\frac{1}{e_h}\right) + \pi \quad (1.12)$$

where  $e_h$  refers to the eccentricity of the hyperbolic departure orbit. For a complete derivation of Equation (1.12), refer to Bate, Mueller, and White.[1] In order to find the departure eccentricity, we analyze the orbit's angular momentum. Referring to the definition of angular momentum, as well as the orbit geometry, we find that

$$h_h^2 = \mu_{\oplus}p = \mu_{\oplus}a_h(1 - e_h^2) = \mu_{\oplus}r_p(1 + e_h) \quad (1.13)$$

where  $h_h$  denotes the angular momentum of the departure orbit,  $p$  refers to the departure semilatus rectum, and  $r_p$  represents the radius at periapsis. But because the burn point at time  $t_0$  is the periapsis point of the departure hyperbola, we know that  $r_0 = r_p$ . Therefore, the angular momentum can also be expressed as

$$h_h^2 = r_0^2\nu_0^2 \quad (1.14)$$

Relating Equations (1.13) and (1.14), we we can now express the departure orbit eccentricity as

$$e_h = \frac{r_0\nu_0^2}{\mu_{\oplus}} - 1 = \frac{r_0\nu_1^2}{\mu_{\oplus}} + 1 \quad (1.15)$$

Using the previously stated values of  $r_0$  and  $\nu_0$  (7500 km and 10.722 km/s, respectively), the departure eccentricity  $e_h$  is given as 1.163. It is important to note that all hyperbolic orbits must have an eccentricity greater than one. Finally, referring back to Equation (1.12) and using the calculated value of  $e_h$ , we find the initial burn angle  $\Phi$  to be roughly 211 degrees.

The patched-conic solution analytically approximates the required velocity  $\nu_1$  at the Earth's sphere of influence necessary to begin the Hohmann transfer to Mars. More rigorous details, such as the effect of the distance between the spacecraft velocity direction and the Earth's heliocentric velocity direction on the orbit, require the use of numerical integration techniques. These techniques will be introduced in Chapter 3.

### 1.2.4 Entering Mars' Sphere of Influence

The following section presents the patched-conic approximation of how the spacecraft enters Mars' sphere of influence. Figure 1.3 offers an illustration of the arrival orbit. It is typical for any spacecraft traveling to an outer planet to enter that planet's sphere of influence ahead of the planet. The spacecraft reaches the outer planet at the apoapsis of the transfer orbit. Therefore, the spacecraft's speed will be less than that of the planet, allowing the planet to overtake it. Once again, using the vis-viva equation,[13] we find the heliocentric arrival velocity  $v_2$  of the spacecraft to be

$$v_2 = \sqrt{2\mu_{\odot}\left(\frac{1}{r_{\sigma}} - \frac{1}{r_{\oplus}}\right) + v_1^2} \quad (1.16)$$

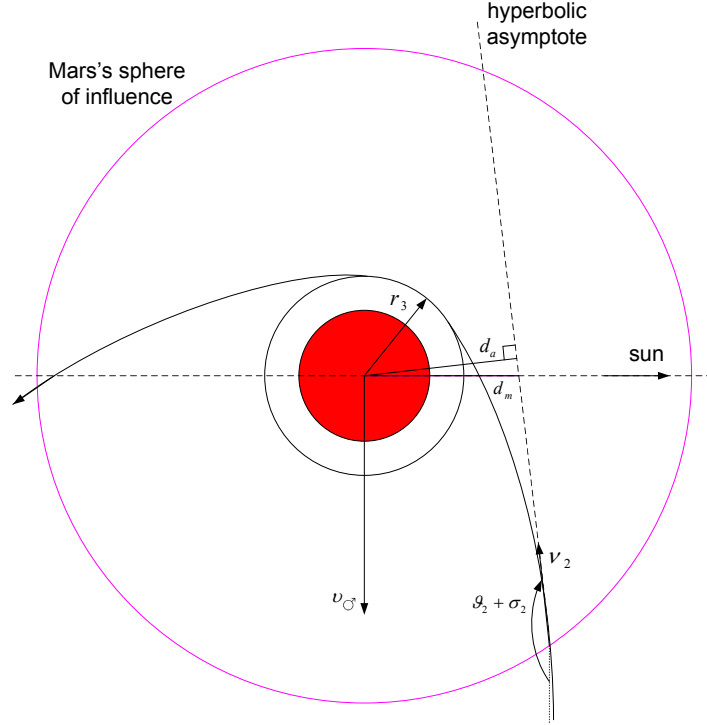


Figure 1.3: **Illustration of the Hyperbolic Arrival.** The spacecraft enters Mars' sphere of influence with the heliocentric velocity  $v_2$  as it approaches the periapsis radius  $r_3$ .

Given the previous calculation of  $v_1$ , we find  $v_2$  to be 21.471 km/s for the transfer to Mars. In general, the spacecraft's heliocentric velocity will be tangent to that of the Earth when it begins the Hohmann. But when it arrives at Mars, it will most likely cross Mars' sphere of influence with some heading angle  $\sigma_2$ . [1]. In order to compute the  $\sigma_2$  heading angle between the sun-normal direction and the craft's heliocentric velocity, we again recall the formal definition of angular momentum as

$$\mathbf{h} = \mathbf{r} \times \mathbf{v} \quad (1.17)$$

Assuming that the radius of Earth's sphere of influence is negligible compared with the major heliocentric orbit axis, we find  $h_e = r_\oplus v_1$ . As the spacecraft enters Mars' sphere of influence, its angular momentum can also be given as

$$h_e = |\mathbf{r}_\sigma \times \mathbf{v}_2| = r_\sigma v_2 \sin\left(\frac{\pi}{2} - \sigma_2\right) = r_\sigma v_2 \cos(\sigma_2) \quad (1.18)$$

Thus, we find the heading angle relative to the sun normal direction to be

$$\sigma_2 = \cos^{-1}\left(\frac{h_e}{r_\sigma v_2}\right) = \cos^{-1}\left(\frac{r_\oplus v_1}{r_\sigma v_2}\right) \quad (1.19)$$

The heading angle corresponding to the Hohmann transfer is determined to be roughly 0 degrees. For a perfect Hohmann transfer, the value of  $\sigma_2$  would be exactly equal to 0 degrees. To compute the spacecraft's Mars-centric velocity vector  $\mathbf{v}_2$ , Mars' heliocentric velocity must

be subtracted from that of the spacecraft:

$$\boldsymbol{\nu}_2 = \boldsymbol{v}_2 - \boldsymbol{v}_\sigma \quad (1.20)$$

Via the law of cosines, the magnitude of  $\boldsymbol{\nu}_2$  is calculated as

$$\nu_2 = \sqrt{v_2^2 + v_\sigma^2 - 2v_2v_\sigma \cos \sigma_2} \quad (1.21)$$

which yields a value of 2.648 km/s for the given Hohmann. The heading angle  $\vartheta_2$  between the  $\boldsymbol{v}_2$  and  $\boldsymbol{\nu}_2$  velocity vectors is roughly 180 degrees for the Hohmann transfer, where Figure 1.4 offers an illustration of the triangular geometry. For a perfect Hohmann transfer, the

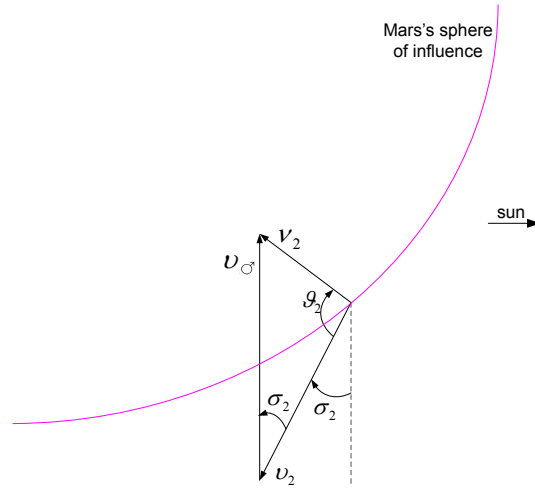


Figure 1.4: **Illustration of the Arrival Heading Angles.** The spacecraft's trajectory is described using two heading angles upon its entrance into Mars' sphere of influence.

value of  $\vartheta_2$  would be exactly 180 degrees.

Identical to the process used for the departure orbit, we use the energy (vis-viva) equation to determine the semi-major axis of the arrival orbit through

$$\frac{1}{a_h} = \frac{2}{r_2} - \frac{\nu_2^2}{\mu_\sigma} \quad (1.22)$$

Making the patched-conic assumption that the spacecraft's approach orbit is hyperbolic, we approximate  $a_h$  as

$$a_h = -\frac{\mu_\sigma}{\nu_2^2} \quad (1.23)$$

where  $r_2 \approx \infty$ . If the Hohmann orbit were perfect, the spacecraft would directly hit the Martian surface. To avoid this occurrence, the hyperbolic arrival trajectory is aimed such that it will miss Mars by some miss distance  $d_m$ , as shown in Figure 1.3. However, from the spacecraft's perspective, it is easiest to estimate the shortest distance  $d_a$  between the approach asymptote and Mars, given by

$$d_a = d_m \sin(\vartheta_2 + \sigma_2) \quad (1.24)$$

Similar to the departure orbit, we examine the spacecraft's constant angular momentum in order to determine the arrival eccentricity. Figure 1.3 illustrates how the angular momentum simplifies to

$$h_h = |\mathbf{r}_2 \times \boldsymbol{\nu}_2| = d_a \nu_2 \quad (1.25)$$

Substituting Equation (1.25) into Equation (1.13), we find the hyperbolic eccentricity  $e_h$  as

$$e_h = \sqrt{1 + \frac{d_a^2 \nu_2^4}{\mu_\sigma}} \quad (1.26)$$

Finally, the periapsis radius  $r_p$  of the arrival orbit can be calculated by substituting Equation (1.23) into the angular momentum expression of Equation (1.13) as

$$r_p = \frac{\mu_\sigma}{\nu_2^2} (e_h - 1) \quad (1.27)$$

The transfer mission is usually designed in such a way that the periapsis radius is equivalent to the final parking orbit radius. Thus, the final orbit radius about Mars is uniquely determined once both the eccentricity  $e_h$  and arrival speed  $\nu_2$  are given. Because  $e_h$  depends upon the miss distance, the arrival is actually set with prescribed values of  $d_m$  and  $\nu_2$ .

## 1.3 Restricted Four-Body Problem

In this section, we extend the patched-conic approximation to a restricted four-body problem. Taking into consideration the gravitational influences of the sun, Earth, and Mars at all times, we determine the spacecraft's transfer orbit from Earth to Mars. The motion is not analyzed with respect to the three separate spheres of influence. Instead, this method incorporates the gravitational effects of each celestial body even when the spacecraft is beyond the body's sphere of influence. The analysis incorporates these comparatively minute effects in order to better estimate the exact state of the vehicle upon arrival at Mars. All orbital motion during the transfer is assumed to be planar. Thus, the effects of Earth's and Mars' orbit inclinations are not considered when integrating the spacecraft's trajectory.

Because the restricted four-body problem is considerably more complex than the two-body problem, numerical integration is used to develop the spacecraft's orbit. Integrating numerically allows for the incorporation of the sun's, Earth's, and Mars' gravitational influences at all times. After completing the orbit integration, we perform a series of sanity checks on the results in an attempt to verify their legitimacy. Of particular interest is how the initial conditions of the four-body setup may be modified in order to achieve the desired arrival position and velocity. Thus, adjustments in the initial position and velocity data are made and the effects upon the spacecraft's arrival at Mars are measured.

### 1.3.1 Derivation of the Equations of Motion

#### Application of the $n$ -Body Problem

Before beginning the numerical integration process, we must first derive the equations of motion that we wish to integrate. Figure 1.5 offers an illustration of the coordinate frames

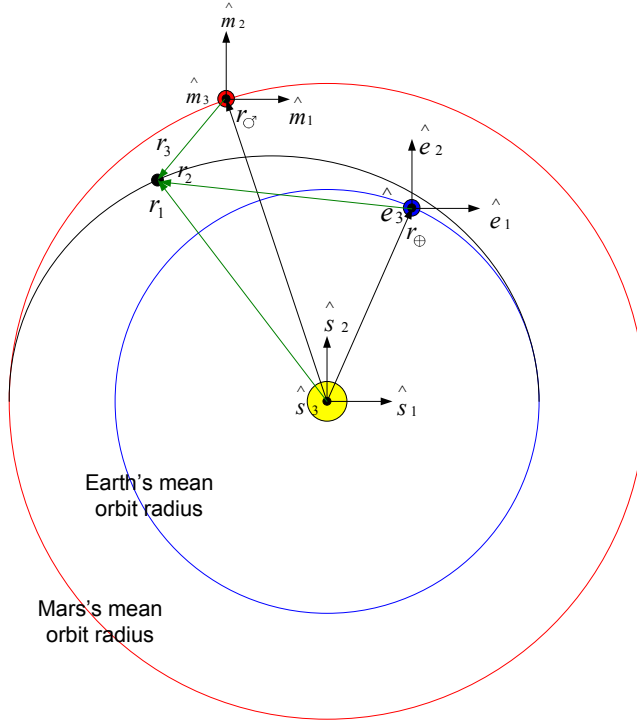


Figure 1.5: **Coordinate Frames and Position Vectors.** Definition of the coordinate frames and position vectors used to derive the spacecraft's equations of motion. Note that the sun-centered frame is inertial.

we use to designate the state of the spacecraft for all time  $t$ . The  $\mathcal{S}$ :  $\{\hat{s}_1, \hat{s}_2, \hat{s}_3\}$  frame is an inertial frame centered at the sun. Thus, we make the assumption that the sun is stationary during the spacecraft's transfer orbit. The  $\mathcal{E}$ :  $\{\hat{e}_1, \hat{e}_2, \hat{e}_3\}$  frame is a non-rotating frame centered at Earth. We use this frame to describe the state of the spacecraft with respect to Earth. In addition, the  $\mathcal{M}$ :  $\{\hat{m}_1, \hat{m}_2, \hat{m}_3\}$  frame is a non-rotating frame centered at Mars. In a similar manner, we use the  $M$  frame to track the state of the spacecraft relative to Mars. Now that the coordinate frames have been established, we can express the position of the spacecraft with respect to the three origins. As shown in Figure 1.5, the spacecraft's position with respect to the sun, Earth, and Mars are labeled  $\mathbf{r}_1$ ,  $\mathbf{r}_2$ , and  $\mathbf{r}_3$ , respectively.

For a general  $n$ -body problem, the total force  $\mathbf{f}_i$  acting upon mass  $m_i$ , due to the other  $n - 1$  masses, is

$$\mathbf{f}_i = G \sum_{j=1}^n \frac{m_i m_j}{r_{ij}^3} (\mathbf{r}_j - \mathbf{r}_i) \quad (1.28)$$

where  $G$  is the universal gravitation constant. Note that the term for which  $i = j$  is to be omitted. Newton's Second Law of Motion states

$$\mathbf{f}_i = m_i \frac{d^2 \mathbf{r}_i}{dt^2} \quad (1.29)$$

Therefore, the  $n$  vector differential equations

$$\frac{d^2 \mathbf{r}_i}{dt^2} = G \sum_{j=1}^n \frac{m_j}{r_{ij}^3} (\mathbf{r}_j - \mathbf{r}_i) \quad (1.30)$$

along with appropriate initial conditions completely describe the motion of the system of  $n$  particles. Consult Battin for the complete derivation of Equation (1.30).[2] With our restricted four-body assumption, we neglect the gravitational effects of the spacecraft upon the three celestial bodies. We also treat the two planetary orbits as perfect circles, neglecting any relatively small deviations from these idealized orbits. Thus, for our specific case, we can apply Equation (1.30) as

$$\ddot{\mathbf{r}}_1 + \frac{\mu_\odot}{r_1^3} \mathbf{r}_1 + \frac{\mu_\oplus}{r_2^3} \mathbf{r}_2 + \frac{\mu_\sigma}{r_3^3} \mathbf{r}_3 = 0 \quad (1.31)$$

where  $\ddot{\mathbf{r}}_1$  represents the second inertial derivative of  $\mathbf{r}_1$  with respect to time. Also, we have used the relation

$$\mu = G(m_1 + m_2) \quad (1.32)$$

in order to express our equations of motion of the spacecraft in terms of the three gravitational coefficients  $\mu_i$  of the celestial bodies. By analysis of Equation (1.31), we see that as the spacecraft's trajectory is outside the spheres of influence of Earth and Mars, the second term will govern. Thus, because the sun's gravitational coefficient is so much greater than that of Earth and Mars, the sun will provide the primary gravitational force during most of the transfer. But when the spacecraft is sufficiently close to either planet (i.e. within their spheres of influence), the third and fourth terms will govern. The patched-conic approximation involved a simplified version of Equation (1.31) by assuming the smaller terms for each portion of the transfer to be zero. But our four-body integrator will take these small perturbations into consideration in order to achieve a more accurate representation of the spacecraft's state development.

## Motion of Earth and Mars

As stated earlier, we assume the motion of both Earth and Mars to be circular. Figure 1.6 offers an illustration of Earth's circular orbit about the sun. We define the angle  $\theta$  from the positive  $\hat{\mathbf{s}}_1$  direction to the Earth's position vector  $\mathbf{r}_\oplus$ . Thus, we can express the  $\hat{\mathbf{s}}_1$  component of the Earth's position as

$$x_\oplus = r_\oplus \cos \theta \quad (1.33)$$

Similarly, we find that the  $\hat{\mathbf{s}}_2$  component of  $\mathbf{r}_\oplus$  is

$$y_\oplus = r_\oplus \sin \theta \quad (1.34)$$

In order to express the position of Earth in terms of time  $t$ , we can use Earth's mean orbit rate as  $\theta = n_\oplus t$ . Finally, we write Earth's position vector in the  $S$  frame as

$$\mathbf{r}_\oplus(t) = \begin{pmatrix} r_\oplus \cos n_\oplus t \\ r_\oplus \sin n_\oplus t \\ 0 \end{pmatrix}^S \quad (1.35)$$



of the method is

$$\mathbf{y}_{i+1} = \mathbf{y}_i + \phi g \quad (1.38)$$

where  $\mathbf{y}_i$  and  $\mathbf{y}_{i+1}$  denote the state vector at times  $t_i$  and  $t_{i+1}$ , respectively, and  $\phi$  is the representative slope over the current time step  $g$ . The increment function  $\phi$  is expressed as

$$\phi = a_1 \mathbf{k}_1 + a_2 \mathbf{k}_2 + \cdots + a_n \mathbf{k}_n \quad (1.39)$$

where the  $a$ 's are constants and the  $\mathbf{k}$ 's are individual slope estimates. Note that vector notation is used for the state variables and slope estimates. We use this notation because the Runge-Kutta Method can be used to simultaneously integrate a system of ordinary differential equations. The spacecraft's state vector that we integrate for the Hohmann transfer from Earth to Mars contains six elements, and therefore six simultaneous differential equations are solved.

We can use different types of Runge-Kutta methods by varying the number of terms in the increment function  $\phi$ . The Fourth-Order Runge-Kutta Method ( $n = 4$ ) has a global truncation error on the order of  $g^4$ . [3] Figure 1.7 offers an illustration of one iteration of the Fourth-Order Runge-Kutta Method. Using this method, we integrate the state variable as

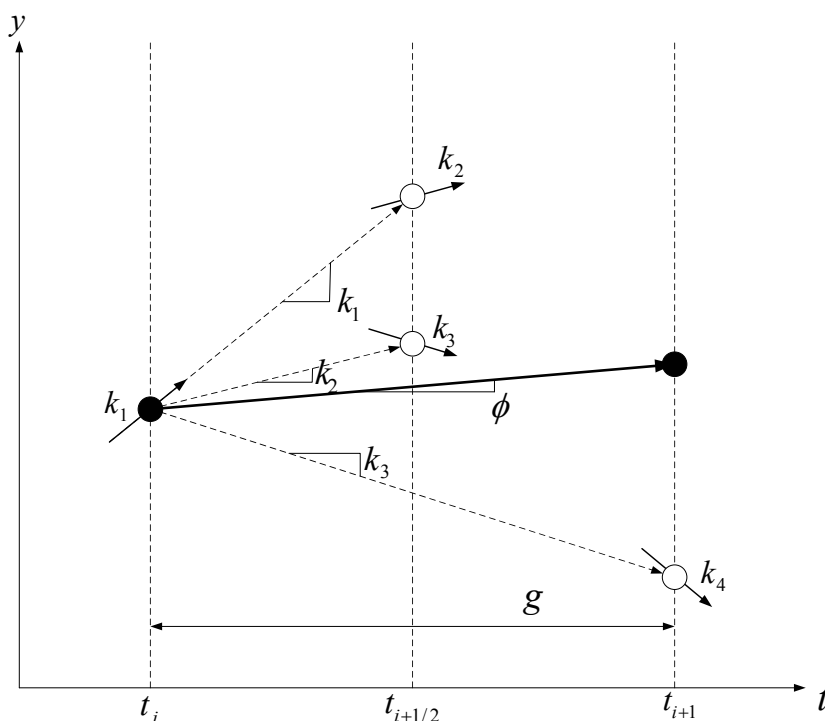


Figure 1.7: **Fourth-Order Runge-Kutta Method.** Illustration of the calculation of slope estimates during one iteration of the Runge-Kutta Method.

$$\mathbf{y}_{i+1} = \mathbf{y}_i + \frac{1}{6}(\mathbf{k}_1 + 2\mathbf{k}_2 + 2\mathbf{k}_3 + \mathbf{k}_4)g \quad (1.40)$$

where

$$\mathbf{k}_1 = \mathbf{f}(t_i, \mathbf{y}_i) \quad (1.41a)$$

$$\mathbf{k}_2 = \mathbf{f}\left(t_i + \frac{1}{2}g, \mathbf{y}_i + \frac{1}{2}\mathbf{k}_1g\right) \quad (1.41b)$$

$$\mathbf{k}_3 = \mathbf{f}\left(t_i + \frac{1}{2}g, \mathbf{y}_i + \frac{1}{2}\mathbf{k}_2g\right) \quad (1.41c)$$

$$\mathbf{k}_4 = \mathbf{f}\left(t_i + g, \mathbf{y}_i + \mathbf{k}_3g\right) \quad (1.41d)$$

and the weighting coefficients of Equation (1.39) have been given the values

$$a_1 = \frac{1}{6}, \quad a_2 = \frac{2}{6}, \quad a_3 = \frac{2}{6}, \quad a_4 = \frac{1}{6} \quad (1.42)$$

Because each of the  $\mathbf{k}$ 's represents a slope estimate, Equation (1.40) uses a weighted slope average to more efficiently determine the state vector at the future time  $t_{i+1}$ .

At this point, it must be noted that we can use a variable time step in order to improve the efficiency of the Runge-Kutta integrator. For instance, if the time step is increased for some portion of the integration, then the  $\mathbf{k}_i$  slope estimates are averaged over larger changes in time  $t_{i+1} - t_i$  during that portion. This variable time step is very convenient when applied to the restricted four-body problem. As the spacecraft travels through either Earth's or Mars' sphere of influence, it accelerates at a much greater rate than during the heliocentric portion of the mission. Therefore, it is very computationally efficient to increase the integration time step  $g$  during the heliocentric portion of the transfer orbit. The next section discusses how to implement the variable time step within the four-body algorithm.

### 1.3.3 Four-Body Algorithm

This section provides an explanation of the algorithm we use to integrate the spacecraft's state over the course of the transfer orbit. For a listing of the MatLab code used to execute the algorithm, please contact the author. As shown in Equation (1.31), the equations of motion of the spacecraft are nonlinear. We can express the initial value problem of any nonlinear system as

$$\dot{\mathbf{y}}(t) = \mathbf{f}(t, \mathbf{y}(t)), \quad \mathbf{y}(t_0) = \mathbf{y}_0, \quad a < t < b \quad (1.43)$$

where  $\mathbf{y}_0$  represents the vector of initial conditions and  $a$  and  $b$  denote the time limits of integration.[6] In the case of the Hohmann transfer, the state vector  $\mathbf{y}(t)$  and its inertial derivative  $\dot{\mathbf{y}}(t)$  are given by

$$\mathbf{y}(t) = \begin{pmatrix} x_1(t) \\ y_1(t) \\ 0 \\ \dot{x}_1(t) \\ \dot{y}_1(t) \\ 0 \end{pmatrix}, \quad \dot{\mathbf{y}}(t) = \begin{pmatrix} \dot{x}_1(t) \\ \dot{y}_1(t) \\ 0 \\ \ddot{x}_1(t) \\ \ddot{y}_1(t) \\ 0 \end{pmatrix} \quad (1.44)$$

After writing Equation (1.31) as a system of scalar equations and substituting into Equation (1.44), we find that

$$\dot{\mathbf{y}}(t) = \begin{pmatrix} \dot{x}_1(t) \\ \dot{y}_1(t) \\ 0 \\ -\frac{\mu_{\oplus}}{r_1^3}x_1 - \frac{\mu_{\oplus}}{r_2^3}x_2 - \frac{\mu_{\oplus}}{r_3^3}x_3 \\ -\frac{\mu_{\oplus}}{r_1^3}y_1 - \frac{\mu_{\oplus}}{r_2^3}y_2 - \frac{\mu_{\oplus}}{r_3^3}y_3 \\ 0 \end{pmatrix} \quad (1.45)$$

Thus, we have derived the rate of change of the spacecraft's state vector as a function of both its current state  $\mathbf{y}(t)$  and the current time  $t$ . We can now use the Fourth-Order Runge-Kutta Method to calculate the spacecraft's state vector over the course of the entire Hohmann transfer from Earth to Mars.

Once we establish the desired initial conditions and the appropriate time interval for the integration, we perform an iterative loop. For each time step of this loop, the following calculations are made:

- Use the current state vector and time to determine the  $\mathbf{k}_1$  slope estimate via Equation (1.45).
- 2. Use  $\mathbf{y}(t)$  and the computed value of  $\mathbf{k}_1$  to calculate the state at the midpoint of the interval  $g$  as

$$\mathbf{y}\left(t + \frac{g}{2}\right) = \mathbf{y}(t) + \mathbf{k}_1 \frac{g}{2} \quad (1.46)$$

- Use the current time  $t$  and the computed state vector at  $t + \frac{g}{2}$  to calculate the new slope estimate  $\mathbf{k}_2$ .
- Update the state vector at the midpoint of the interval by substituting  $\mathbf{k}_2$  into Equation (1.46).
- Repeat this process until all slope estimates  $\mathbf{k}_1$ ,  $\mathbf{k}_2$ ,  $\mathbf{k}_3$ , and  $\mathbf{k}_4$  have been determined.
- Calculate the increment function  $\phi$  as a weighted average of the four slope estimates, via Equation (1.39).
- Use the current state vector  $\mathbf{y}(t)$  and the weighted slope estimate  $\phi$  to calculate the future state  $\mathbf{y}(t + h)$  as in Equation (1.40).

We use a variable time step  $g$  to increase the speed of integration. The spacecraft acceleration is greatest as it travels through the spheres of influence of Earth and Mars. Therefore, we set the planet-centric time step  $g_h$  to a lower value as the spacecraft travels through each sphere of influence. In fact, to be conservative, we implement the smaller time step  $g_h$  whenever the craft is within 1.5 times the sphere of influence of either Earth or Mars. Using a smaller time step for both the hyperbolic departure and arrival orbits allows us to accurately integrate the two portions of the transfer that are most sensitive to integration error. During the heliocentric portion of the trip, we implement a larger time step  $g_e$  in order to improve computational efficiency. The integration process does not require as small

a time step during the elliptic orbit because the craft does not accelerate to the extent that it does during the hyperbolic orbits. For the specific case of the planar Hohmann transfer from Earth to Mars, the time step  $g_e$  can be at least 1000 times greater than  $g_h$ . Even with such a large difference between the two time step values, the transfers achieved are roughly identical to those that result from using the smaller step  $g_h$  throughout the entire orbit. Thus, using a variable time step allows us to greatly improve computational efficiency without sacrificing integration accuracy.

As previously stated, please contact the author to request the MatLab code used to run the iterative loop. The code contains the functions used to integrate the circular motion of both Earth and Mars about the sun. Now that we have established how the four-body integrator works, we check the validity of its output.

### 1.3.4 Validity Check

Before using the Runge-Kutta integrator to examine the restricted four-body problem, we first perform a checks upon the integrator results. It must be noted at this point that, unless stated otherwise, the initial offset angle between Earth and Mars used during integration is that solved for in section 1.2.1 (44.343 degrees). In order to perform the first check, we set the initial state of the spacecraft such that it should maintain a relatively circular orbit about Earth during the entire period of integration. We assign the critical velocity  $\nu_c$  of 7.290 km/s at the initial parking orbit radius of 7500 km. Figure 1.8 displays the motion of the spacecraft relative to Earth during the orbit. As expected, the spacecraft does not

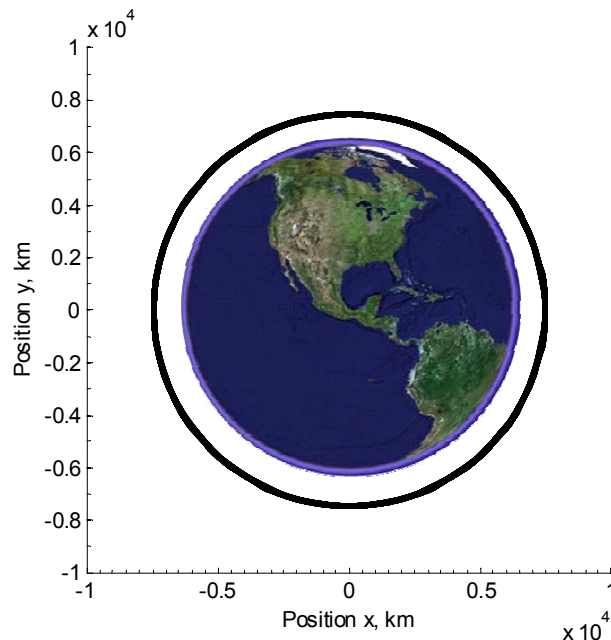


Figure 1.8: **Critical Orbit Integrator Check.** Check on a critical orbit about Earth with an initial altitude of 7500 km. The  $x$  and  $y$  positions are taken relative to the center of the non-rotating Earth frame  $\mathcal{E}$ .

appear to deviate substantially from an altitude of 7500 km. But we must still focus on a smaller portion of the orbit in order to determine how much the spacecraft deviates from an altitude of 7500 km. Figure 1.9 displays a small portion of the nearly-circular orbit for two different planet-centric step sizes  $g_h$ . For a step size of 100 seconds, the spacecraft stays

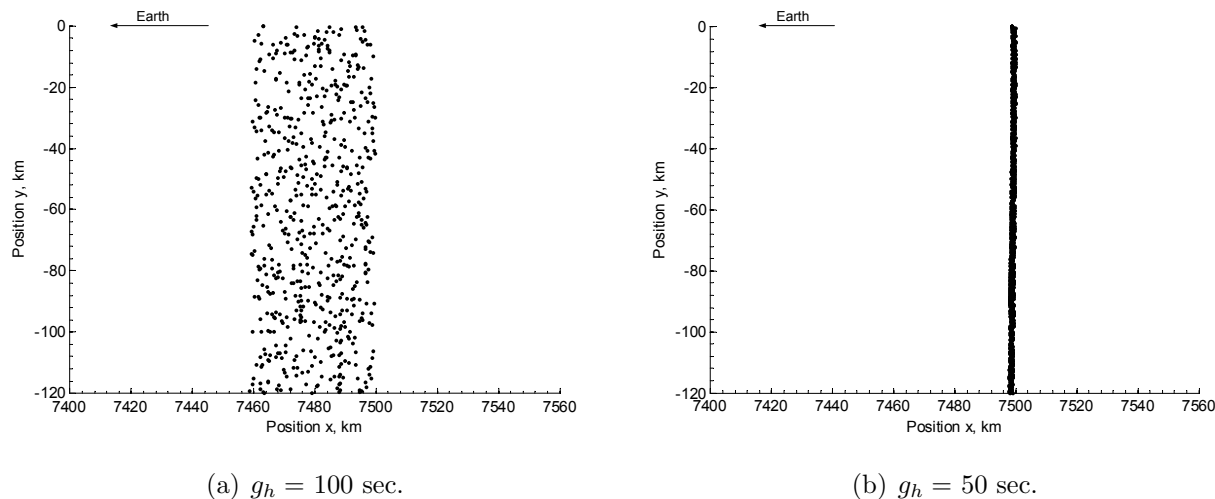


Figure 1.9: **Integration Time Step Validation.** Illustration of the variation in altitude during a critical orbit about Earth. The  $x$  and  $y$  positions are taken relative to the center of the non-rotating Earth frame  $\mathcal{E}$ .

within roughly 40 km of its initial 7500 km orbit radius. But when the step size is halved to 50 seconds, the motion of the spacecraft deviates only 3 km from the 7500 km radius. Thus, the error accrued in Figure 1.3.4 is most likely round-off error due to the size and precision limits of the integrator itself. Once the step size is set to 50 seconds, the spacecraft stays within 0.04 percent of its initial orbit radius. These results seem reasonable, as we expect the orbit radius to deviate slightly from its initial value due to the small gravitational influences of the sun and Mars.

After performing a check on the validity of the Runge-Kutta integrator, we now use it to examine the application of the four-body problem to a Hohmann transfer from Earth to Mars. We are interested in how the analytical solutions of the patched-conic approximation compare with the actual output of the integrator. In addition, we determine the effect of varying the initial conditions upon the development of the transfer. Thus, we can comment on the advantages and disadvantages of various orbit setups.

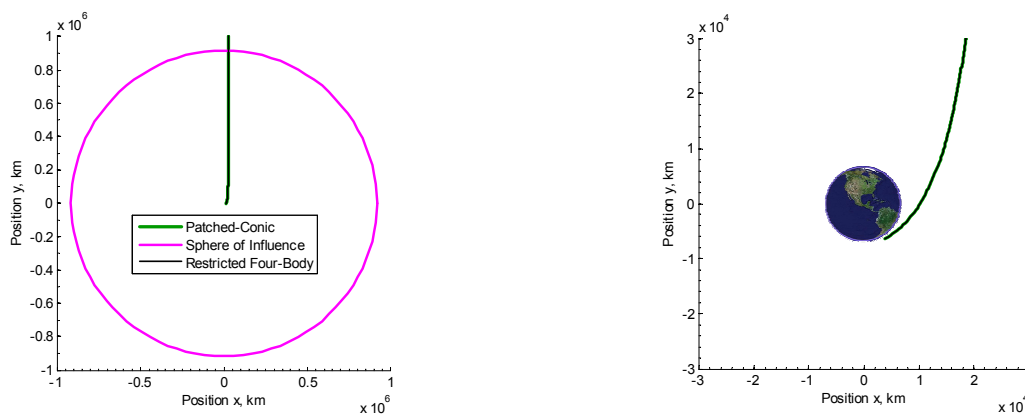
## 1.4 Integration Results

### 1.4.1 Comparison of the Patched-Conic and Restricted Four-Body Solutions

As noted in Chapter 1.2, the patched-conic approximation essentially partitions the overall transfer orbit into three separate two-body problems. During the first portion of the mission,

we assume that the Earth provides the only gravitational influence upon the spacecraft. After the craft leaves Earth’s sphere of influence, we then assume the sun to provide the sole gravitational influence. Once the spacecraft has entered Mars’ sphere of influence, we treat Mars as the only source of gravitational force.

We first analyze the spacecraft’s motion through Earth’s sphere of influence for both the patched-conic approximation and the restricted four-body solution. We have already seen the development of a Runge-Kutta integrator for the restricted four-body problem. Using the same process, we develop a Runge-Kutta integrator to integrate the spacecraft’s departure orbit as a simpler two-body problem. Having both the four-body and two-body integrators, we can compare the spacecraft’s motion for the two cases. We set the initial parking orbit radius and the elliptic semi-major axis to be 7500 km and 1.8877e+008 km, respectively. These initial conditions match those used in Chapter 1.2 to apply the patched-conic approximation to the Hohmann transfer from Earth to Mars. In addition, we set the time step  $g_h$  to 50 seconds for the transfer orbit. Figure 1.10 illustrates the integrated solutions for both the two-body and four-body problems. As shown by Figure 1.10, the



(a) Motion through Earth’s entire sphere of influence. (b) Close-up of the first stages of the departure.

Figure 1.10: **Patched-Conic and Four-Body Motions.** Comparison of the patched-conic and restricted four-body predictions of the spacecraft’s motion through Earth’s sphere of influence. Positions  $x$  and  $y$  are relative to the center of the Earth frame  $\mathcal{E}$ .

patched-conic approximation basically matches the spacecraft motion under the restricted four-body problem. In both cases, the spacecraft leaves Earth’s sphere of influence with a heliocentric velocity in the same direction as that of the Earth. Thus, the results support the patched-conic prediction of a departure velocity  $\mathbf{v}_1$  parallel to the Earth’s heliocentric velocity  $\mathbf{v}_\oplus$ .

Using the same initial conditions ( $r_0 = 1500$  km,  $a_e = 1.8877\text{e}+008$  km), we now examine the spacecraft’s motion during the entire Hohmann transfer. With a step size  $g_h$  of 50 seconds, we use the Runge-Kutta integrator to calculate the spacecraft’s state over the transfer orbit. Figure 1.11 displays a plot of the integrated orbit from Earth to Mars. The patched-conic approximation predicts that the spacecraft’s trajectory will be an perfect

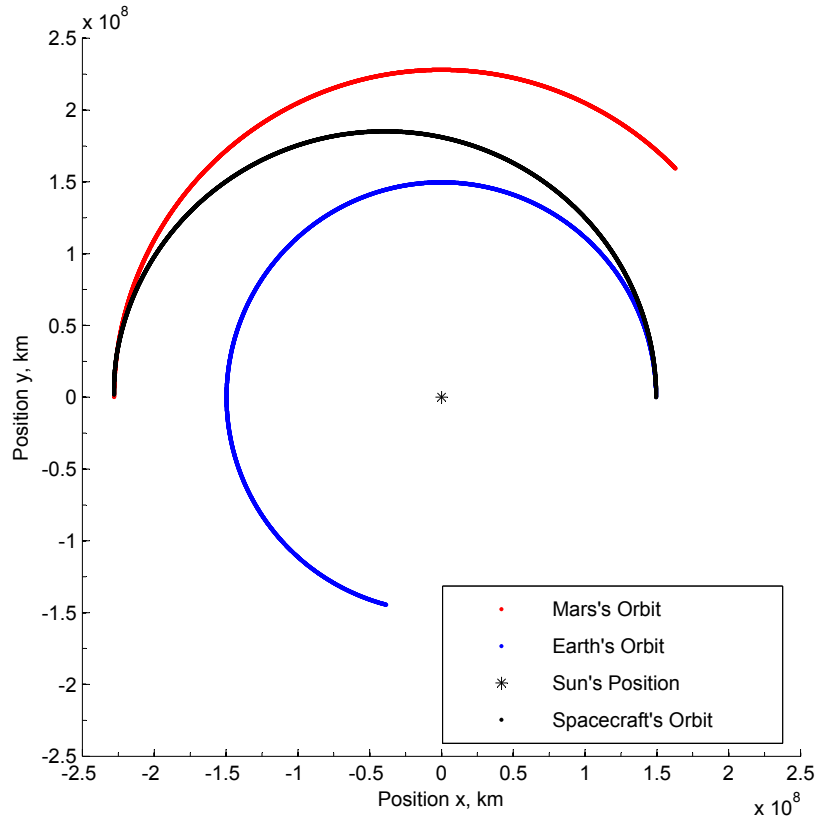
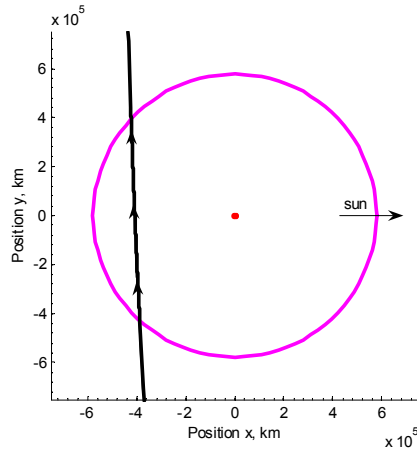


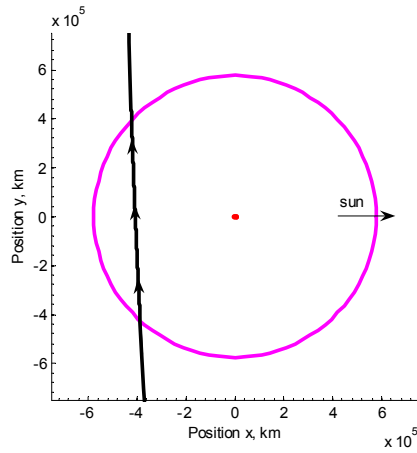
Figure 1.11: **Restricted Four-Body Heliocentric Motion.** Illustration of the spacecraft's heliocentric motion during the entire Hohmann transfer. Step size used with the four-body integrator is  $g_h = 50$  seconds.

ellipse with a semi-major axis  $a_e$  equal to  $1.8877e+008$  km. As shown by Figure 1.11, this is a good prediction when we analyze the motion on heliocentric orders of magnitude. The spacecraft's transfer orbit does indeed appear to be almost a perfect ellipse. At this point, it must be noted that the actual semi-major axis of the transfer will be slightly different from that used to graph Figure 1.11. The difference comes from the fact that the spacecraft performs the departure burn at some offset distance from the center of the Earth. The patched-conic approximation ignores this minute detail, but we will study its effects upon the arrival orbit in a later section.

We are also interested in the spacecraft's motion during its arrival orbit through Mars' sphere of influence. Thus, using the same initial conditions and the same integrator, we plot the spacecraft's motion relative to Mars. Figure 1.12 displays the planet-centric trajectory of the spacecraft. As Figure 1.12 shows, the Hohmann transfer enters Mars' sphere of influence at a Mars-centric heading angle  $\vartheta_2$  that is very close to 180 degrees. If the spacecraft were on a perfect Hohmann transfer, the  $\vartheta_2$  heading angle would be exactly equal to 180 degrees, given its definition in Figure 1.4. It is reassuring to know that the restricted four-body problem yields a transfer orbit that does enter the Martian sphere of influence. Further, the heading angle upon entry is very similar to that of a perfect Hohmann transfer. As predicted



(a)  $g_h = 50$  sec.



(b)  $g_h = 25$  sec.

Figure 1.12: **Restricted Four-Body Arrival Orbit.** Illustration of the spacecraft's arrival orbit through Mars' sphere of influence.

by the patched-conic approximation, the spacecraft enters the sphere of influence from the front door. In other words, Mars intercepts the spacecraft at the end of the transfer.

Perhaps the most important feature of Figure 1.12 is the similarity between the two graphs. Halving the planet-centric time step  $g_h$  from 50 to 25 seconds has roughly no effect on the spacecraft's arrival orbit. Therefore, we can set the planet-centric time step to be at least 50 seconds without sacrificing significant accuracy. For the orbits shown in Figure 1.12, the heliocentric time step  $g_e$  is maintained at 50000 seconds.

While the spacecraft does stay within Mars' sphere of influence, it also overshoots the planet by roughly  $4e+005$  kilometers. At first, such a result would seem counter-intuitive. The spacecraft actually begins its orbit slightly farther away from the sun than if it were to begin a perfect Hohmann transfer directly from Earth's surface. However, as the spacecraft's initial position shifts slightly farther away from the sun, we do not alter the calculation of the initial escape velocity  $\nu_0$ . When we view the problem from the heliocentric point of view,

we recognize that the spacecraft does not require as much initial speed when beginning the orbit slightly farther away from the sun. Such a statement can be proved by applying the conservation of angular momentum to the elliptic heliocentric orbit. Therefore, because we keep the same  $\nu_0$  at a larger distance from the sun, the spacecraft is expected to overshoot Mars by some miss distance  $d_m$ .

In many respects, the four-body integration supports the patched-conic approximations given in Chapter 1.2. The hyperbolic departure orbit is identical for the two- and four-body scenarios. The integrated Hohmann transfer to Mars' sphere of influence closely matches a perfect ellipse. Perhaps most importantly, the spacecraft penetrates Mars' sphere of influence in same fashion predicted by the patched-conic approximation. The results support the validity of using the patched-conic approximation as a rough estimate of the  $\Delta v_1$  needed to perform the Hohmann transfer. Having compared the two- and four-body problems as well as their results, we now analyze the effect of changing certain initial conditions of the transfer orbit. Of particular interest is how the arrival orbit is altered due to the changes in initial conditions.

## 1.4.2 Altering the Initial Conditions

### Changing the Mars Offset Angle

As discussed in Chapter 1.2, there must exist some initial offset angle  $\gamma(t_1)$  between Earth and Mars. If there were no initial offset angle, the spacecraft would perform the Hohmann transfer without ever entering Mars' sphere of influence. Up to this point, we have performed all numerical integrations with the initial offset angle computed in Chapter 1.2 (44.343 degrees). By changing this initial offset angle, we can examine the effect that it has upon the hyperbolic arrival orbit. Thus, we perform a series of restricted four-body integrations, varying this offset angle  $\gamma(t_1)$ . Figure 1.13 displays a group of arrival orbits for six different Mars offset angles. The planet-centric step size used to integrate the six different cases is 50 seconds. At this point we are most concerned with the relative geometries of the orbits depending upon the initial Mars offset angle. As shown by Figure 1.12, a step size  $g_h$  of 50 seconds is small enough to accurately give us the relative geometries. Figure 1.13 illustrates that increasing the initial offset angle  $\gamma(t_1)$  affects the hyperbolic arrival orbit in two ways. It noticeably varies the miss distance  $d_m$  between the spacecraft's projected trajectory and the sun direction. As  $\gamma(t_1)$  is increased from 44.343 to 44.843 degrees, the miss distance decreases and the eccentricity of the hyperbolic arrival increases. But for all of these orbit geometries, the spacecraft orbits Mars in a clockwise fashion. Once  $\gamma(t_1)$  surpasses 44.843 degrees, the spacecraft begins performing counter-clockwise orbits about Mars. This effect is particularly important if we want to ultimately have a geostationary orbit about Mars. In such a case, we would need to be orbiting Mars in the same direction as the planetary rotation.

Secondly, the changes in initial offset angle  $\gamma(t_1)$  have a slight effect upon the arrival heading angle  $\sigma_2 + \vartheta_2$ . Note that, as the offset angle is increased from 44.343 to 45.031 degrees, the heading angle decreases from its initial value of roughly 180 degrees. The reason for this slight decrease in heading angle is that the spacecraft is now penetrating Mars' sphere of influence at an earlier time on its Hohmann transfer. Thus, the heading

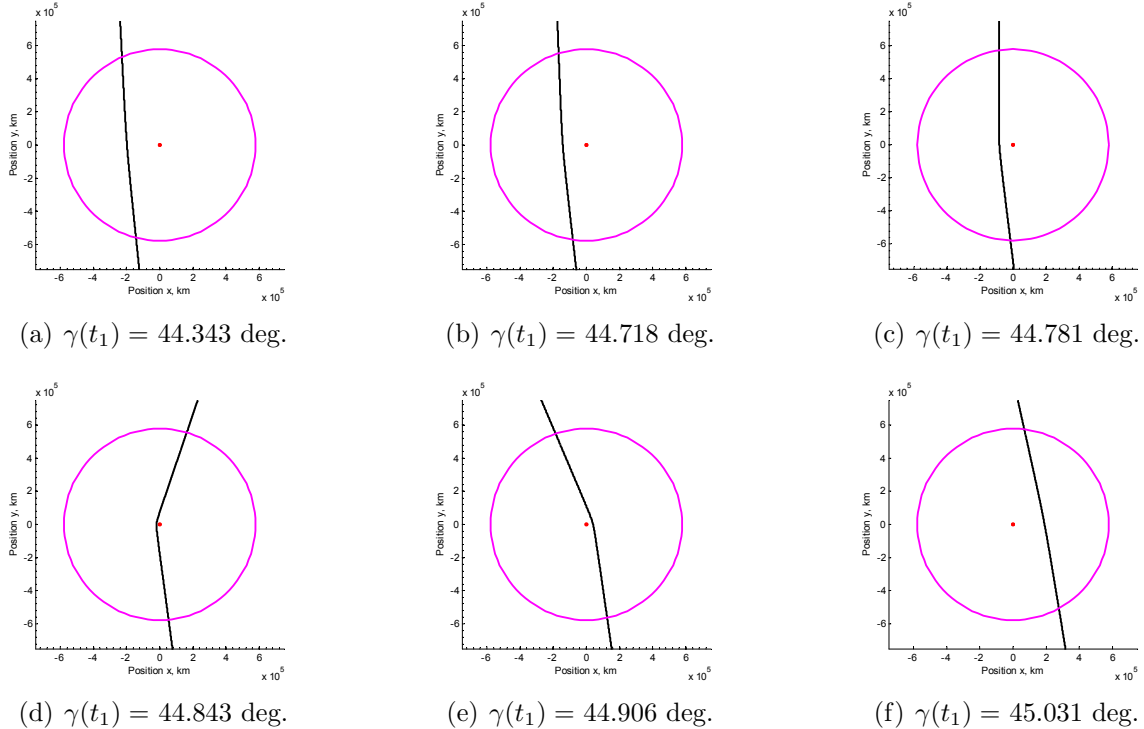


Figure 1.13: **Arrival Orbits Corresponding to Initial Offset Angle Variations.** Series of hyperbolic arrival orbits corresponding to six different initial offset angles between Earth and Mars. The  $x$  and  $y$  positions are taken relative to the Mars-centered frame  $\mathcal{M}$ . The step size  $g_h$  used is 50 seconds.

angle begins to regress from the ideal value of 180 degrees for a perfect Hohmann transfer.

### Changing Mars' Heliocentric Orbit Radius

As noted in Section 1.4.1, when we use the patched-conic approximation to estimate the necessary initial conditions for the Hohmann transfer, the arrival orbit overshoots Mars by roughly  $4e+005$  kilometers. Therefore, if we want to achieve a certain hyperbolic periapsis radius  $r_3$  about Mars, we must alter at least one initial condition. Referring to the patched-conic arrival orbit solutions presented in Section 1.2.4, we find that the  $r_3$  parking radius depends upon the miss distance  $d_m$  and the velocity  $\boldsymbol{\nu}_2$ . Equation (1.24) gives the relation between the actual miss distance  $d_m$  and the perpendicular miss distance  $d_a$ . The planar Hohmann transfer from Earth to Mars will always yield a planet-centric velocity  $\nu_2$  roughly equal to 2.648 km/s, as calculated in Section 1.2.4. Thus, to achieve a specific parking orbit radius about Mars, we can alter the miss distance  $d_a$  until the necessary arrival geometry is obtained. One way to alter the miss distance  $d_a$  of the arrival hyperbola is to make small changes in Mars' heliocentric orbit radius. For instance, if the spacecraft overshoots Mars by too great a distance, we subtract the extra miss distance from Mars' orbit radius and iterate the same Hohmann transfer. Using such a method, we can determine what Martian heliocentric orbit radius will yield the miss distance  $d_a$  corresponding to our desired parking radius  $r_3$ . Figure 1.14 offers a flow chart illustrating the  $r_\sigma$  correction process.

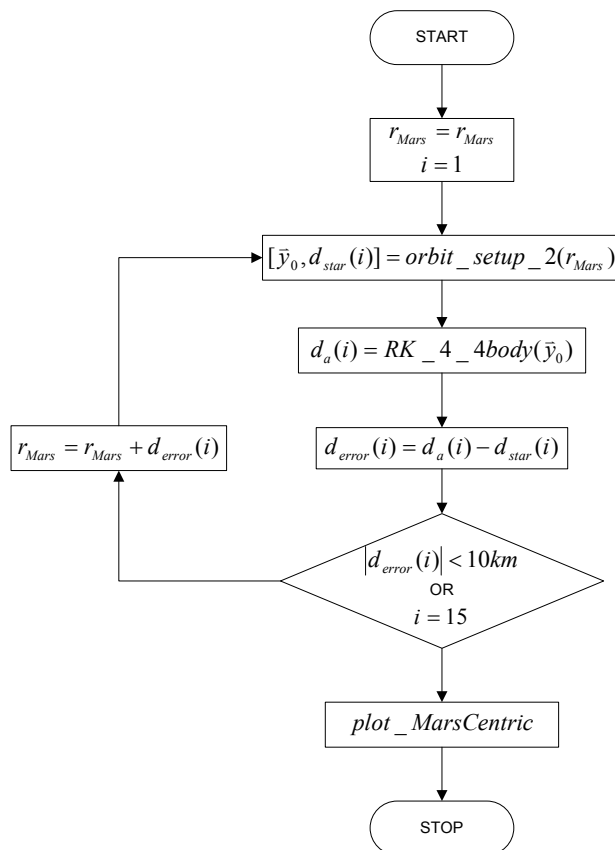


Figure 1.14: **Semi-Major Axis Correction Algorithm.** Flow chart depicting the loop used to iteratively correct Mars’ orbit radius  $r_{\mathcal{O}}$  in order to achieve the desired arrival parking radius  $r_3$  about Mars.

The advantage of using a variable time step is accentuated when we perform the given iteration to determine a unique arrival orbit geometry. In performing the iteration, we are integrating the Hohmann transfer a number of times in order to analyze changes in the arrival hyperbola. Thus, being able to quickly integrate the heliocentric portion of each Hohmann transfer is a valuable asset. Figure 1.15 offers an illustration of both the corrected and uncorrected arrival orbit geometries. For the iterations performed, we set the desired Mars parking radius  $r_3$  to 4000 km. The initial iteration yields a miss distance of roughly  $4e+005$  kilometers. But after seven iterations are performed, the miss distance is almost exactly equal to the necessary value  $d_{star}$  of 8142 kilometers. Both graphs of Figure 1.15 show the projection of the  $\nu_2$  velocity upon entry into Mars’ sphere of influence as a blue line. We use this projection to then calculate the perpendicular distance to the center of Mars, corresponding to the actual miss distance  $d_a$ . Table 1.1 offers a listing of the actual distance  $d_a$ , necessary distance  $d_{star}$ , and distance error  $d_{error}$  for each iteration.

Note that by the seventh iteration, the magnitude of  $d_{error}$  has dropped below 1 kilometer. Figure 1.15 illustrates how the seventh iteration yields an arrival orbit with a periapsis radius  $r_3$  of roughly 4000 kilometers. Thus, we have taken the restricted four-body problem and found one set of initial conditions that result in a desired final parking orbit radius

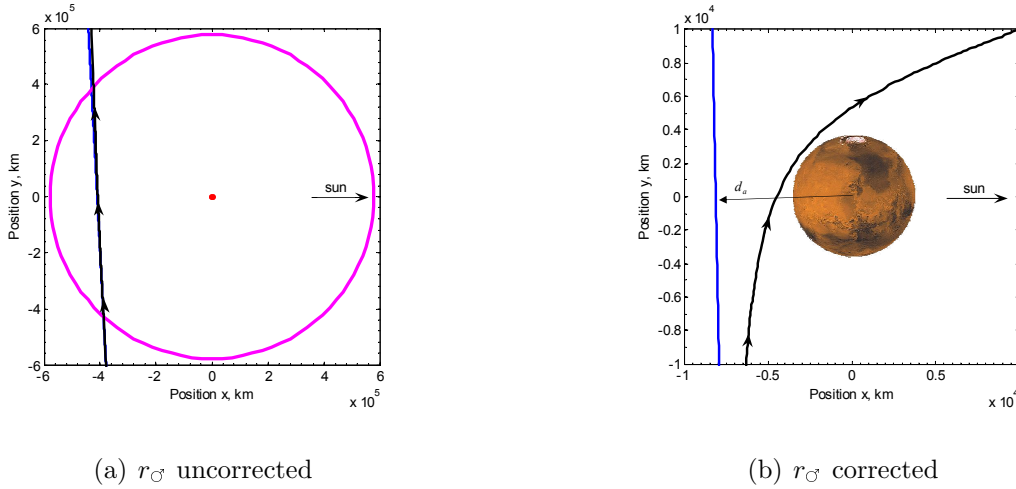


Figure 1.15: **Semi-Major Axis Correction Results.** Illustration of both the uncorrected and corrected arrival orbit geometries for the Mars orbit radius iteration. Values  $x$  and  $y$  are defined relative to the non-rotating Mars frame  $\mathcal{M}$ . Seven iterations were performed before achieving the final corrected arrival.

Table 1.1: **Semi-Major Axis Correction Scheme Miss Distance Values.** Table of miss distance values calculated during each iteration of the Mars orbit radius correction scheme.

Iteration	$d_a$ , km	$d_{star}$ , km	$d_{error}$ , km
1	-4.09519e+005	-8.05389e+003	-4.01465e+005
2	-9.34220e+004	-8.12439e+003	-8.52976e+004
3	-1.95337e+004	-8.13963e+003	-1.13941e+004
4	-9.49786e+003	-8.14167e+003	-1.35619e+003
5	-8.30000e+003	-8.14192e+003	-1.58085e+002
6	-8.16003e+003	-8.14194e+003	-1.80811e+001
7	-8.14283e+003	-8.14195e+003	-8.83155e-001

about Mars. Table 1.1 also offers a listing of the necessary miss distance  $d_{star}$  values for each iteration. We iterate the necessary miss distance value because the arrival speed  $\nu_2$  is altered slightly for each new value of the Mars orbit radius. Because the changes in  $\nu_2$  for each iteration are so small, the magnitude of  $d_{star}$  changes only slightly. By the fifth iteration, the value of  $d_{star}$  has already reached its approximate final value of  $-8.1419e+003$  km. Figure 1.16 offers a plot of the miss distance error magnitude for the Mars orbit radius correction process. After three iterations, most of the correction to Mars' orbit radius  $r_\sigma$  has already been made. Between iterations three and seven, much smaller corrections are made to Mars' orbit radius, and the corrections in the error  $d_{error}$  are therefore also much less.

Our iteration yields an orbit with a periapsis radius about Mars roughly equal to the desired value of 4000 km. But the spacecraft rotates about Mars in a retrograde fashion. If we desire the same periapsis radius, but corresponding to a posigrade rotation about Mars, we would need to change the necessary miss distance  $d_{star}$  to a positive value. However, in

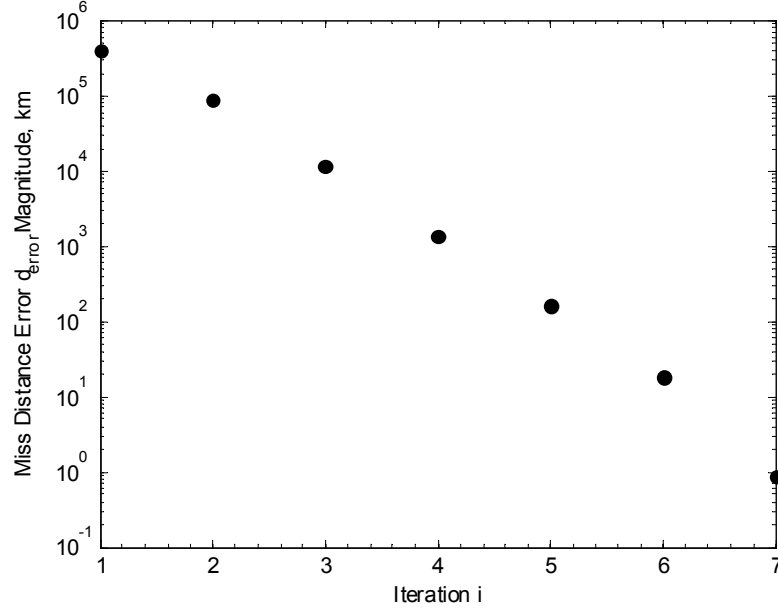


Figure 1.16: **Semi-Major Axis Correction Miss Distance Errors.** Graph of the miss distance error magnitude  $d_{error}$  for each step of the Mars orbit radius correction scheme.

doing so, we would need to alter the first correction of Mars' orbit radius to be sure that the second iteration does not yield an orbit that strikes Mars' surface. This singularity would significantly change the results of the iterative process. One suggestion for iterating to yield a posigrade orbit is to over-correct the first Mars orbit radius. Once the  $r_{\mathcal{C}}$  orbit radius has been over-corrected, we can then iterate using the method explained in this section to yield the desired periapsis radius  $r_3$ .

### 1.4.3 Comparison of Predicted $\Delta v$ Values

So far, we have analyzed three different ways to estimate the necessary  $\Delta v$  value to travel from Earth to Mars on a Hohmann transfer. We first view the transfer orbit as a single elliptic orbit with a change in true anomaly of 180 degrees. Such an approximation treats the sun as the only gravitational influence upon the spacecraft during the transfer. The gravitational effects of both Earth and Mars are ignored entirely.

Our second representation of the Hohmann transfer is as a series of two-body orbits about Earth, the sun, and Mars, respectively. Because we represent each portion of the orbit as a conic solution, we term this solution the patched-conic approximation. The patched-conic approximation allows us to take into account the gravity of Earth and Mars as the spacecraft travels through the planets' spheres of influence. However, this approximation ignores the gravitational effects of the planets when the spacecraft is traveling outside of their spheres of influence. The patched-conic approximation yields a better estimate of the  $\Delta v$  required to reach Mars than the simple Hohmann solution. This better estimate results from taking into account the gravitational influence of Earth as the spacecraft performs its hyperbolic departure orbit.

The final representation of the transfer orbit is as a restricted four-body orbit. Thus, we

Table 1.2: **Comparison of  $\Delta v$  Estimates for the Hohmann Transfer.** Table showing the differences in required  $\Delta v$  estimates for the Hohmann transfer, patched-conic approximation, and restricted four-body problem. The value of  $\Delta v$  for the four-body approximation corresponds to a desired Mars parking orbit radius  $r_3$  of 4000 km.

Orbit Approximation	$\Delta v$ (km/s)
Hohmann Transfer	2.943
Patched-Conic	3.432
Restricted Four-Body	3.428

take the gravity of Earth, the sun, and Mars into consideration for the duration of the entire transfer orbit. We also examine the effects of altering certain departure orbit conditions upon the nature of the arrival orbit. More specifically, we determine the required  $\Delta v$  to achieve a particular periapsis radius  $r_3$  about Mars. Such a calculation cannot be made when examining the orbit using either the Hohmann approximation or the patched-conic approximation. Table 1.2 provides a listing of the  $\Delta v$  estimates corresponding to each of the three Hohmann transfer representations.

Note that the difference in required  $\Delta v$  values lies mostly in going from the general Hohmann approximation to the patched-conic approximation. There exists only a 0.004 km/s difference in the  $\Delta v$  values for the patched-conic approximation and the restricted four-body problem. However, integrating the restricted four-body problem allows us to confirm that this seemingly minute difference allows us to achieve a desired Mars periapsis radius of 4000 km. Such minute details become extremely important when attempting to establish a true interplanetary mission plan.

## 1.5 Conclusions

The original analytic solution to the Hohmann transfer from Earth to Mars offers a crude estimate of the  $\Delta v$  required to perform the transfer. Because it neglects the gravitational effects of both Earth and Mars, this orbit solution cannot achieve the same accuracy as the patched-conic approximation. However, this simple orbit representation does provide a suitable rough estimate of the initial burn required to reach Mars' sphere of influence.

The patched-conic approximation provides a much better estimate of the  $\Delta v$  required to reach Mars on a Hohmann transfer. Its consideration of the planets' gravitational influences as the spacecraft travels through their spheres of influence makes this solution much more credible than the simple Hohmann solution. By breaking the entire orbit into three separate conic solutions, we can begin to see the effects of the departure orbit geometry on both the elliptic transfer and hyperbolic arrival. However, the patched-conic approximation does not allow us to alter certain departure orbit conditions and see the direct effect upon the arrival. Instead, we must solve each of the three conic solutions as separate orbits.

The restricted four-body integration scheme allows us to view the Hohmann transfer from Earth to Mars as one entire orbit. Thus, while taking into consideration the gravity of Earth, the sun, and Mars for all time, we can analyze the effects of altering certain initial conditions upon the arrival orbit. In addition, we can determine the necessary departure burn

to achieve a desired parking orbit radius  $r_3$  about Mars. The patched-conic approximation does not allow for such precise orbit modeling. Treating the Hohmann transfer as a restricted four-body problem yields an even higher fidelity representation of the transfer orbit.

One idea for future work is to examine the applicability of the established four-body integrator to other interplanetary missions. Such missions need not necessarily be Hohmann transfers. They could also lead to arrivals at a different planet from Mars. The sensitivity of the four-body integrator to perturbations of these different orbits could then be analyzed. Still other future work could focus on increasing the accuracy of the presented four-body orbit modeling scheme. For instance, atmospheric drag is a disturbance that must be considered for both the departure and arrival orbits. In addition, the planar orbit assumption could be dropped by taking into account the slight orbit inclination difference between Earth and Mars. The spacecraft would then have a full three-dimensional state vector to be integrated over the course of the transfer. In short, much work remains in yielding an orbit modeling scheme that presents what would actually occur in a real-time transfer from Earth to Mars.

# Chapter 2

## Application of Sensitivities to the Restricted Four-Body Problem

### 2.1 Introduction

The objective of this chapter is to present the use of sensitivities as a method for developing interplanetary trajectories. The interplanetary trajectory focused on during this paper is a Hohmann transfer from Earth to Mars. A restricted four-body setup is used to describe the motion of the spacecraft. Both Earth's and Mars' orbits are constrained to be circular. The only gravitational forces taken into consideration are those of the sun, Earth, and Mars on the spacecraft. In addition, all orbits are constrained to be planar. As previously shown by Reppert, the restricted four-body orbit setup yields a more accurate representation of the Hohmann transfer than the patched-conic approximation.[10]

The Hohmann transfer was already computed using initial conditions derived from the patched-conic approximation.[11] This paper presents an analysis of how sensitivities may be used to refine the initial propagation of the transfer orbit. These refinements are used to provide desired arrival orbit conditions, such as a chosen Mars periapsis radius. The sensitivities are computed both analytically and numerically. The analysis provides an approximation to how perturbations in initial conditions of the departure orbit affect the arrival orbit geometry. Such information is valuable when trying to attain a particular arrival orbit.

Before assessing sensitivities of the four-body problem, the paper begins with a discussion of coding the four-body integrator in both Matlab and C. The advantages and disadvantages of using each language to perform the four-body integration are given. Thereafter, Section 2.3 provides an analysis of state transition matrices and their relation to sensitivity matrices. The analysis given in Section 2.3 is an introduction to the concept of sensitivities. This introduction provides preparation for the application of sensitivities to the four-body problem in Section 2.4.

The two sensitivities that are used to examine the restricted four-body problem are  $\frac{\partial d_a}{\partial \nu_0}$  and  $\frac{\partial r_3}{\partial \nu_0}$ . The variable  $\nu_0$  is the Earth-relative departure speed, whereas  $d_a$  and  $r_3$  are the arrival miss distance and periapsis radius, respectively. These sensitivities are computed both analytically and numerically in order to provide a means of attaining a desired arrival orbit geometry. The convergence performances of the perturbation methods are compared

by the computation time required to achieve a particular accuracy.

## 2.2 Converting Code from Matlab to C

Last year, a set of Matlab code was used to propagate the spacecraft's Hohmann transfer from Earth to Mars. This set of code is displayed in the appendix of the corresponding semester report.[11] Using Matlab's many built-in functions helped make the coding process easier to understand. However, the user-friendly advantages of coding in Matlab came at a cost.

The last objective of this past semester's research was to optimize the Hohmann transfer from Earth to Mars. In order to perform this optimization, multiple integrations of the transfer orbit were required. As is shown in the semester report, seven iterations of the Runge-Kutta integration were necessary to reach the stopping criterion for the Martian periapsis optimization.[11] Computing seven iterations of the orbit took approximately two minutes in Matlab. It was realized that, in order to compute any lengthier orbit optimizations, coding in another language would be much more efficient. The C programming language was chosen as the tool to be used for computing the lengthier optimization problems.

Having a previously developed set of Matlab code allowed for an easier transition to the C code. If a certain function in C did not provide the expected output, its contents could be checked in a line-by-line fashion with the corresponding Matlab code. In this manner, a set of C code was developed to complement the previously developed Matlab code. A listing of the C code may be requested from the author.

The only critical difference between the contents of the Matlab code and the C code is the method used to calculate the miss distance  $d_a$  of the arrival orbit. The Matlab code utilizes the built-in function `polyfit` to perform a linear regression on the spacecraft's position relative to Mars upon entering the sphere of influence. A total of 10 points are used to calculate the linear fit of the spacecraft's propagated position.

In contrast, the C code uses the value of the spacecraft's velocity vector upon entering Mars' sphere of influence to calculate the miss distance  $d_a$ . Figure 2.1 provides an illustration of the geometry. As the spacecraft crosses Mars' sphere of influence, the its velocity is propagated tangentially as follows:

$$y_{\text{tan}} = r_{s_y} + \frac{v_{s_y}}{v_{s_x}}(x_{\text{tan}} - r_{s_x}) \quad (2.1)$$

where  $\mathbf{r}_s$  and  $\mathbf{v}_s$  denote the spacecraft's position and velocity relative to Mars, respectively. However, problems can arise when the value of  $v_{s_y}/v_{s_x}$  becomes large. In the case of the Hohmann transfer, the value of this slope will always be large (as shown in Figure 2.1). Therefore, a better way to create the tangential extension of the velocity vector is to use  $x_{\text{tan}}$  as the dependent variable. The velocity vector is then propagated as

$$x_{\text{tan}} = r_{s_x} + \frac{v_{s_x}}{v_{s_t}}(y_{\text{tan}} - r_{s_y}) \quad (2.2)$$

Equation (2.2) is a more reliable way of calculating the linear extension of the velocity vector. The value of the slope  $v_{s_x}/v_{s_y}$  is always less than one for the Hohmann transfer.

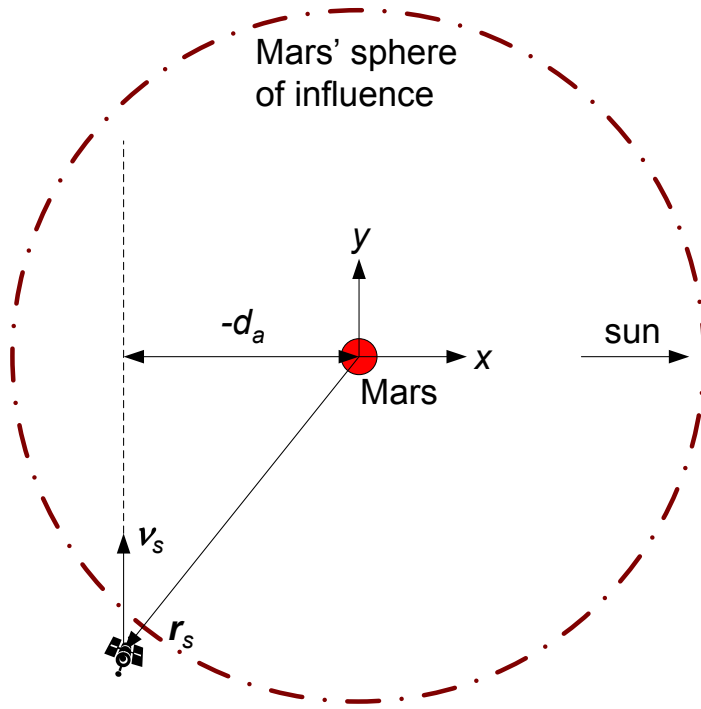


Figure 2.1: **Setup for the C Miss Distance Calculation.** Depiction of the arrival orbit geometry used to derive the C miss distance  $d_a$  calculation algorithm.

Once the velocity propagation is complete, the perpendicular miss distance  $d_a$  may be computed as the minimum distance between the center of Mars and the propagated velocity. This process for calculating the miss distance is more accurate than the process previously used in the Matlab code. The increase in accuracy is due to using the actual velocity vector instead of an approximated velocity vector to create the linear fit.

Most importantly, the C code computes the same optimization that took Matlab two minutes in approximately 10 seconds. This savings in time is critical when attempting to perform sensitive optimization problems. Matlab is valuable for computing and visualizing one transfer orbit, whereas C is valuable for calculating multiple transfer orbits in a computationally intense optimization problem. For a listing of the C code used to perform the sensitivity analyses discussed in Section 2.4, contact the author at [treppert@vt.edu](mailto:treppert@vt.edu).

## 2.3 State Transition Matrices

Sensitivity matrices provide a description of how perturbations of one variable cause changes in the value of another variable. The state transition matrix  $[\Phi(t, t_0)]$  is a particular type of sensitivity matrix that describes how perturbations of an initial state vector  $\mathbf{r}(t_0)$  lead to changes in the final state vector  $\mathbf{r}(t)$ . The state transition matrix can be seen as the sensitivity matrix of the current state to the initial conditions. One of the many applications of this matrix is to calculate how initial trajectory errors evolve over time.[13] This appli-

ation is later discussed with respect to the interplanetary transfer optimization problem. Chapter 2.3 presents fundamental state transition matrix theory as it applies to linear, homogeneous dynamic systems. The theory given is later extended to perform optimizations of the restricted four-body problem.

### 2.3.1 Linear, Homogeneous Dynamic Systems

Consider the homogeneous vector-matrix differential equation case:

$$\frac{d\mathbf{x}}{dt} = \dot{\mathbf{x}} = [A]\mathbf{x}, \quad \mathbf{x}(t_0) = \mathbf{x}_0 \quad (2.3)$$

where the coefficient matrix  $[A]$  is constant and  $\mathbf{x}(t)$  is an  $n$ -dimensional state vector. Schaub and Junkins show that, using a Taylor series solution, the  $\mathbf{x}(t)$  state vector may be computed in terms of the initial conditions as

$$\mathbf{x}(t) = \left( [I] + \sum_{n=1}^{\infty} A^n \frac{(t-t_0)^n}{n!} \right) \mathbf{x}(t_0) \quad (2.4)$$

The expression between the large parenthesis is exactly the definition of the matrix exponential function.[13] Therefore, the general solution for  $\mathbf{x}(t)$  may be written as

$$\mathbf{x}(t) = e^{[A](t-t_0)} \mathbf{x}(t_0) \quad (2.5)$$

Now consider a classical result that, if  $[A]$  has distinct eigenvalues, transforms the computation of the matrix exponential function into a trivial exercise. A transformation to a different  $n$ -dimensional state vector  $\boldsymbol{\eta}$  may be written as

$$\mathbf{x}(t) = [T]\boldsymbol{\eta}(t) \quad (2.6)$$

where  $[T]$  is a constant, non-singular  $n \times n$  matrix. Substituting Equation (2.6) into Equation (2.3) yields

$$\dot{\boldsymbol{\eta}} = ([T]^{-1}[A][T])\boldsymbol{\eta} \quad (2.7)$$

Schaub and Junkins show that the matrix multiplication of  $[T]^{-1}[A][T]$  is diagonal when the columns of the  $[T]$  matrix are the eigenvectors of  $[A]$ . [13] This state transformation converts the originally coupled set of  $n$  differential equations into  $n$  uncoupled differential equations, given by

$$\dot{\boldsymbol{\eta}}(t) = \lambda_i \boldsymbol{\eta}(t) \quad (2.8)$$

where each  $\lambda_i$  is an eigenvalue of  $[A]$ . Using the convenient choice of the matrix  $[T]$  allows for the computation of the matrix exponential function as follows:

$$e^{[A](t-t_0)} = [T][\text{diag}(e^{\lambda_i(t-t_0)})][T]^{-1} \quad (2.9)$$

where  $[\text{diag}(e^{\lambda_i(t-t_0)})]$  is a diagonal matrix with each diagonal entry given using the corresponding eigenvalue  $\lambda_i$ . The solution for the state transition matrix of the linear, homogeneous dynamic system is now applied to the specific case of the spring-mass system.

### 2.3.2 Spring-Mass System; Direct Analytical Solution

The equation of motion governing the standard spring-mass system is

$$m\ddot{x} + kx = 0 \quad (2.10)$$

where  $m$  denotes the mass and  $k$  is the spring constant. Various methods may be used to find the analytical solution for  $x(t)$  as

$$x(t) = x_0 \cos(\omega_n t) + \frac{\dot{x}_0}{\omega_n} \sin(\omega_n t) \quad (2.11)$$

where  $x_0$  and  $\dot{x}_0$  are the initial position and speed, respectively. Differentiating Equation (2.11) with respect to time yields

$$\dot{x}(t) = -\omega_n x_0 \sin(\omega_n t) + \dot{x}_0 \cos(\omega_n t) \quad (2.12)$$

where  $\omega_n = \sqrt{\frac{k}{m}}$  is the natural frequency of the spring-mass system. The values of  $x(t)$  and  $\dot{x}(t)$  may be combined into the state vector  $\mathbf{x}(t)$ , which is written in terms of the initial conditions as

$$\mathbf{x}(t) = \begin{pmatrix} x(t) \\ \dot{x}(t) \end{pmatrix} = \begin{bmatrix} \cos(\omega_n t) & \frac{\sin(\omega_n t)}{\omega_n} \\ -\omega_n \sin(\omega_n t) & \cos(\omega_n t) \end{bmatrix} \begin{pmatrix} x_0 \\ \dot{x}_0 \end{pmatrix} \quad (2.13)$$

Note that Equation (2.13) gives the state vector  $\mathbf{x}(t)$  in terms of the initial state vector  $\mathbf{x}_0(t)$  multiplied by a matrix. This matrix is the state transition matrix for the spring-mass system. Therefore, Equation (2.13) may be written equivalently as

$$\mathbf{x}(t) = [\Phi(t, t_0)] \mathbf{x}(t_0) \quad (2.14)$$

The previous process shows how, for some very simple systems, the state transition matrix may be derived by solving directly for the state vector  $\mathbf{x}(t)$  in terms of the initial conditions. However, not all systems lend themselves to this method of solution. Thus two more robust methods are used to solve for the state transition matrix of the spring-mass system. The solutions of the two following methods are compared with the previous solution for  $[\Phi(t, t_0)]$ .

### 2.3.3 Spring-Mass System; State Transformation Solution

The state transition matrix of the spring-mass system may also be determined by computing the eigenvalues and eigenvectors of the system's  $[A]$  coefficient matrix, as described earlier. In order to do so, the homogeneous vector-matrix differential equation for the spring-mass system is written as follows:

$$\dot{\mathbf{X}}(t) = \begin{pmatrix} \dot{x}(t) \\ \dot{\dot{x}}(t) \end{pmatrix} = \begin{bmatrix} 0 & 1 \\ -\omega_n^2 & 0 \end{bmatrix} \mathbf{X}(t) \equiv [A] \mathbf{X}(t), \quad \mathbf{X}(t_0) = \mathbf{X}_0 \quad (2.15)$$

If the  $[A]$  coefficient matrix is determined to have distinct eigenvalues, then the computation of the matrix exponential function for this system is trivial.

Before computing the eigenvalues of the spring-mass system, a brief review of the eigenvalue problem is given. This problem is stated mathematically as

$$[A]\mathbf{s} = \lambda\mathbf{s} \quad (2.16)$$

where each  $\lambda_i$  is an eigenvalue of the  $[A]$  matrix. Equation (2.16) may also be written as follows:

$$([A] - \lambda[I])\mathbf{s} = \mathbf{0} \quad (2.17)$$

If the matrix  $([A] - \lambda[I])$  is invertible, then the only solution is  $\mathbf{s} = \mathbf{0}$ . However, this trivial solution is not permissible for the eigenvalue problem. The matrix  $([A] - \lambda[I])$  must have no inverse, and therefore its determinant must be zero:

$$\det([A] - \lambda[I]) = 0 \quad (2.18)$$

Solving this characteristic equation for the spring-mass system yields two distinct eigenvalues, given as  $\lambda_{1,2} = i\omega_n, -i\omega_n$ . These eigenvalues are used to solve for the two corresponding eigenvectors of the  $[A]$  matrix. While the eigenvalues of the system are unique, the eigenvectors for a given  $[A]$  matrix are not unique. For instance, if  $\mathbf{x}$  is an eigenvector of  $[A]$ , then any constant non-zero multiple of  $\mathbf{x}$  is also an eigenvector of  $[A]$ .<sup>[6]</sup> The two eigenvectors of the standard spring-mass system are determined to be

$$\mathbf{s}_1 = \begin{pmatrix} 1 \\ i\omega_n \end{pmatrix}, \quad \mathbf{s}_2 = \begin{pmatrix} 1 \\ -i\omega_n \end{pmatrix} \quad (2.19)$$

As previously shown, because the  $[A]$  matrix for the spring-mass system has distinct eigenvalues, the matrix exponential function for the system may be computed as

$$e^{[A](t-t_0)} = [T][\text{diag}(e^{\lambda_i(t-t_0)})][T]^{-1} \quad (2.20)$$

where, in this case, the two columns of  $[T]$  are the eigenvectors  $\mathbf{s}_1$  and  $\mathbf{s}_2$ . Thus the state transition matrix for the spring-mass system is given by

$$[\Phi(t, t_0)] = e^{[A](t-t_0)} = \begin{bmatrix} 1 & 1 \\ i\omega_n & -i\omega_n \end{bmatrix} \begin{bmatrix} e^{i\omega_n(t-t_0)} & 0 \\ 0 & e^{-i\omega_n(t-t_0)} \end{bmatrix} \begin{bmatrix} 1 & 1 \\ i\omega_n & -i\omega_n \end{bmatrix}^{-1} \quad (2.21)$$

where the inverse  $[T]^{-1}$  is determined to be

$$[T]^{-1} = \begin{bmatrix} 1 & 1 \\ i\omega_n & -i\omega_n \end{bmatrix}^{-1} = \begin{bmatrix} \frac{1}{2} & \frac{1}{2i\omega_n} \\ \frac{1}{2} & \frac{-1}{2i\omega_n} \end{bmatrix} \quad (2.22)$$

The reduced state transition matrix for the spring-mass system is calculated as

$$[\Phi(t, t_0)] = \begin{bmatrix} \frac{1}{2}(e^{i\omega_n(t-t_0)} + e^{-i\omega_n(t-t_0)}) & \frac{1}{2i\omega_n}(e^{i\omega_n(t-t_0)} - e^{-i\omega_n(t-t_0)}) \\ \frac{i\omega_n}{2}(e^{i\omega_n(t-t_0)} - e^{-i\omega_n(t-t_0)}) & \frac{1}{2}(e^{i\omega_n(t-t_0)} + e^{-i\omega_n(t-t_0)}) \end{bmatrix} \quad (2.23)$$

Euler's equation may be used to transform the matrix entries of Equation (2.23) into sine and cosine format.<sup>[4]</sup> In this manner, the state transition matrix is written as

$$[\Phi(t, t_0)] = \begin{bmatrix} \cos(\omega_n(t-t_0)) & \frac{\sin(\omega_n(t-t_0))}{\omega_n} \\ -\omega_n \sin(\omega_n(t-t_0)) & \cos(\omega_n(t-t_0)) \end{bmatrix} \quad (2.24)$$

Note that the state transition matrix of Equation (2.24) matches the matrix of Equation (2.13) exactly. While this second method used to solve for  $[\Phi(t, t_0)]$  is more time-consuming, it can be applied to systems for which  $\dot{\mathbf{X}}(t)$  cannot be determined as a function of  $\mathbf{X}(t)$  directly.

### 2.3.4 Spring-Mass System; Matrix Exponential Solution

One additional way to solve for the state transition matrix of the spring-mass system is to use the definition of the matrix exponential function to solve for each entry in series format. The problem is given as follows:

$$e^{[A](t-t_0)} = \left( [I] + \sum_{n=1}^{\infty} A^n \frac{(t-t_0)^n}{n!} \right), \quad [A] = \begin{bmatrix} 0 & 1 \\ -\omega_n^2 & 0 \end{bmatrix} \quad (2.25)$$

Carrying out the series for the (1,1) entry of the state transition matrix yields

$$[\Phi(t, t_0)](1, 1) = 1 + 0 - \frac{(\omega_n(t-t_0))^2}{2!} + 0 + \frac{(\omega_n(t-t_0))^4}{4!} + \dots \quad (2.26)$$

The series representation of the cosine function is given as[14]

$$\cos(x) = 1 - \frac{x^2}{2!} + \frac{x^4}{4!} + \dots \quad (2.27)$$

Thus, by comparing Equations (2.26) and (2.27), it can be seen that, in the limit, the (1,1) entry of the state transition matrix may be written as

$$[\Phi(t, t_0)](1, 1) = \cos(\omega_n(t-t_0)) \quad (2.28)$$

which matches the (1,1) entries of the matrices given in Equations (2.13) and (2.24). In a similar fashion, the other three entries of  $[\Phi(t, t_0)]$  may be derived from their series representations. Their derivations using this method will also yield values that match the entries given in Equations (2.13) and (2.24). Computing the state transition matrix by carrying out the matrix exponential function serves as a good exercise in working with series representations of functions. It also supports the findings of the previous two methods used to solve for  $[\Phi(t, t_0)]$ .

### 2.3.5 Using State Transition Matrices to Apply Corrections to Initial Conditions

The state transition matrix provides a way to map perturbations in the initial state into changes in the final state. The mathematical representation of this mapping is repeated here:

$$\mathbf{x}(t) = [\Phi(t, t_0)]\mathbf{x}(t_0) \quad (2.29)$$

Note that the state transition matrix may be partitioned into smaller submatrices as follows:

$$[\Phi] = \begin{bmatrix} \Phi_{11} & \Phi_{12} \\ \Phi_{21} & \Phi_{22} \end{bmatrix} \quad (2.30)$$

Let the state vector  $\mathbf{x}$  be defined as

$$\mathbf{x} = \begin{pmatrix} \mathbf{r} \\ \dot{\mathbf{r}} \end{pmatrix} \quad (2.31)$$

where  $\dot{\mathbf{r}}$  is the inertial derivative of the position vector  $\mathbf{r}$ . Using these definitions of the state transition matrix and the state vector, Equation (2.29) may be rewritten as

$$\begin{pmatrix} \mathbf{r} \\ \dot{\mathbf{r}} \end{pmatrix} = \begin{bmatrix} \Phi_{11} & \Phi_{12} \\ \Phi_{21} & \Phi_{22} \end{bmatrix} \begin{pmatrix} \mathbf{r}_0 \\ \dot{\mathbf{r}}_0 \end{pmatrix} \quad (2.32)$$

where the initial state vector is composed of  $\mathbf{r}_0$  and  $\dot{\mathbf{r}}_0$ . Suppose that, for a particular system, a change in the position vector  $\mathbf{r}$  at time  $t$  is desired. This problem is applied to the restricted four-body orbit setup in Chapter 2.4. In order to change  $\mathbf{r}$ , perturbations in either  $\mathbf{r}_0$  or  $\dot{\mathbf{r}}_0$  may be used.

Suppose that changing the initial velocity vector is more suitable for the given system. The effect of perturbing the initial velocity  $\dot{\mathbf{r}}_0$  by some value  $\delta\dot{\mathbf{r}}_0$  on the final position  $\mathbf{r}$  is calculated using the state transition matrix as follows:

$$\delta\mathbf{r} = [\Phi_{12}]\delta\dot{\mathbf{r}}_0 \quad (2.33)$$

Each of the four submatrices that comprise the general state transition matrix may be used to relate changes in initial conditions to changes in the final state vector. The question of which submatrix to use depends upon the nature of the particular problem. If changes in initial position are more feasible than changes in initial velocity, then  $[\Phi_{11}]$  and  $[\Phi_{21}]$  are the two submatrices that should be considered for perturbations in the final state. Chapter 2.4 includes an examination of how to apply this sensitivity analysis to the restricted four-body problem.

## 2.4 Sensitivity Analysis of the Restricted Four-Body Problem

The previous analysis of state transition matrices offers an introduction to the concept of sensitivities. As is stated in Chapter 2.3, the state transition matrix is the sensitivity matrix of the current state with respect to the initial conditions. It maps perturbations in the initial conditions into changes in the final state at time  $t$ . This concept of relating changes in initial conditions to changes in the final state is now extended to the restricted four-body problem.

Chapter 2.4 uses a Hohmann transfer from Earth to Mars as the restricted four-body system. Reppert provides a detailed explanation of the Hohmann transfer orbit setup.[10] The orbits of both Earth and Mars are restricted to be circular. In addition, the only gravitational effects considered are the effects of the sun, Earth, and Mars on the spacecraft. All motion is constrained to be planar.

This chapter provides an analysis of how changes in the transfer orbit's initial conditions affect certain parameters of the Martian arrival orbit. These sensitivities of the Hohmann transfer are calculated both analytically and numerically. The calculations of the sensitivities provide an efficient means of estimating the initial conditions required to achieve a desired arrival orbit geometry.

### 2.4.1 Analytical Solution for $\frac{\partial d_a}{\partial \nu_0}$

This section presents the development of an analytical approximation to the sensitivity of the arrival miss distance  $d_a$  with respect to the initial Earth-relative speed  $\nu_0$ . In other words, perturbations in the velocity  $\nu_0$  are mapped into changes in the miss distance  $d_a$ . The process for deriving the  $\frac{\partial d_a}{\partial \nu_0}$  sensitivity is very methodical. A series of partial derivatives are used to work backward from the miss distance to the initial Earth-relative speed. Then the chain rule for differentiation is used to relate each of the separate partial derivatives. The partial derivatives used to calculate the sensitivity analytically are derived from patched-conic equations. Therefore, the analytical solution for the sensitivity  $\frac{\partial d_a}{\partial \nu_0}$  derived in this section is an approximation to the true non-Keplerian sensitivity. Nonetheless, as is later shown, the approximate sensitivity provides a sufficient means of calculating the necessary initial conditions for a desired arrival orbit.

#### Derivation of the Analytical Solution

The first required partial derivative is that of the miss distance  $d_a$  with respect to the Hohmann semi-major axis  $a_H$ . For the Hohmann transfer from Earth to Mars, the chord  $c$  may be approximated as

$$c \approx 2a_H - d_a \quad (2.34)$$

assuming that the spacecraft's Mars-relative arrival velocity  $\boldsymbol{\nu}_2$  is parallel to Mars' velocity vector  $\boldsymbol{v}_\sigma$ . Figure 2.2 provides an illustration of the required arrival orbit geometry. Note how the miss distance  $d_a$  is treated as a signed scalar. For the Hohmann transfer from Earth to Mars, the arrival velocity  $\boldsymbol{\nu}_2$  is always nearly parallel to  $\boldsymbol{v}_\sigma$ . Thus Equation (2.34) presents a good approximation for the problem being studied. Using Equation (2.34), the partial of the miss distance with respect to the semi-major axis is calculated as follows:

$$\frac{\partial d_a}{\partial a_H} = \left( \frac{\partial c}{\partial d_a} \right)^{-1} \left( \frac{\partial c}{\partial a_H} \right) = (-1)^{-1}(2) = -2 \quad (2.35)$$

Thus if  $a_H$  is perturbed by some value  $n$ , then the corresponding change in  $d_a$  is predicted to be  $-2n$ .

The next partial derivative to be computed is that of the semi-major axis  $a_H$  with respect to the heliocentric departure velocity  $v_1$ . Figure 2.3 offers an illustration of the hyperbolic departure orbit. By applying the energy equation at the time  $t_1$  (when the spacecraft reaches Earth's sphere of influence), the semi-major axis is related to  $v_1$  as

$$a_H = \frac{r_\oplus \mu_\odot}{2\mu_\odot - r_\oplus v_1^2} \quad (2.36)$$

where  $r_\oplus$  is the mean orbit radius of Earth and  $\mu_\odot$  is the gravitational coefficient of the sun. By Equation (2.36), the partial of  $a_H$  with respect to  $v_1$  is determined to be

$$\frac{\partial a_H}{\partial v_1} = \frac{2r_\oplus^2 v_1 \mu_\odot}{(2\mu_\odot - r_\oplus v_1^2)^2} \quad (2.37)$$

Continuing to work back to the initial Earth-relative velocity  $\nu_0$ , the next required partial derivative is that of the heliocentric  $v_1$  with respect to the Earth-relative  $\nu_1$ . Both of these

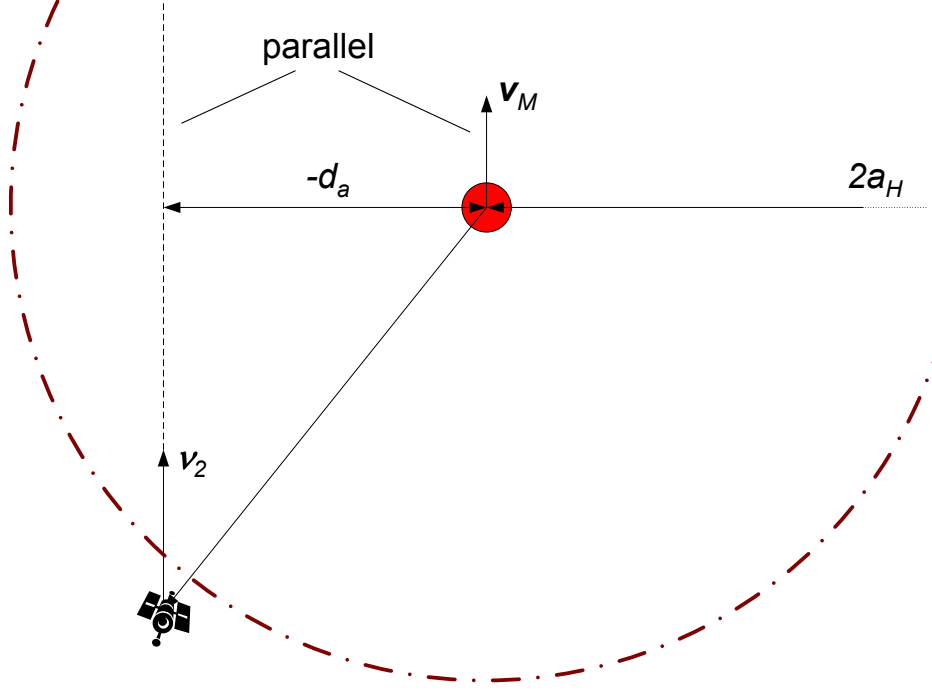


Figure 2.2: **Geometry Used to Approximate the Hohmann Chord Length.** Example of an arrival orbit velocity  $v_2$  necessary for the approximation of the Hohmann chord length.

velocities are displayed in Figure 2.3. In order to attain a relation between  $v_1$  and  $\nu_1$ , it is assumed that  $\nu_s$  converges parallel to  $\nu_\oplus$  at time  $t_1$ . Making this assumption, it follows that

$$v_1 = \nu_1 + v_\oplus \quad (2.38)$$

Thus the partial derivative  $\partial v_1 / \partial \nu_1$  is equal to one.

Finally, the partial derivative of  $v_1$  with respect to the initial Earth-relative speed  $\nu_0$  is computed. In order to do so, the energy equation is applied at time  $t_0$ . In addition, it is assumed that  $r_1 \approx \infty$ . [10] By applying the energy equation,  $\nu_1$  is expressed as a function of  $\nu_0$  as follows:

$$\nu_1 = \sqrt{\nu_0^2 - \frac{2\mu_\oplus}{r_0}} \quad (2.39)$$

where  $r_0$  is the initial parking radius of the hyperbolic departure. By Equation (2.39), the partial of  $\nu_1$  with respect to  $\nu_0$  is expressed as

$$\frac{\partial \nu_1}{\partial \nu_0} = \frac{\nu_0}{\sqrt{\nu_0^2 - \frac{2\mu_\oplus}{r_0}}} \quad (2.40)$$

In order to determine the partial of the miss distance  $d_a$  with respect to  $\nu_0$ , the four previously calculated partial derivatives are related using the chain rule for differentiation.

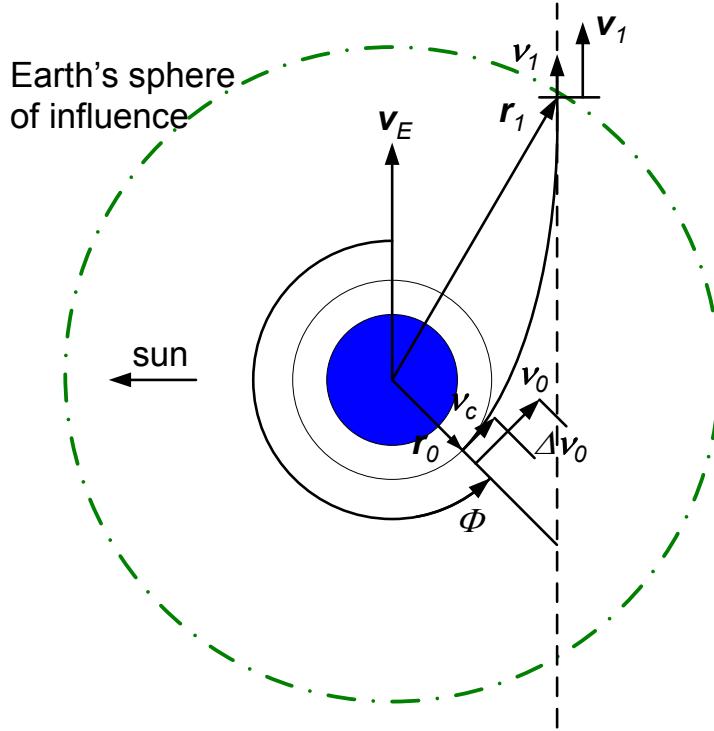


Figure 2.3: **Parameters of the Hyperbolic Departure Orbit.** Depiction of the position and velocity notation used to describe the spacecraft's hyperbolic departure orbit from Earth.

The process is given as follows:

$$\frac{\partial d_a}{\partial \nu_0} = \frac{\partial d_a}{\partial a_H} \frac{\partial a_H}{\partial v_1} \frac{\partial v_1}{\partial \nu_1} \frac{\partial \nu_1}{\partial \nu_0} = \frac{-4r_{\oplus}^2 v_1 \nu_0 \mu_{\odot}}{(2\mu_{\odot} - r_{\oplus} v_1^2)^2 \sqrt{\nu_0^2 - \frac{2\mu_{\oplus}}{r_0}}} \quad (2.41)$$

Equation (2.41) gives the analytical solution for the sensitivity of the miss distance  $d_a$  with respect to the initial Earth-relative velocity  $\nu_0$ . This sensitivity may be used to relate perturbations in  $\nu_0$  to predicted changes in  $d_a$ .

### Application Using the Four-Body Integrator

The analytical approximation to  $\partial d_a / \partial \nu_0$  is now applied to the four-body problem using the previously developed variable step Runge-Kutta integrator.[11] Let the desired miss distance  $d^*$  correspond to a desired arrival periapsis of 4000 km. Using the patched-conic approximation, some initial guess for the required velocity  $\nu_0$  is computed. Reppert previously showed that this initial guess yields an arrival orbit that penetrates Mars' sphere of influence. The current goal is to use the analytical solution for  $\partial d_a / \partial \nu_0$  to refine  $\nu_0$  such that it produces the desired miss distance  $d^*$ . Let the miss distance error at a given iteration be defined as

$$d_e = d_a - d^* \quad (2.42)$$

Table 2.1: **Error Values Using Analytical  $\partial d_a/\partial \nu_0$ .** Listing of the miss distance values calculated for each step of the correction scheme using an analytical  $\partial d_a/\partial \nu_0$ . Note that the iterative process stops after the miss distance error  $|d_e|$  drops below 10 km.

Iteration	$d_a$ , km	$d^*$ , km	$d_e$ , km
1	-4.09307e+005	-8.05187e+003	-4.01255e+005
2	-9.27212e+004	-8.05187e+003	-8.46693e+004
3	-1.97402e+004	-8.05187e+003	-1.16883e+004
4	-9.49203e+003	-8.05187e+003	-1.44016e+003
5	-8.22640e+003	-8.05187e+003	-1.74537e+002
6	-8.07298e+003	-8.05187e+003	-2.11189e+001
7	-8.05443e+003	-8.05187e+003	-2.56708e+000

where  $d_a$  is the actual miss distance computed using the four-body integrator. By Equation (2.42), after a given iteration, the applied change in miss distance should be  $\Delta d_a = -d_e$ . Using the applied change in  $d_a$ , the required perturbation in  $\nu_0$  is computed as follows:

$$\Delta \nu_0 = \left( \frac{\partial d_a}{\partial \nu_0} \right)^{-1} \Delta d_a = - \left( \frac{\partial d_a}{\partial \nu_0} \right)^{-1} d_e = \frac{(2\mu_\odot - r_\oplus v_1^2)^2 \sqrt{\nu_0^2 - \frac{2\mu_\oplus}{r_0}}}{4r_\oplus^2 v_1 \nu_0 \mu_\odot} d_e \quad (2.43)$$

Equation (2.43) is used to make corrections in the initial Earth-relative velocity  $\nu_0$  for each iteration of the Hohmann transfer. The desired result is an arrival orbit that has a miss distance  $d_a$  corresponding to a periapsis radius  $r_3$  of 4000 km. Because  $d_a$  is a signed scalar, this application can be used to generate both posigrade and retrograde arrival orbits. If the arrival orbit direction were not significant, then the desired miss distance  $d^*$  could be assigned the same sign as  $d_a$ . This process would yield the desired arrival geometry closest to the initial integrated orbit.

The code used to apply the  $\nu_0$  correction scheme to the restricted four-body problem is developed in C. The reasons for programming the iterative process in C are given in Chapter 2.2. On the first iteration of the correction loop, the patched-conic approximation for the  $\nu_0$  required to arrive at Mars is calculated. This value is used as the first guess for the required departure speed. The first iteration also includes a calculation of the desired miss distance  $d^*$  based upon the specified Mars arrival periapsis  $r_3$  (4000 km). Thereafter, for each iteration, the value of  $\nu_0$  is corrected using the approximate sensitivity given in Equation (2.43). The corrections are performed until the difference between the actual miss distance  $d_a$  and the desired miss distance  $d^*$  is less than 10 km. A limit of 15 iterations is placed on the correction scheme to avoid excessive computation. Figure 2.4 provides a flowchart outlining the iterative process that uses the analytical approximation for  $\partial d_a/\partial \nu_0$  to apply corrections to  $\nu_0$ .

Using the analytical approximation to the miss distance sensitivity, the system does indeed converge. As shown by Table 2.1, the miss distance  $d_a$  converges to within 10 km of the desired miss distance  $d^*$  after seven iterations. It is important to note that the value of  $d^*$  never changes throughout the iterative process. The desired periapsis radius  $r_3$  and the overall Hohmann orbit geometry are the two main factors that affect the computation of  $d^*$ . Because the patched-conic approximation is used to derive a relation for  $d^*$ , the

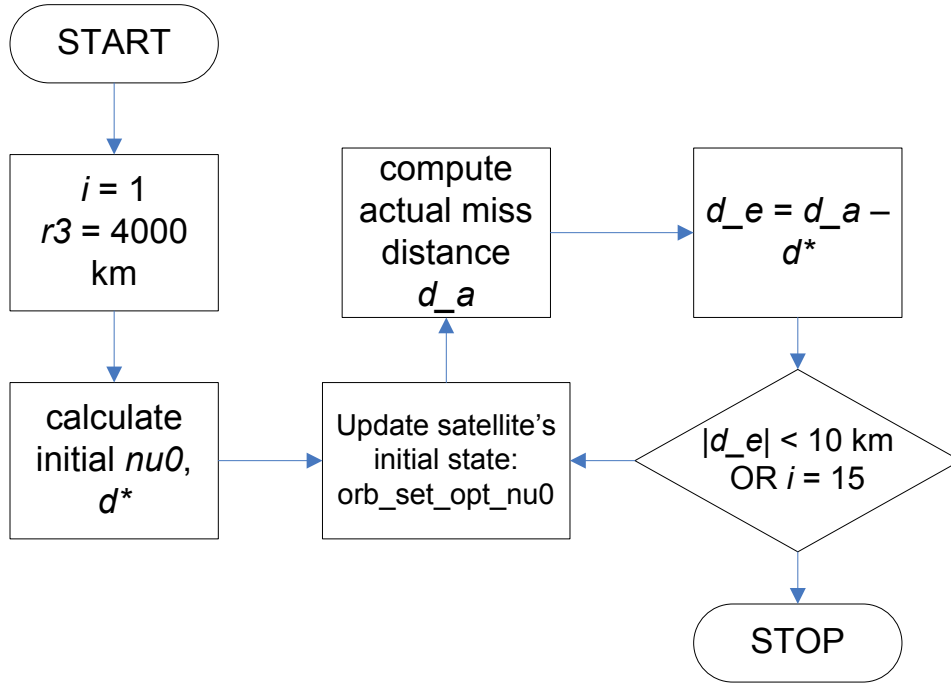


Figure 2.4: **Correction Scheme Using Analytical  $\partial d_a/\partial \nu_0$ .** Flowchart describing the iterative process used to apply the analytical approximation for  $\partial d_a/\partial \nu_0$  to the restricted four-body problem. The sensitivity is used to make corrections in the initial speed  $\nu_0$ .

initial departure speed  $\nu_0$  is taken to have no effect on the desired miss distance. However, the value of  $\nu_0$  is taken to have an effect on the departure angle  $\Phi$  (Figure 2.3). For each correction in  $\nu_0$ , patched-conic relations are used to compute a corresponding perturbation in the departure angle. If this angle were not corrected along with the departure speed, then the spacecraft would not exit Earth’s sphere of influence at the desired hyperbolic trajectory. In this case, controlled adjustments to  $\nu_0$  could not be made, and the iterative process would most likely fail to determine the necessary departure velocity.

Another notable feature of the data given in Table 2.1 is that both the actual and error miss distances  $d_a$  and  $d_e$  are always negative. The spacecraft always penetrates Mars’ sphere of influence on the negative side of the Mars-relative coordinate frame, as is later shown in Figure 2.6. In other words, the analytical approximation to the sensitivity never yields a correction that overshoots the desired miss distance. Each corrected value of  $\nu_0$  consistently approaches the desired arrival geometry from the same side.

As both Table 2.5 and Figure 2.5 show, the magnitude of the miss distance error  $d_e$  decreases by approximately one order of magnitude for every iteration. From the first iteration to the seventh iteration, the magnitude drops from  $4.01 \times 10^5$  km to 2.57 km. After the seventh iteration, the 10-km error stopping criterion is achieved, and the iterative process is terminated.

In summary, the analytical approximation to the miss distance sensitivity performs very well when used to correct  $\nu_0$  for the given Hohmann transfer orbit. The actual miss distance consistently approaches the desired miss distance, with the miss distance error decreasing

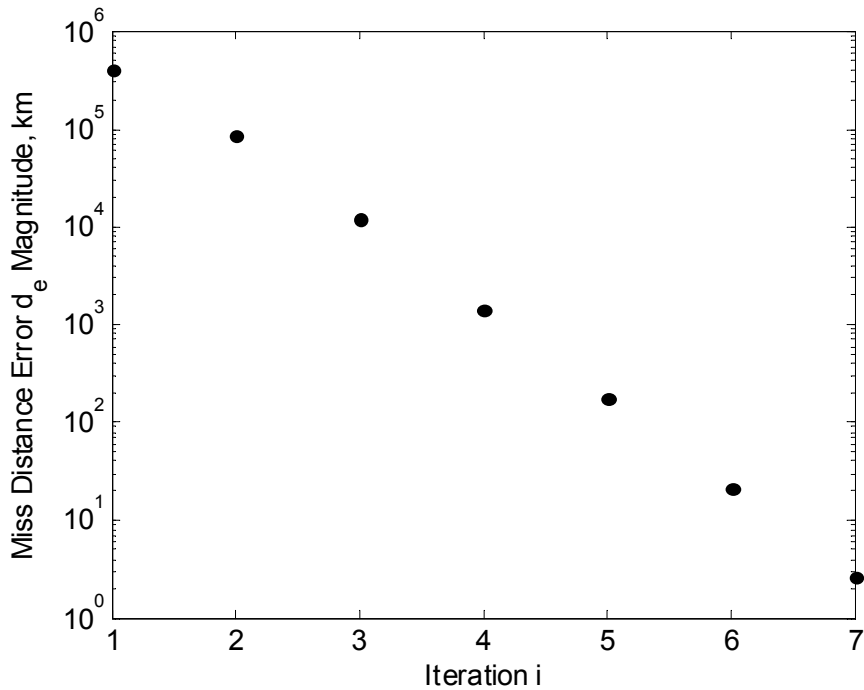


Figure 2.5: **Error Values Using Analytical  $\partial d_a/\partial \nu_0$ .** Plot of the decreasing miss distance error values  $d_e$  for the  $\nu_0$  correction scheme using an analytical sensitivity approximation. Note that  $d_e$  decreases by approximately one order of magnitude at every iteration.

by an order of magnitude at each step. Using this correction scheme, it is determined that an initial speed  $\nu_0$  of approximately 10.71824 km/s is necessary to achieve the desired miss distance. Figure 2.6 displays the corrected Mars arrival orbit geometry. As Figure 2.6 shows, the arrival orbit achieves a periapsis radius  $r_3$  that is very close to 4000 km. However, the correction scheme presented in this section is only used to compute corrections in the miss distance  $d_a$ . Patched-conic relations are then used to relate the miss distance to the final periapsis radius  $r_3$ . A more exact correction process would incorporate the gravitational influences of Earth and the sun into the calculated of the actual periapsis radius  $r_3$ . In this manner, corrections could be made directly to the arrival periapsis  $r_3$ . Nonetheless, Figure 2.6 illustrates that the analytical approximation to  $\partial d_a/\partial \nu_0$  provides a sufficient means of achieving a good estimate of the necessary departure speed  $\nu_0$ .

### 2.4.2 Numerical Solution for $\frac{\partial d_a}{\partial \nu_0}$

The numerical miss distance correction scheme uses approximations to the  $\frac{\partial d_a}{\partial \nu_0}$  sensitivity. At each iteration, a current value of  $\nu_0$  is used to integrate the spacecraft's Hohmann transfer to Mars. The resulting miss distance  $d_a$  upon entering Mars' sphere of influence is recorded. The current  $\nu_0$  is then perturbed by a value  $\epsilon$  as follows:

$$\nu'_0 = \nu_0 + \epsilon \quad (2.44)$$

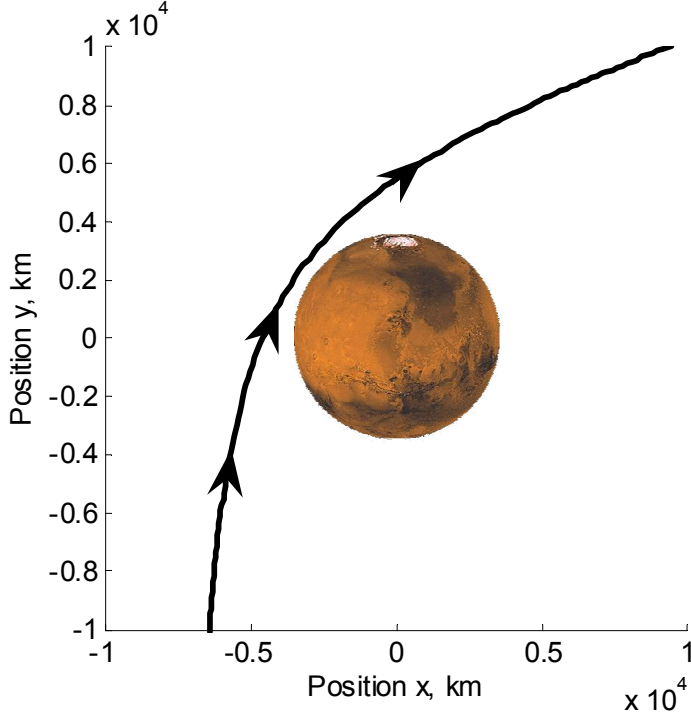


Figure 2.6: **Final Mars-Relative Arrival Orbit Geometry Using Analytical  $\partial d_a/\partial \nu_0$ .** Depiction of the Mars-relative orbit geometry that results from using the analytical approximation to the miss distance sensitivity  $\partial d_a/\partial \nu_0$ . Positions  $x$  and  $y$  are given relative to the center of the Mars frame  $\mathcal{M}$ .

where  $\nu'_0$  is the Earth-centric departure speed after the small perturbation. The importance of choosing a decent  $\epsilon$  value is discussed later in this section. Once the perturbed speed  $\nu'_0$  is obtained, the spacecraft's Hohmann transfer is integrated again. This second orbit is slightly different from the first, resulting in a different miss distance  $d'_a$ . The sensitivity  $\frac{\partial d_a}{\partial \nu_0}$  can then be approximated as:

$$\frac{\partial d_a}{\partial \nu_0} \approx \frac{d'_a - d_a}{\nu'_0 - \nu_0} = \frac{d'_a - d_a}{\epsilon} \quad (2.45)$$

This approximate sensitivity is used to compute a new Earth-centric departure speed as follows:

$$\nu_{0_{i+1}} = \nu_{0_i} - \left( \frac{\partial d_a}{\partial \nu_0} \right)^{-1} d_e \quad (2.46)$$

where  $d_e$  represents the error in the miss distance at the current iteration  $i$ .

In this manner, an approximate sensitivity is computed for each iteration of the correction scheme, and therefore two complete integrations of the Hohmann transfer are necessary for one iteration  $i$ . Each iteration of the numerical sensitivity correction scheme takes approximately twice as long as an iteration using the analytical sensitivity. However, this property does not necessarily mean that the numerical solution takes longer to converge to a desired miss distance criterion. A comparison of integration time using the two methods is provided in Section 2.4.4.

Table 2.2: **Effects of Perturbation Value  $\epsilon$  Using Numerical  $\frac{\partial d_a}{\partial \nu_0}$** . Tabulated values for number of iterations  $k$  and final miss distance error magnitude  $|d_e|$  versus perturbation  $\epsilon$  using the numerical  $\frac{\partial d_a}{\partial \nu_0}$ . At  $\epsilon$  equal to 1e-02 and 1e-10, the iterations do not converge (DNC).

$\epsilon$ , km/s	1e-02	1e-03	1e-04	1e-05	1e-06	1e-07	1e-08	1e-09	1e-10
$k$	DNC	5	4	4	4	4	4	5	DNC
$ d_e $ , km	DNC	4.16e-1	8.16e-1	7.29e-2	4.85e-2	1.98e-1	6.43e-1	1.09e-1	DNC

At this point, it is important to note that a good initial guess for the necessary departure speed  $\nu_0$  is required due to the nonlinearity of the spacecraft's motion. If the initial guess is not within a sufficient range of the required value, the numerical correction scheme fails. For this problem, the patched-conic approximation to the necessary  $\nu_0$  for the transfer is sufficient for convergence to a solution. When solving linear systems of equations, the initial guess is not very important when considering convergence. But for nonlinear problems such as the restricted four-body setup, the initial guess must be chosen with care.[9]

Table 2.2 provides a listing of the number of iterations  $k$  and final miss distance error values  $|d_e|$  corresponding to the use of a range of perturbation values  $\epsilon$ . The value of  $\epsilon$  has a significant effect on the rate of convergence of the numerical correction scheme. For instance, any values of  $\epsilon$  greater than or equal to  $10^{-2}$  km/s are too large to yield convergence. Such large perturbations incur excessively large corrections to the Hohmann transfer. Conversely, any values of  $\epsilon$  equal to or smaller than  $10^{-10}$  km/s are too small to yield convergence. Using a 32-bit processor, the truncation error involved with such calculations makes the correction scheme ineffective. Using a numerical approximation to  $\frac{\partial d_a}{\partial \nu_0}$ , the number of iterations necessary for convergence to the stopping criterion ( $d_e < 10$  km) plateaus at four for  $\epsilon$  between  $10^{-4}$  km/s and  $10^{-8}$  km/s.

Figure 2.7 provides a plot of the number of iterations  $k$  necessary to satisfy the stopping criterion using the different values of  $\epsilon$ . As is noted in the figure, the minimum final miss distance error magnitude occurs at  $\epsilon = 10^{-6}$  km/s. However, all values of  $\epsilon$  between  $10^{-4}$  km/s and  $10^{-8}$  km/s provide convergence within the same minimum amount of time for the given stopping criterion.

### 2.4.3 Numerical Solution for $\frac{\partial r_3}{\partial \nu_0}$

The numerical periapsis correction scheme uses approximations to the  $\frac{\partial r_3}{\partial \nu_0}$  sensitivity. The algorithm for using the sensitivity approximation to apply corrections to the Earth-relative departure speed  $\nu_0$  is identical to that used for the miss distance numerical scheme. The only difference in this case is that the sensitivity is being used to correct the periapsis radius  $r_3$  instead of the miss distance  $d_a$ . Thus, after  $\nu_0$  is perturbed by some value  $\epsilon$ , the resulting orbit yields a periapsis radius  $r'_3$ . This perturbed periapsis radius is used with the unperturbed value to approximate the sensitivity as:

$$\frac{\partial r_3}{\partial \nu_0} \approx \frac{r'_3 - r_3}{\nu'_0 - \nu_0} = \frac{r'_3 - r_3}{\epsilon} \quad (2.47)$$

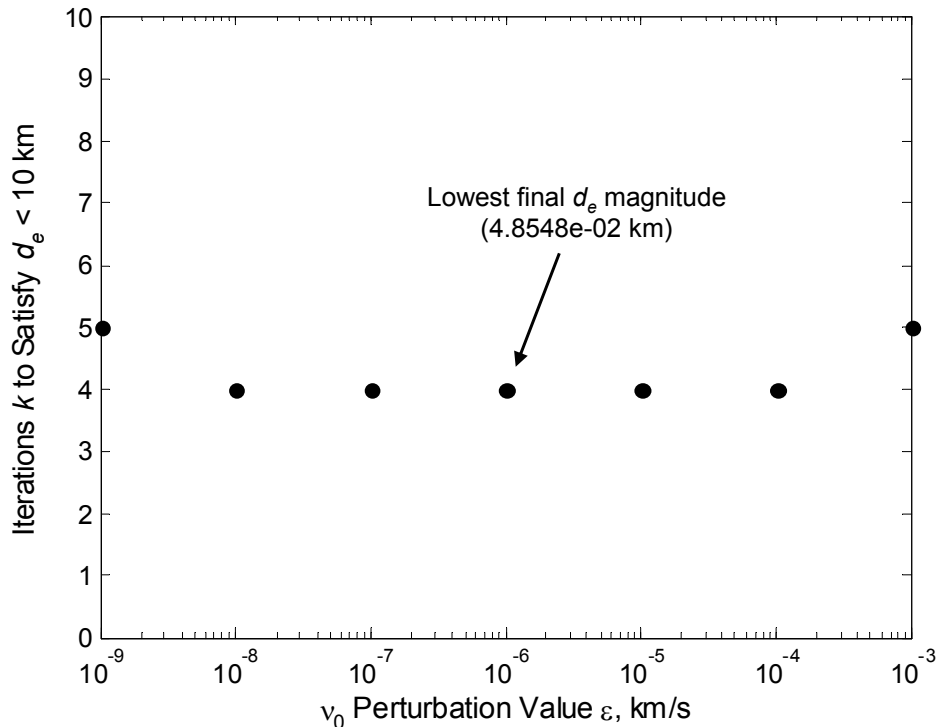


Figure 2.7: **Effect of  $\epsilon$  on Number of Iterations Using Numerical  $\frac{\partial d_e}{\partial \nu_0}$ .** Plot of the number of iterations  $k$  versus the  $\epsilon$  perturbation value in  $\nu_0$ . Note that  $\epsilon = 10^{-6}$  km/s yields the lowest final miss distance error magnitude.

The approximation to the sensitivity can then be used to apply corrections to  $\nu_0$  according to:

$$\nu_{0_{i+1}} = \nu_{0_i} - \left( \frac{\partial r_3}{\partial \nu_0} \right)^{-1} r_{3_e} \quad (2.48)$$

where  $r_{3_e}$  corresponds to the error of the current periapsis radius relative to the desired value (4000 km for this report). The value of  $\nu_0$  is corrected until the specified periapsis error tolerance is achieved.

The direct periapsis correction scheme is an even more sensitive nonlinear problem than the miss distance correction scheme. Therefore, the initial guess for  $\nu_0$  is more important for the periapsis correction algorithm. For the restricted four-body problem, using the patched-conic approximation to the necessary departure speed  $\nu_0$  is sufficient to provide convergence for a range of perturbations  $\epsilon$ . If the patched-conic approximation were not sufficiently accurate for an initial guess, the solution of the miss distance correction scheme could have been used as an initial guess for the periapsis scheme. It is important to note how a very sensitive, nonlinear problem can be brought to a particular solution by gradually increasing the complexity and robustness of the integration.

Figure 2.8 provides a plot of the number of iterations  $k$  taken to converge within the specified periapsis tolerance ( $r_{3_e} < 10$  km) for different values of perturbation  $\epsilon$ . Similar to

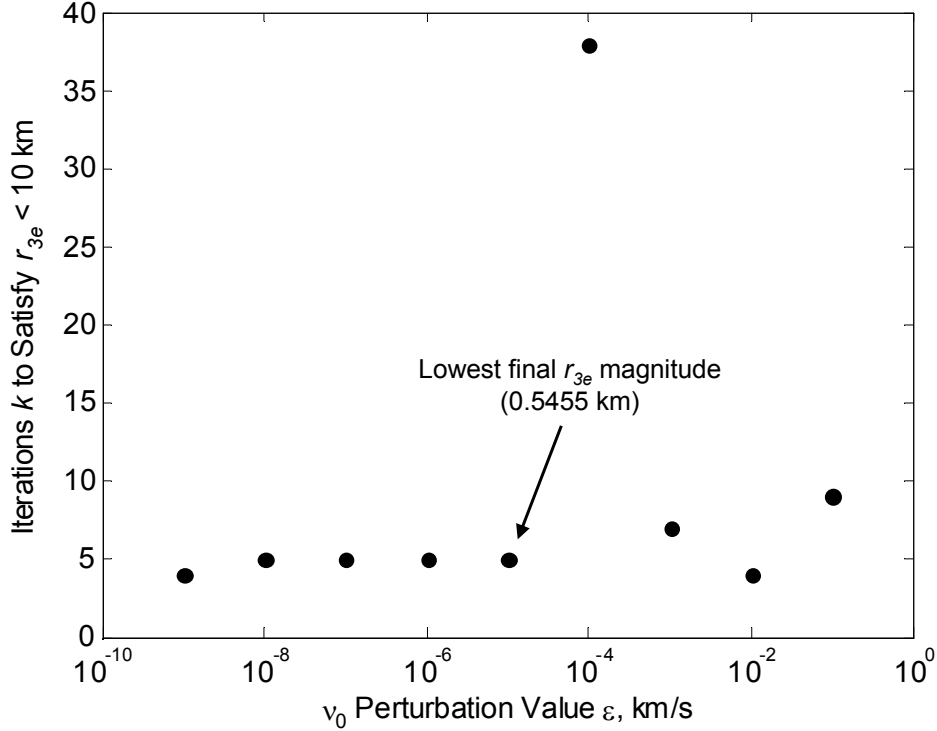


Figure 2.8: **Effect of  $\epsilon$  on Number of Iterations Using Numerical  $\frac{\partial r_3}{\partial \nu_0}$ .** Plot of the number of iterations  $k$  versus the  $\epsilon$  perturbation value in  $\nu_0$ . Note that  $\epsilon = 10^{-5}$  km/s yields the lowest final miss distance error magnitude.

the miss distance correction case, any values of  $\epsilon$  less than or equal to  $10^{-10}$  km/s result in correction schemes that do not converge. The lack of convergence is again due to the significant truncation error that occurs when using such fine perturbations to make corrections in  $\nu_0$ . If a 64-bit processor were used to make the calculations, then the lower limit for  $\epsilon$  values would most likely decrease due to the enhanced ability to handle computations with smaller numbers. All values of  $\epsilon$  equal to or greater than 1 km/s cause divergence as well. In this case, the corrections to  $\nu_0$  are so large that they cause excessive overshooting of the desired departure speed.

As Figure 2.8 shows, the number of iterations  $k$  plateaus for values of  $\epsilon$  between  $10^{-9}$  km/s and  $10^{-5}$  km/s. Interestingly, the periapsis correction scheme takes 38 iterations to converge for  $\epsilon = 10^{-4}$  km/s. For some reason, this seemingly standard value of  $\epsilon$  results in extremely slow convergence to the desired orbit geometry. The particular reasons for this behavior are left for a subsequent study. The minimum error magnitude  $|r_{3e}|$  (0.5455 km) occurs for a perturbation value of  $10^{-5}$  km/s. However, using perturbations of  $10^{-9}$  km/s and  $10^{-4}$  km/s result in the fastest rates of convergence, as the correction schemes finish within 4 iterations.

## 2.4.4 Integration Time Comparison

The number of iterations is not the best means of comparing the convergence rates of the three previously discussed correction algorithms. Both of the numerical sensitivity algorithms require two complete transfer orbit integrations for each iteration. The first integration is used to compute the current sensitivity value, and the second integration provides a means of calculating a new departure speed. In contrast, the analytical miss distance sensitivity algorithm requires only one integration per iteration. While the use of the analytical sensitivity requires more iterations to achieve a particular miss distance accuracy, it does not necessarily require more computational time.

Therefore, the central processor unit (CPU) time required to converge to within a particular accuracy is a better measure of the rate of convergence for the correction methods. The C function `clock` is used to provide an estimate of the amount of time that each of the three previously described methods takes to achieve the stopping criterion. The accuracy of the time estimates is 0.001 seconds. For both of the miss distance algorithms, the stopping criterion is set to  $d_e \leq 10^{-3}$  km, whereas that of the direct periapsis algorithm is set to  $r_{3_e} \leq 10^{-3}$  km. For each of the numerical approximation methods, the perturbation  $\epsilon$  is set to  $10^{-6}$  km/s.

Figure 2.9 provides plots of the time taken to provide different levels of accuracy in the arrival periapsis  $r_3$ . One of the most notable features of Figure 2.9 is the plateau in periapsis error  $r_{3_e}$  that occurs for both of the miss distance sensitivity algorithms. This plateau suggests that the two methods are unable to achieve an error in the periapsis radius less than approximately 190 km. The reason for the two methods' plateau is the approximation built into the patched-conic relation between the miss distance  $d_a$  and periapsis  $r_3$ . The patched-conic relation between  $d_a$  and  $r_3$  is built upon the two-body assumption. However, the sun and the Earth still have minor effects upon the trajectory of the spacecraft after it penetrates Mars' sphere of influence. In this manner, the patched-conic prediction for the miss distance necessary to achieve  $r_3 = 4000$  km involves approximately 190-km error from the actual periapsis radius.

In contrast, the algorithm using the numerical approximation to the periapsis sensitivity continues to approach zero error after a computational time of approximately 12 seconds. This third algorithm achieves periapsis errors roughly five orders of magnitude smaller by 24 seconds. In other words, the  $\frac{\partial r_3}{\partial \nu_0}$  correction algorithm achieves roughly meter-level periapsis accuracy by 24 seconds. The other two algorithms simply cannot achieve this accuracy. While all three methods perform fairly equally during the first 12 seconds of CPU time, the direct periapsis correction scheme performs much better when continuing the correction process. The reason for this better performance is that it does not depend upon a patched-conic relation between  $d_a$  and  $r_3$  for a specified accuracy. Thus, of the three examined methods, the  $\frac{\partial r_3}{\partial \nu_0}$  correction algorithm provides the best performance for correcting the arrival periapsis  $r_3$ .

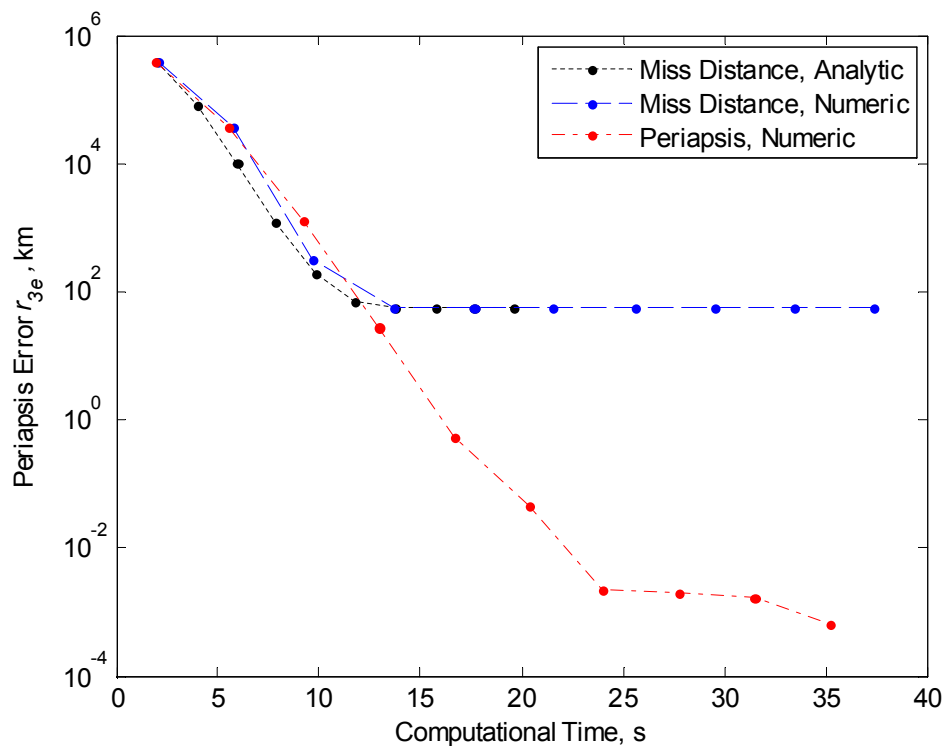


Figure 2.9: **Plot of Integration Times.** Plot of the integration time used for the analytical and numerical  $\frac{\partial d_a}{\partial \nu_0}$  approximation algorithms, as well as the numerical  $\frac{\partial r_3}{\partial \nu_0}$  algorithm. For each of the numerical approximation methods, the perturbation  $\epsilon$  is set to  $10^{-6}$  km/s.

## 2.5 Conclusions

This chapter presents an investigation of the use of sensitivities to optimize the arrival trajectory of a Hohmann transfer from Earth to Mars. The equations of motion are derived from a restricted four-body setup, with Earth, Mars, and the sun as the primary celestial bodies. Section 2.3 presents an introduction to the concept of sensitivities and, in particular, state transition matrices. The usefulness of sensitivity matrices in providing a description of how perturbations of one variable cause changes in another variable are discussed. The theory presented in Section 2.3 is then extended to perform optimizations of the restricted four-body problem. Section 2.4 discusses the use of three sensitivities to optimize the arrival orbit geometry of the Hohmann transfer: analytical  $\frac{\partial d_a}{\partial \nu_0}$ , numerical  $\frac{\partial d_a}{\partial \nu_0}$ , and numerical  $\frac{\partial r_3}{\partial \nu_0}$ . The application of each sensitivity to a corresponding orbit correction scheme is presented. Additionally, the convergence performances of the perturbation methods are compared by the computation time required to achieve a particular accuracy. The following conclusions are drawn:

1. The C programming language is more efficient than Matlab for calculating multiple transfer orbits in a computationally intense optimization problem.

2. Matlab provides user-friendly techniques for creating visualizations of the C output.
3. Sensitivity matrices provide a way to map perturbations in one variable into changes in another variable.
4. State transition matrices, a subset of sensitivity matrices, provide a way to map perturbations in initial conditions to changes in the final state.
5. For a stopping criterion of  $d_e \leq 10$  km, the use of the analytical sensitivity  $\frac{\partial d_a}{\partial \nu_0}$  provides convergence within seven iterations.
6. For a stopping criterion of  $d_e \leq 10$  km, the use of the numerical sensitivity  $\frac{\partial d_a}{\partial \nu_0}$  provides convergence within four iterations for a series of departure speed perturbations  $\epsilon$ .
7. For a stopping criterion of  $r_3 \leq 10$  km, the use of the numerical sensitivity  $\frac{\partial r_3}{\partial \nu_0}$  provides convergence within four iterations for two values of departure speed perturbation  $\epsilon$ .
8. During the first 12 seconds of computational time, the three perturbation techniques perform equally well.
9. After 12 seconds, the direct  $r_3$  correction scheme performs much better than the indirect  $d_a$  correction schemes.
10. The  $r_3$  correction scheme performs better because it does not depend on the patched-conic approximation to the relation between the miss distance and the periapsis radius.

# Chapter 3

## Application of Continuation Methods to the Restricted Four-Body Problem

### 3.1 Introduction

Chapter 2 presents the use of sensitivities as a tool for modeling interplanetary transfer orbits. For a particular two-point boundary value problem, sensitivities may be used to adjust initial conditions in order to achieve a desired final state. However, it is important to note that sensitivities can only be used to optimize one two-point boundary value problem; they cannot be used to solve a series of problems.

Thus, consider the following question: What if the solution to a series of similar boundary value problems is desired? In this case, a sensitivity application is not sufficient to provide the required family of answers. In Chapter 2, sensitivities are used to find the initial state vector required of a spacecraft in order to transfer from Earth to Mars and achieve a desired final periapsis radius  $r_3$ . Suppose that similar initial state vector solutions are required for transfer orbits with successively smaller times of flight. This more general problem requests the solution to a series of similar two-point boundary value problems, each with slight differences in one parameter: time of flight.

Such a general type of problem is very applicable to present-day transfer orbit modeling and analysis. For any particular interplanetary transfer mission, information regarding families of similar transfer possibilities are required in order to compare and choose the optimum transfer geometry. The series of  $\Delta\mathbf{v}$  estimates received from such an analysis can be used with other mission design factors in order to select a particular mission geometry.

Chapter 3 presents one method that, when used in combination with sensitivity correction schemes, may be used to solve such families of boundary value problems. This method, known either as the homotopy or the continuation method, represents a very powerful tool for modeling general interplanetary transfer orbit problems. The chapter begins with an introduction to the theory behind continuation methods, followed by an application of such methods to an example problem presented by Roberts and Shipman.[12] It is important to note that this chapter involves multi-dimensional sensitivity correction schemes, as opposed to the scalar corrections made to the four-body problem in Chapter 2. The example problem analysis provides a detailed first look into how the continuation method incorporates

sensitivity analysis into a more robust algorithm.

Section 3.3 then presents an application of the continuation method to the previously established restricted four-body problem. This method is used to solve for required initial conditions corresponding to transfers with a variety of times of flight. Additionally, the continuation method is used to add eccentricity to the orbits of both Earth and Mars. Thus, the circular planetary orbit restrictions held in Chapters 1 and 2 are broken with the gradual addition of eccentricities provided by the continuation method. The final section of the chapter presents the conclusions drawn from the application of continuation methods to the restricted four-body problem.

## 3.2 Continuation Methods

### 3.2.1 Introduction

The continuation method builds upon the capabilities of conventional numerical techniques for solving two-point boundary value problems by decreasing dependency upon a good initial guess. Continuation methods break a highly sensitive two-point boundary value problem into a series of smaller, less sensitive problems. Each of the smaller problems depends upon some continuation parameter  $\tau$  that varies smoothly along a predetermined interval, typically  $[\tau_0, \tau_N] = [0, 1]$ . The family of smaller problems is constructed such that the solution corresponding to  $\tau_0$  is either available or obtainable. The solution corresponding to the parameter  $\tau_N$  is equivalent to the desired solution to the larger boundary value problem. It is important to note that continuation methods decrease the condition number of the problem at hand and generally yield better convergence provided there are no bifurcations in the problem.[5]

Continuation methods are numerical techniques derived from the homotopy analysis method, which is now presented fundamentally. Consider a differential equation

$$\mathbf{A}[u(t)] = \mathbf{0} \quad (3.1)$$

where  $\mathbf{A}$  is a nonlinear operator,  $t$  corresponds to the time, and  $u(t)$  is an unknown variable. Let  $u_0(t)$  be a preliminary approximation to  $u(t)$  and  $\mathbf{L}$  be an auxiliary linear operator with the property

$$\mathbf{L}f = \mathbf{0} \quad (3.2)$$

when  $f = 0$ . The so-called homotopy may then be constructed as follows:

$$\mathbf{H}[\phi(t, \tau), \tau] = (1 - \tau)\mathbf{L}[\phi(t, \tau) - u_0(t)] + \tau\mathbf{A}[\phi(t, \tau)] \quad (3.3)$$

where  $\tau \in [0, 1]$  is the alterable parameter and  $\phi$  is a function of both  $t$  and  $\tau$ . When  $\tau = 0$  and  $\tau = 1$ ,

$$\mathbf{H}[\phi(t, \tau), \tau]|_{\tau=0} = \mathbf{L}[\phi(t, 0) - u_0(t)] \quad (3.4)$$

and

$$\mathbf{H}[\phi(t, \tau), \tau]|_{\tau=1} = \mathbf{A}[\phi(t, 1)] \quad (3.5)$$

respectively. Via Equation (3.2), it is found that

$$\phi(t, 0) = u_0(t) \quad (3.6)$$

is the solution to the equation

$$\mathbf{H}[\phi(t, \tau), \tau]|_{\tau=0} = \mathbf{0} \quad (3.7)$$

Conversely, the solution to

$$\mathbf{H}[\phi(t, \tau), \tau]|_{\tau=1} = \mathbf{0} \quad (3.8)$$

is as follows:

$$\phi(t, 1) = u(t) \quad (3.9)$$

As the variable parameter  $\tau$  increases from 0 to 1, the solution  $\phi(t, \tau)$  of the equation

$$\mathbf{H}[\phi(t, \tau), \tau] = \mathbf{0} \quad (3.10)$$

depends upon the parameter  $\tau$  and changes from the initial approximation  $u_0(t)$  to the solution  $u(t)$  of Equation (3.1). In the field of topology, such continuous variation is termed deformation.[8]

Because this report deals with the integration of restricted four-body orbits as two-point boundary value problems, this chapter presents the application of continuation methods to such boundary value problems. It must be noted that traditional shooting methods have proved to be an unreliable solution to two-point boundary value problems with high sensitivities to initial conditions. One of the main appeals of continuation methods is their functionality when used in combination with shooting methods: such combinations often allow for the solution of problems that could not be solved solely with the use of shooting methods. Combining shooting methods with continuation methods avoids the intricacies involved with using finite-difference methods, while still maintaining the necessary stability.[12]

Continuation methods always deal with the original nonlinear differential equations of the problem, as opposed to linear approximations to these equations. The concern is whether or not the missing initial conditions solved for by a particular method will satisfy the terminal boundary conditions for the original problem over  $[t_0, t_f]$ . With continuation methods, if a solution is found over the desired interval, then this solution represents the answer to the original problem.

With continuation methods, there are two mechanisms that may be used to control the speed of finding a solution. The first mechanism is the weight step value  $\Delta\alpha$  which is used for parameter variation. For instance, if it were desired to increase  $t_f$  from 1.0 to 1.8 seconds and  $\Delta\alpha$  were set to 0.25, then each iteration of the continuation method would involve a 0.2 second increase in  $t_f$ . The smaller the value of  $\Delta\alpha$ , the more likely that the solution to each successive two-point boundary value problem converges. However, a smaller  $\Delta\alpha$  also represents increased computational cost. Thus it is of interest to find a value of  $\Delta\alpha$  which allows for maintained convergence without excessive computational cost. The second mechanism that may be varied is the weight  $\beta$  applied to the perturbation corrections of the initial conditions. A value of  $\beta = 1$  would represent applying full corrections to the initial conditions within each individual boundary value problem.[12]

Perhaps one of the most powerful properties of continuation methods is their versatility, especially within the realm of two-point boundary value problems. When seeking to apply

continuation methods to a different problem, only the subroutines which specify the set of differential equations must be changed significantly. The outline of the continuation method remains the same, allowing for quick application to a wide variety of boundary value problems.

One of the applications of continuation methods is to solve iteratively a sequence of two-point boundary value problems with time spans  $[t_0, t_1]$ ,  $[t_0, t_2]$ ,  $[t_0, t_f]$ , where  $t_0 < t_1 < \dots < t_f$ . For each individual problem, the boundary conditions are held constant, but the integration times increase from the initial  $t_0$  to the desired  $t_f$ . The initial conditions determined as the solution to integration  $i$  are used as the initial guess for integration  $(i + 1)$ , which has an extended integration time. An example of such an application is now given in more detail.

### 3.2.2 Application: Sensitive Two-Point Boundary Value Problem

Roberts and Shipman present a very sensitive two-point boundary value problem that is not solvable by conventional shooting methods.[12] However, such shooting methods may be integrated into a more robust continuation method in order to provide a problem solution. This section provides a comparison between the use of conventional shooting methods and continuation methods for the solution of a sensitive boundary value problem.

The differential equations for the example problem are listed as follows:

$$\dot{x}_1 = x_2 \tag{3.11a}$$

$$\dot{x}_2 = x_3 \tag{3.11b}$$

$$\dot{x}_3 = - \left( \frac{3-n}{2} \right) x_1 x_3 - n x_2^2 + 1 - x_4^2 + s x_2 \tag{3.11c}$$

$$\dot{x}_4 = x_5 \tag{3.11d}$$

$$\dot{x}_5 = - \left( \frac{3-n}{2} \right) x_1 x_5 - (n-1) x_2 x_4 + s(x_4 - 1) \tag{3.11e}$$

The initial conditions are given as

$$x_1(0) = 0, \quad x_2(0) = 0, \quad x_4(0) = 0$$

whereas the terminal conditions are

$$x_2(t_f) = 0, \quad x_4(t_f) = 1$$

Finally, the two scalar parameters are provided as

$$n = -0.1, \quad s = 0.2$$

For the particular problem studied in this section, the limits of integration are  $t_0 = 0.0$  and  $t_f = 7.5$ . The overall objective of using a continuation method to solve the problem is to find the initial conditions  $x_3(0.0)$  and  $x_5(0.0)$  that yield a final state within a specified error  $\xi$  of the two provided terminal conditions. Figure 3.1 provides a flowchart of the algorithm used to approach the two-point boundary value problem. In order to start the algorithm,

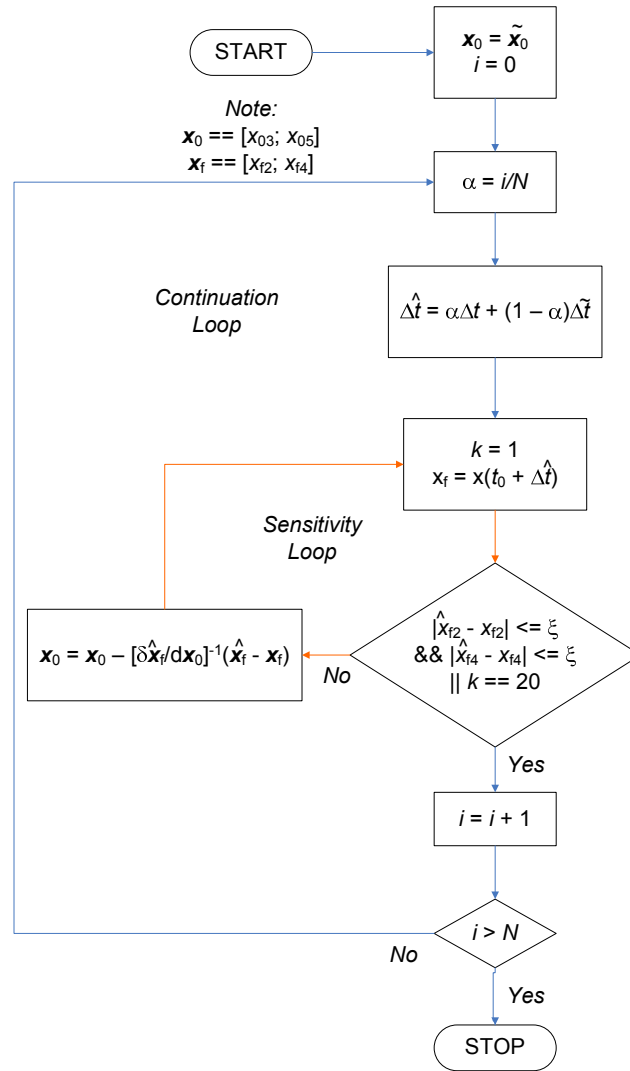


Figure 3.1: **Flowchart for Example Continuation Application.** Flowchart depicting the algorithm used to approach the example two-point boundary value problem provided by Roberts and Shipman. The initial guess values of the missing initial conditions are  $x_3(0) = -1.0$  and  $x_5(0) = 0.6$ .

the missing initial conditions are initialized as  $x_3(0.0) = -1.0$  and  $x_5(0.0) = 0.6$ . These relatively good initial guesses are provided by Roberts and Shipman, and are necessary due to the sensitive nature of the boundary value problem.[12] The remaining initial conditions are all specified in the problem statement. The continuation method algorithm is now broken up into its two main components in order to provide a clear interpretation of its function. The first of these two components to be discussed is the inner sensitivity loop.

### Sensitivity Loop

The sensitivity loop, designated by orange arrows in Figure 3.1, provides a solution to a single setup of the two-point boundary value problem. In other words, this loop can be viewed as a function that takes the specified initial and final conditions as well as the desired

time of integration as inputs. The function then uses a sensitivity matrix to apply iterative corrections to the initial conditions  $x_3(0.0)$  and  $x_5(0.0)$  until the final state vector components  $x_2(t_f)$  and  $x_4(t_f)$  are within the desired error value  $\xi$ . If the final state is not within the specified error after  $k = 20$  iterations, then the sensitivity loop exits with its current initial condition estimates. The state transition matrix  $[\Phi(t, t_0)]$ , a particular style of sensitivity matrix, is used as a mapping between the two variable initial conditions and the two specified final conditions:

$$\begin{pmatrix} x_2(t_f) \\ x_4(t_f) \end{pmatrix} = [\Phi(t_f, t_0)] \begin{pmatrix} x_3(t_0) \\ x_5(t_0) \end{pmatrix} \quad (3.12)$$

where the state transition matrix is populated as:

$$[\Phi(t_f, t_0)] = \begin{bmatrix} \frac{\partial x_2(t_f)}{\partial x_3(t_0)} & \frac{\partial x_2(t_f)}{\partial x_5(t_0)} \\ \frac{\partial x_4(t_f)}{\partial x_3(t_0)} & \frac{\partial x_4(t_f)}{\partial x_5(t_0)} \end{bmatrix} \quad (3.13)$$

Thus a column-wise numerical process may be executed to populate the state transition matrix for each iteration of the sensitivity function. For instance, by perturbing the value of  $x_3(t_0)$  by some small value  $\epsilon$  and re-integrating the boundary value problem, the first column of  $[\Phi(t_f, t_0)]$  is calculated. Subsequently, a second integration using a slight perturbation of  $x_5(t_0)$  provides the second column of the state transition matrix. For example, elements  $\Phi_{11}$  and  $\Phi_{21}$  are computed as:

$$\Phi_{11} = \frac{x_2'^3(t_f) - x_2(t_f)}{\epsilon} \quad (3.14a)$$

$$\Phi_{21} = \frac{x_4'^3(t_f) - x_4(t_f)}{\epsilon} \quad (3.14b)$$

where  $\epsilon$  represents the small perturbation applied to the initial condition  $x_3(t_0)$ . The variables  $x_2'^3(t_f)$  and  $x_4'^3(t_f)$  represent the values of the second and fourth state components after integration of the initial state vector with a slight perturbation in  $x_3(t_0)$ . A total of three separate integrations of the problem are required for each iteration of the sensitivity loop. The first integration tests the final state errors, the second computes the first column of  $[\Phi(t_f, t_0)]$ , and the third computes the second column of  $[\Phi(t_f, t_0)]$ .

After the state transition matrix is populated, its inverse is used to apply corrections to the variable initial conditions as follows:

$$\begin{pmatrix} x_3(t_0) \\ x_5(t_0) \end{pmatrix}' = \begin{pmatrix} x_3(t_0) \\ x_5(t_0) \end{pmatrix} - [\Phi(t_f, t_0)]^{-1} \begin{pmatrix} \delta x_2(t_f) \\ \delta x_4(t_f) \end{pmatrix} \quad (3.15)$$

where  $\delta x_2(t_f)$  and  $\delta x_4(t_f)$  represent the errors in the final values  $x_2(t_f)$  and  $x_4(t_f)$ . The prime on the left side of the equation notes the adjustment being made to the initial conditions. For this problem, LU decomposition is used to compute the inverse of the state transition matrix and to adjust the initial conditions. The adjusted initial conditions  $x_3(t_0)$  and  $x_5(t_0)$  are then used to initiate the following problem iteration until the stopping criterion  $\xi$  has been met.

Once the sensitivity loop converges upon a solution, it then outputs both the initial state vector that yields an acceptable error as well as the integrated state vector. It is important to

note that each completion of the sensitivity loop represents the completion of one two-point boundary value problem. The continuation loop encompasses the inner sensitivity loop in a larger algorithm that demands the solution of multiple two-point boundary value problems.

### Continuation Loop

The continuation loop is modeled after a similar procedure provided by Schaub for solving Lambert's problem given a desired time of flight.[13] As previously stated, the continuation method begins with the initialization of the estimated values for  $x_3(t_0)$  and  $x_5(t_0)$ . Additionally, the loop counter  $i$  is initialized to 0. Before finishing the explanation of the algorithm provided in Figure 3.1, it is important to note several new variables. The continuation parameter  $\alpha$  serves as a weight measure of the problem modeling between the initial and desired problem setups. For instance, the desired final time for this example problem is  $t_f = 7.5$ , but the applied continuation method begins with a value  $\tilde{t}_f = 3.5$ . Therefore, a value  $\alpha = 0.25$  gives 25 percent weight to the desired final time, corresponding to a current final time of  $\hat{t}_f = 4.5$ . Figure 3.1 provides the equation used to calculate the current integration time via  $\alpha$ , repeated here for clarification:

$$\Delta\hat{t} = \alpha\Delta t + (1 - \alpha)\Delta\tilde{t} \quad (3.16)$$

where  $\Delta\hat{t}$ ,  $\Delta\tilde{t}$ , and  $\Delta t$  represent the current, initial, and desired integration times, respectively. Note that when  $\alpha = 0$ , the problem is fully modeled with the initial specified integration time. The integration limit  $\hat{t}_f$  increases gradually until it reaches the desired value  $t_f = 6.4$ , corresponding to  $\alpha = 1$ .

For each new value of integration time  $\Delta\hat{t}$ , the sensitivity function is called to provide the initial conditions  $x_3(0.0)$  and  $x_5(0.0)$  that satisfy the stopping criterion. As shown by Figure 3.1, the stopping criterion for this problem is two-fold:

$$|x_2(\hat{t}_f) - x_2(t_f)| \leq \xi, \quad |x_4(\hat{t}_f) - x_4(t_f)| \leq \xi$$

Thus the stopping criterion deals with the errors in  $x_2(t_f)$  and  $x_4(t_f)$  independently. In this manner, the continuation loop may be viewed as a gradual transformation of one two-point boundary value problem into the final, desired boundary value problem. The loop does not finish until after the continuation parameter  $\alpha$  equals 1, corresponding to a setup that completely models the desired two-point boundary value problem.

### Integration Results

As previously stated, the limits of integration for the desired two-point boundary value problem are  $t_0 = 0.0$  and  $t_f = 7.5$ . The time step used for all integrations in this analysis is  $g = 0.005$ . The perturbation value  $\epsilon$  used to apply slight changes to the initial conditions  $x_3(0.0)$  and  $x_5(0.0)$  is set to  $10^{-6}$ . Additionally, the stopping criterion  $\xi$  used to judge the error in both  $x_2(t_f)$  and  $x_4(t_f)$  is  $10^{-4}$ .

As a means of comparison, the two-point boundary value problem is first integrated without the use of the continuation method. The initial guesses for  $x_3(0.0)$  and  $x_5(0.0)$  (-1.0 and 0.6, respectively) are thus used to integrate directly from  $t = 0.0$  to  $t = 7.5$ . The result

is that the final state vector does not satisfy the convergence criterion of  $\xi = 10^{-4}$  for either  $x_2$  or  $x_4$ . As a matter of fact, the integration blows up for both values of the final state vector. This divergent behavior occurs even when attempting an integration from  $t = 0.0$  to  $t = 4.0$ , which represents a much less demanding problem. Thus the conventional shooting method yields an unacceptable attempt to solve the boundary value problem.

Because the shooting method does not yield convergence within the desired limits of integration, it is extended to a continuation method. The initial value of the final time  $\tilde{t}_f$  is set to 3.5, while the desired value is still  $t_f = 7.5$ . The parameter  $N$  (introduced in Figure 3.1) is set to eight, corresponding to eight gradual steps of 0.5 from  $\tilde{t}_f = 3.5$  to  $t_f = 7.5$ . Figure 3.2 displays the results of the integration scheme implementing the continuation method as a series of blue circles. The red box surrounding the final states

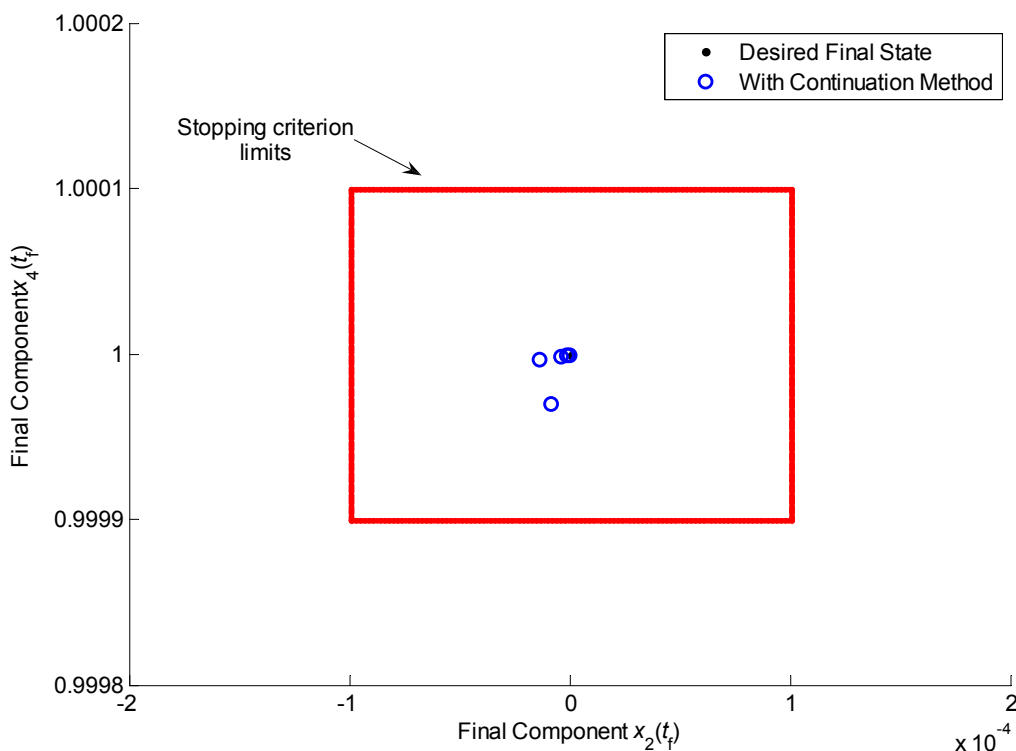


Figure 3.2: **Example Continuation Application Final States.** Plot of the continuation method results relative to the two-dimensional stopping criterion for the example two-point boundary value problem. Note that the values of both  $x_2(t_f)$  and  $x_4(t_f)$  must be within  $10^{-4}$  of the desired final conditions.

corresponds to the imposed stopping criterion value  $\xi = 10^{-4}$  for both  $x_2(t_f)$  and  $x_4(t_f)$ . As Figure 3.2 notes, the continuation method yields a converged solution corresponding to each value of the final integration time  $\hat{t}_f$ . The initial value of the integration time is decreased to  $\Delta\hat{t} = 3.5$  in order to provide a solution given the provided initial conditions. Once this particular solution is provided, it is then used to find a solution to the slightly more difficult problem involving an integration time of  $\Delta\hat{t} = 4.0$ . This process is repeated until a solution is found for the desired two-point boundary value problem, which specifies an integration

time of  $\Delta t = 7.5$ .

Perhaps the most important aspect of the continuation method is its ability to use the initial conditions found from previous problems to provide convergence for a new problem. For the particular example provided by Roberts and Shipman, the problems are distinguished by the limits of integration. However, continuation methods may be used to solve a series of boundary value problems with other differentiating parameters. This application is extended to the restricted four-body problem in following sections. Regardless of the varying problem parameter, it is important that the sensitivity optimization converges for each value of the continuation parameter  $\alpha$ . Table 3.1 provides a listing of the initial conditions  $x_3(0.0)$  and  $x_5(0.0)$  that yield convergence for each iteration of the continuation method. The first

**Table 3.1: Example Continuation Application Initial Conditions.** Listing of the initial conditions  $x_3(0.0)$  and  $x_5(0.0)$  that provide convergence for each iteration of the continuation method. Note that the corrected initial conditions from each iteration are used to initialize the new boundary value problem.

$\hat{t}_f$	$x_3(0.0)$	$x_5(0.0)$	$x_3'(0.0)$	$x_5'(0.0)$
3.5	-1.00000000	0.60000000	-0.97819773	0.64678672
4.0	-0.97819773	0.64678672	-0.96916706	0.65253832
4.5	-0.96916706	0.65253832	-0.96667565	0.65311112
5.0	-0.96667565	0.65311112	-0.96629732	0.65299880
5.5	-0.96629732	0.65299880	-0.96628917	0.65293178
6.0	-0.96628917	0.65293178	-0.96630414	0.65291346
6.5	-0.96630414	0.65291346	-0.96630999	0.65290994
7.0	-0.96630999	0.65290994	-0.96631149	0.65290951
7.5	-0.96631149	0.65290951	-0.96631178	0.65290953

column of Table 3.1 displays the final time  $\hat{t}_f$  corresponding to each of the nine iterations of the continuation method. The second and third columns provide the initial guesses for  $x_3(0.0)$  and  $x_5(0.0)$  used to begin the sensitivity optimization for that iteration. The fourth and fifth columns show the corrected initial condition values  $x_3'(0.0)$  and  $x_5'(0.0)$  found after each use of the sensitivity optimization. The arrows in the table show how each set of corrected initial conditions is used to initialize a new iteration of the continuation method corresponding to a larger  $\hat{t}_f$ . As noted in Table 3.1, the values of the initial conditions necessary to solve the desired two-point boundary value problem are  $x_3(0.0) = -0.96631178$  and  $x_5(0.0) = 0.65290953$ . The table shows how the sensitivity of the boundary value

problem to the initial conditions increases with increasing integration time  $\Delta\hat{t}$ . By the last iteration of the continuation method, the corrected initial conditions change at most by two significant digits. An interesting study could be performed to relate the sensitivity of the two-point boundary value problem to the integration time  $\Delta\hat{t}$ . Such an analysis is not provided in this report.

## Conclusions

The example problem provided by Roberts and Shipman gives insight into the advantages of using continuation methods to solve sensitive two-point boundary value problems. Traditional shooting methods have a greater risk of failing to converge upon a solution for problems with a high sensitivity to the initial guess  $\mathbf{x}(t_0)$ . This greater risk is partly due to the fact that traditional shooting methods can only provide a solution to a single boundary value problem. If the particular problem being studied is prone to divergence, then the shooting method requires an excellent initial guess in order to find a solution. However, continuation methods allow for the use of solutions to similar problems in order to converge upon the solution of the desired boundary value problem. If the solution to a nearby problem setup is known, then that solution may be used with a continuation method to find a solution to the desired two-point boundary value problem. The conclusions drawn from this example continuation method application are as follows:

1. Continuation methods allow for the use of solutions to similar two-point boundary value problems in order to solve a sensitive desired problem.
2. Traditional shooting methods do not allow for such gradual transformation from one problem setup to another.
3. The convergence of the sensitivity optimization depends upon many factors, several of which include the integration time step  $g$ , perturbation value  $\epsilon$ , convergence criterion  $\xi$ , and initial guess  $\mathbf{x}(t_0)$ .
4. For the example problem provided by Roberts and Shipman, the initial conditions determined to provide convergence over the interval  $[0.0, 7.5]$  are  $x_3(0.0) = -0.96631178$  and  $x_5(0.0) = 0.65290953$ .
5. A future study could develop a relationship between the sensitivity of the example boundary value problem and the integration time  $\Delta\hat{t}$ .

## 3.3 Restricted Four-Body Problem

Section 3.2 provides an introduction to the concept of continuation methods, as well as their use to solve an example problem provided by Roberts and Shipman.[12] The following section presents the application of continuation methods to the restricted four-body problem, which is introduced in Chapter 1. As in previous chapters, the gravitational effects of the sun, Earth, and Mars on the spacecraft are taken into account throughout the entire transfer orbit; the influences of Earth and Mars on the sun are neglected. All celestial motion is planar,

but the circular restrictions on the planets' heliocentric orbits are relaxed via use of the continuation method. This section illustrates how effective the combination of continuation methods and sensitivity analyses can be when used to assess families of possible transfer orbit geometries.

### 3.3.1 Altering the Time of Flight: First Method

The first application of the continuation method to the restricted four-body problem is used to decrease the time of flight of the original transfer orbit. All of the transfers dealt with thus far throughout this paper have been approximately Hohmann, with a time of flight of roughly 259 days. Using an algorithm very similar to that presented in Figure 3.1, it is possible to find solutions for transfer orbits that have smaller transfer times. In this case, the continuation parameter  $\alpha$  is used to iteratively decrease the value of the time of flight  $\Delta t$ . Figure 3.3 illustrates the solutions to several of the iterations of the continuation method. As the figure shows, the continuation method is used to decrease the overall transfer time

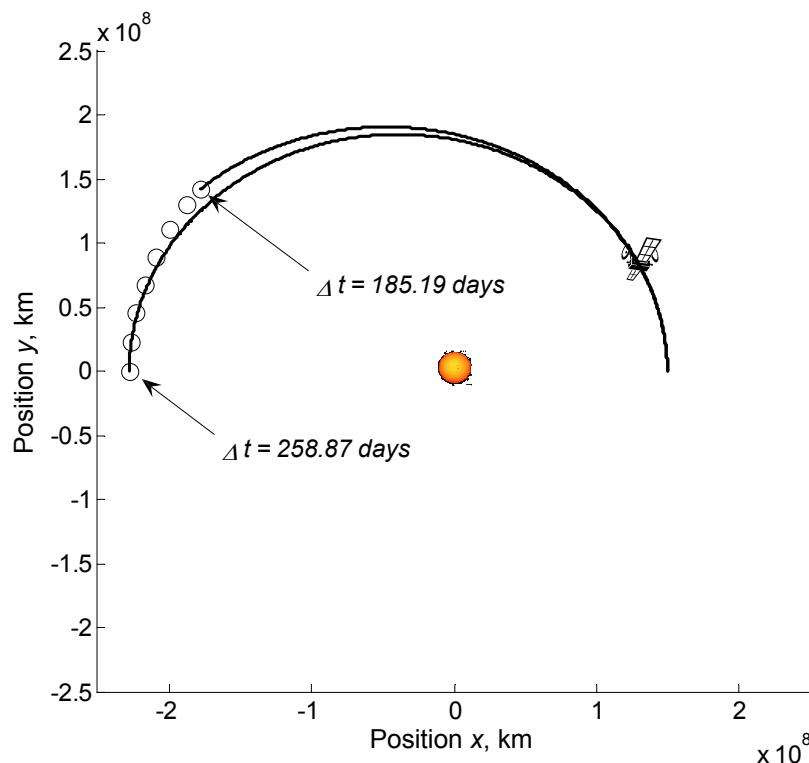


Figure 3.3: **Progressively Smaller Values of  $\Delta t$ .** Illustration of the final heliocentric positions achieved after several of the iterations of the continuation method. In this case, the method is used to decrease the transfer time of flight  $\Delta t$ .

from 258.87 days to 185.19 days. This difference in transfer times represents a significant variation in  $\Delta v$  costs, as each different transfer geometry requires a unique initial Earth-relative state vector. Each of the circles in Figure 3.3 represents the final spacecraft position for a particular iteration of the continuation method. As previously described in Section 3.2, the initial condition results from one iteration of the continuation method are used as

a starting point for the next iteration. In this manner, solutions are obtained for an entire family of transfer orbits, each with a unique transfer time.

It is important to note that it is not necessary to stop the continuation analysis at a transfer time of 185 days. The time of flight could continue to be decreased through a larger family of transfer orbits, depending upon mission needs and constraints. The computation time required for this particular application of the continuation method is on the order of seconds considering present-day computational capabilities. However, this speed is partly due to the fact that the stopping criterion for the sensitivity correction scheme only requires achieving a particular position  $(x_f, y_f)$  relative to Mars upon completion of the transfer. The criterion sets no limits on the spacecraft's Mars-relative velocity at the end of the orbit, meaning that a ballistic trajectory is deemed 'acceptable.' In industrial applications, such an arrival trajectory would not be acceptable, and thus the following subsection presents a second application of the continuation method to the four-body problem.

### 3.3.2 Altering the Time of Flight: Revised Method

The revised application of the continuation method uses a different sensitivity correction scheme in order to solve each separate two-point boundary value problem. Instead of optimizing the final Mars-relative position, the revised method requires that the spacecraft achieve a final Mars-relative altitude of 600 km with no radial velocity component. In this manner, if it were desired, another burn could be applied at the final spacecraft position in order to prepare for a parking orbit about Mars. Figure 3.4 displays the heliocentric transfer orbit with a decreased transfer time  $\Delta t$  using the revised continuation application. The time

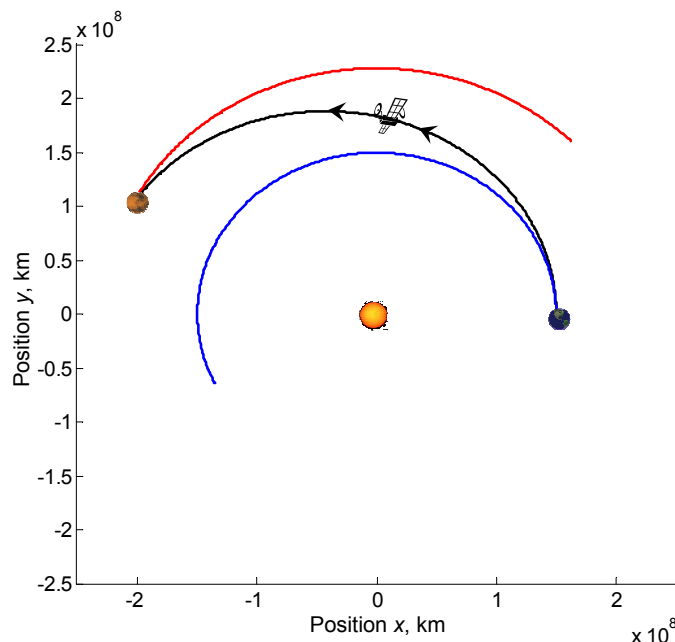


Figure 3.4: **Final Heliocentric Transfer Geometry: Revised Method.** Depiction of the final heliocentric transfer geometry achieved by using the revised continuation method. The transfer time for the orbit shown is 208 days.

of flight for the transfer shown in Figure 3.4 is 208 days, which is slightly greater than that

of the shortest transfer presented in the previous section. However, despite the smaller range of  $\Delta t$  values, the revised continuation method application still takes significantly longer to converge upon each new problem solution as it approaches the 208-day transfer. More specifically, the computational time spent altering the time of flight from 259 days to 208 days using the revised method is approximately 12.56 minutes. As stated previously, the first application of the continuation method converges within a matter of seconds.

The disparity in computational time spent using the the two continuation applications is partially due to the difference in sensitivity stopping criteria. Achieving a specified final Mars-relative altitude with zero radial velocity component is more demanding than simply attaining a final position relative to Mars.

Table 3.2 provides a listing of the initial velocity components for 11 iterations of the revised continuation application. Note that not all iterations of the continuation method

**Table 3.2: Initial Velocity Corrections: Revised Method.** Listing of the corrections made to the initial velocity components  $v_x(t_0)$  and  $v_y(t_0)$  for 11 iterations of the revised continuation application.

$t_i$ , days	$v_x(t_0)$ , km/s	$v_y(t_0)$ , km/s	$v_x'(t_0)$ , km/s	$v_y'(t_0)$ , km/s
258.87	9.19141690	35.29793200	9.19114570	35.29843755
253.81	9.23609534	35.22294409	9.23826018	35.21931686
248.76	9.27549909	35.15733884	9.27725767	35.15444262
243.71	9.30677244	35.10669586	9.30812314	35.10456785
238.65	9.32958380	35.07226596	9.33079440	35.07044082
233.60	9.34437156	35.05377067	9.34488997	35.05329165
228.55	9.35094693	35.05196783	9.35103602	35.05236634
223.49	9.34854802	35.06853312	9.34819404	35.06984405
218.44	9.33713856	35.10364739	9.33632438	35.10590371
213.39	9.31634581	35.15794262	9.31505101	35.16117453
208.33	9.28572775	35.23199635	9.28392841	35.23623110

are shown in Table 3.2. Overall, 100 iterations are used to alter the transfer time of flight from 259 days to 208 days. Attempting to use 80 iterations instead of 100 results in failed convergence of the continuation method. An interesting analysis could assess the problem characteristics that influence the threshold value for the number of iterations  $N$ . More sensitive boundary value problems require a higher value of  $N$  in order to make neighboring boundary value problems more similar. As stated previously in Section 3.2, the continuation method converges as long as the solution to one boundary value problem lies within the sphere of convergence for the neighboring problem.

Figure 3.5 provides an illustration of the final Mars-relative arrival orbit. Another reason

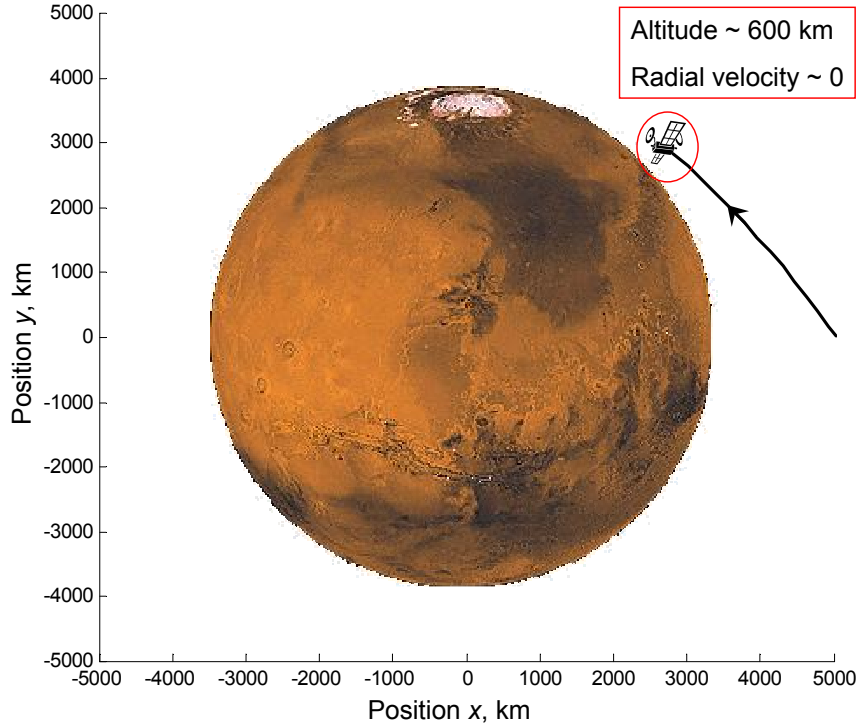


Figure 3.5: **Final Mars-Relative Transfer Geometry: Revised Method.** Depiction of the final Mars-relative transfer geometry achieved by using the revised continuation method. The transfer time for the orbit shown is 208 days.

that the revised continuation application takes so much longer to converge upon iterative solutions is because the required final altitude is only 600 km, as opposed to the previous 4000 km. Such a small final altitude requires more iterations of the sensitivity correction scheme for each individual transfer orbit. As the figure shows, the spacecraft approaches its final position with roughly no radial velocity component. Another way to perform the same arrival orbit optimization would be to require a specified periapsis radius  $r_3$  and time to periapsis  $t_3$ . Chapter 2 presents sensitivity applications that deal directly with the final periapsis radius  $r_3$ .

With the use of the continuation method, a series of arrival orbits all similar to that shown in Figure 3.5 are achieved for a family of transfers. As such, all of the transfer orbits satisfy the two-dimensional sensitivity stopping criterion. Depending upon the needs and constraints for a proposed mission to Mars, a performance function could be created to assess trade offs between increasing  $\Delta v$  and decreasing  $\Delta t$  for the family of orbits. The continuation method provides an excellent method for modeling the various orbits in preparation for design synthesis and selection.

### 3.3.3 Altering Mars' Eccentricity

In addition to changing the transfer time of flight, continuation methods may also be used to alter the shape of the planetary orbits. The only change made to the algorithm presented in Figure 3.1 is that the continuation parameter  $\alpha$  is now used to gradually change a particular orbit parameter, such as eccentricity, instead of time. In this manner, the orbits of both Earth and Mars may be transformed from circular to a close approximation of their true geometries. The continuation method has the capability of altering any of the orbit elements used to describe the planetary orbits, thereby making any trajectory possible. Once again, the only condition is that one solution is already found for a particular transfer from Earth to Mars.

In order to show how the continuation method may be used to alter the planetary orbits, the algorithm in Figure 3.1 is remodeled slightly to increase Mars' eccentricity. According to the Jet Propulsion Laboratory, a good approximation for Mars' eccentricity is 0.09341233.[7] Thus, with the use of the continuation method, Mars' eccentricity is gradually increased from 0.0 to a final value of 0.09341233. Figure 3.6 displays the resulting heliocentric transfer orbit of the spacecraft, after the addition of Mars' eccentricity. The transfer orbit shown in

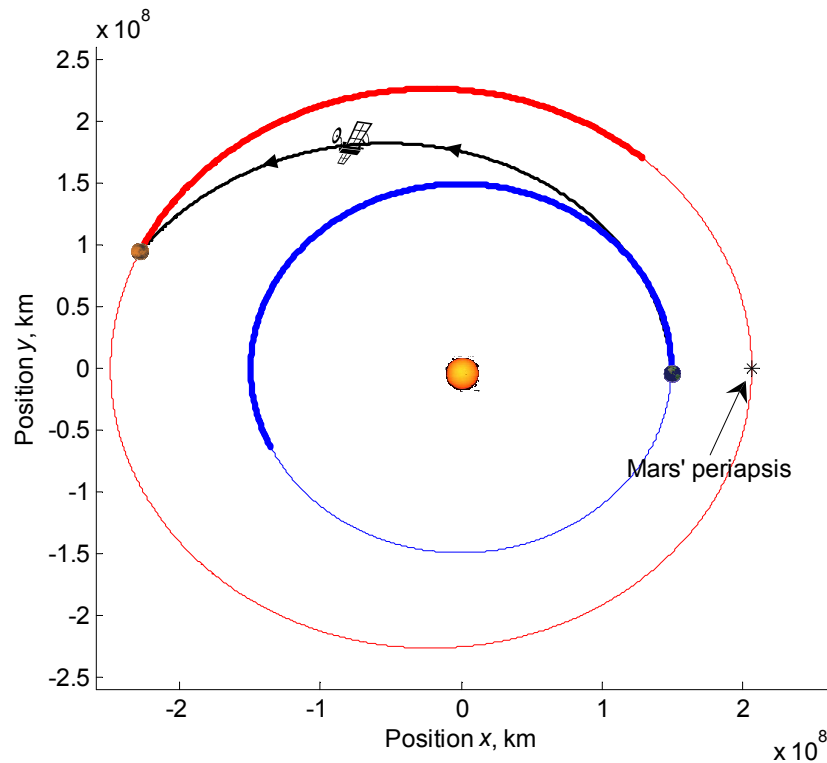


Figure 3.6: **Heliocentric Motion: Elliptic Martian Orbit.** Illustration of the transfer orbit from Earth to Mars, including Mars' eccentricity of 0.09341233. Note that the transfer time is 208 days.

Figure 3.6 has several generalized features when compared with the transfers developed in previous chapters. The transfer time during the continuation optimization is kept constant at 208 days; thus, the transfer is no longer minimum-energy. Additionally, Mars has an elliptic trajectory, with its periapsis arbitrarily chosen to be located along the  $x$ -axis of the sun-centered inertial frame. Because the periapsis points for both Earth and Mars shift gradually about the sun, the specific periapsis locations are not of great concern in this optimization.

The bold portions of the planetary orbits shown in Figure 3.6 correspond to the propagated positions of each planet from  $t_0 = 0$  to  $t_f = 208$  days. Mars' initial mean anomaly angle is set to the offset angle from previous orbit modeling done in Chapters 1 and 2. In this manner, the spacecraft still performs its Martian rendezvous at a position relatively close to previous orbit geometries. Perhaps the most important feature of Figure 3.6 is its illustration of how continuation methods may be used to alter any interplanetary transfer orbit geometry in a generalized fashion. Simple problems, such as a Hohmann transfer between circular orbits, are easily transformed into good approximations of true interplanetary motion. The combination of continuation methods and sensitivity correction schemes represents a very powerful tool for modeling non-Keplerian motion.

## 3.4 Conclusions

Chapter 3 presents an investigation into the use of continuation methods to model interplanetary transfer orbits. Section 3.2 provides an introduction to the concept of continuation methods, including how such methods incorporate sensitivity analyses into the solution of multiple boundary value problems. The continuation method is then used to solve a sample problem presented by Roberts and Shipman.[12] Section 3.3 extends the concepts developed in Section 3.2 to modeling the restricted four-body transfer orbit from Earth to Mars. Specifically, the continuation method is used to alter both the spacecraft's time of flight and Mars' eccentricity. Several conclusions are drawn from the analysis performed in Chapter 3:

1. Traditional shooting methods do not allow for the gradual transformation of one boundary value problem into another.
2. Continuation methods use information from previous boundary value problem solutions to solve neighboring problems, and thus find entire families of solutions.
3. Continuation methods may be used to alter both time of flight and planetary orbit parameters for a particular transfer orbit geometry.
4. In general, the combination of continuation methods and sensitivity analyses is an effective tool for modeling interplanetary transfer orbits.
5. Future work could investigate how to predict whether or not a particular iteration of the continuation method will converge or diverge, given the fidelity of the initial guess developed from previous iterations.

# Bibliography

- [1] Roger R. Bate, Donald D. Mueller, and Jerry E. White. *Fundamentals of Astrodynamics*. Dover Publications, Inc. New York, NY., 1971.
- [2] Richard H. Battin. *An Introduction to the Mathematics and Methods of Astrodynamics, Revised Edition*. American Institute of Aeronautics and Astronautics, Inc. Reston, VA., 1999.
- [3] Steven C. Chapra. *Applied Numerical Methods with MatLab*. McGraw-Hill Companies, Inc. New York, NY., 2005.
- [4] William L. Hallauer Jr. *Introduction to Linear, Time-Invariant, Dynamic Systems*. William L. Hallauer, Jr., Blacksburg, VA, 2005.
- [5] Mischa Kim. *Continuous Low-Thrust Trajectory Optimization: Techniques and Applications*. Ph. D. Dissertation, Aerospace and Ocean Engineering Department, Virginia Polytechnic Institute, Blacksburg, VA, 2005.
- [6] Werner Kohler and Lee Johnson. *Elementary Differential Equations with Boundary Value Problems*. Pearson Education, Inc., New York, NY, 2004.
- [7] Jet Propulsion Laboratory. Solar system dynamics: Horizons ephemerides. <http://ssd.jpl.nasa.gov/>, 04 May 2007.
- [8] Shijun Liao. *Beyond Perturbation: Introduction to the Homotopy Analysis Method*. CRC Press LCC, Boca Raton, FL, 2004.
- [9] Tao Lin. *Class Notes: Introduction to Numerical Analysis*. Virginia Polytechnic Institute and State University, Blacksburg, VA, 2006.
- [10] Thomas R. Reppert. Extending the patched-conic approximation to the restricted four-body problem. *AIAA Student Journal*, 44(2):1–11, May–Aug. 2006.
- [11] Thomas R. Reppert. Extending the patched-conic approximation to the restricted four-body problem. Technical report, Virginia Polytechnic Institute and State University, Blacksburg, VA 24060, May 2006.
- [12] S. M. Roberts and J. S. Shipman. *Two-Point Boundary Value Problems: Shooting Methods*. American Elsevier Publishing Company, Inc., New York, NY, 1972.

- [13] Hanspeter Schaub and John L. Junkins. *Analytical Mechanics of Space Systems*. American Institute of Aeronautics and Astronautics, Inc., Reston, VA, 2003.
- [14] James Stewart. *Calculus: Early Transcendentals*. Thomson Learning, Inc., Belmont, CA, 2003.